Title
First-Principles Modeling of Thin-Film Ferroelectrics

Author
Angsten, Thomas Henry

Publication Date
2018

Peer reviewed|Thesis/dissertation

First-Principles Modeling of Thin-Film Ferroelectrics

by

Thomas Henry Angsten

A dissertation submitted in partial satisfaction of the

requirements for the degree of

Doctor of Philosophy

in

Engineering - Materials Science and Engineering

in the

Graduate Division

of the

University of California, Berkeley

Committee in charge:

Professor Mark Asta, Chair
Professor Jeffrey Neaton
Professor Lane Martin

Spring 2018

First-Principles Modeling of Thin-Film Ferroelectrics

Abstract

First-Principles Modeling of Thin-Film Ferroelectrics

by

Thomas Henry Angsten

Doctor of Philosophy in Engineering - Materials Science and Engineering

University of California, Berkeley

Professor Mark Asta, Chair

The goal of this dissertation is to explore the properties of thin-film ferroelectrics using first-principles computational methods. Achieving this goal requires both the development of efficient methods for computing thin-film properties as well as the application of these methods to a variety of thin-film materials of interest. The research included in this dissertation is thus composed of a mix of these two efforts.

First, the structural properties, energetics, and polarizations of perovskite-based thin-film oxide systems are computed as a function of biaxial strain state and epitaxial orientation, employing an automated computational workflow based on density functional theory (DFT). A total of 14 compositions are considered, of the form ABO_3, with A=Ba, K, Na, Pb, and Sr and non-magnetic B=Hf, Sn, Ti, Zr, Nb, Ta, and V site cations chosen to yield tolerance factors with values ranging between 0.95 and 1.1. Three biaxial strain states corresponding to epitaxial growth of (100)-, (110)-, and (111)-oriented films are considered, with misfit strains ranging between -4% to 4%. Results are presented for the series of perovskite-derived phases, and their corresponding symmetries, which are energetically favorable as a function of misfit strain, along with their corresponding equilibrium atomic positions, lattice parameters, and electric polarizations. The results demonstrate robust trends of in-plane polarization enhancement under tensile strain for all epitaxial orientations, and out-of-plane polarization enhancement with compression for the (100)- and (110)-oriented films. Strains corresponding to the (111)-growth orientation lead to a wider variety of out-of-plane polarization behavior, with $BaTiO_3$ showing anomalous diminishing polarization with compression. Epitaxial orientation is shown to have a strong effect on the nature of strain-induced phase transitions, with (100)-oriented systems tending to have smooth, second-order transitions and (110)- and (111)-oriented systems more commonly exhibiting first-order transitions. The significance of this effect for device applications is discussed, and a number of systems are identified as potentially interesting for ferroelectric thin-film applications based on energetic stability and polarization behavior. Analysis of polarization behavior across different orientations reveals distinct groups into which compositions can be

organized, some of which having polarization dependencies on misfit strain that have not been predicted previously.

Following the work described above, ground-state epitaxial phase diagrams are calculated by DFT for $SrTiO_3$, $CaTiO_3$, and $SrHfO_3$ perovskite-based compounds, accounting for effects of antiferrodistortive and *A*-site displacement modes. Biaxial strain states corresponding to epitaxial growth of (001)-oriented films are considered, with misfit strains ranging between -4% and 4%. Ground-state structures are determined using a computational procedure in which input structures for DFT optimizations are identified as local minima in expansions of the total energy with respect to strain and soft-mode degrees of freedom. Comparison to results of previous DFT studies demonstrates the effectiveness of the computational approach in predicting ground-state phases. The calculated results show that antiferrodistortive octahedral rotations and associated *A*-site displacement modes act to suppress polarization and reduce epitaxial strain energy. A projection of calculated atomic displacements in the ground-state epitaxial structures onto soft-mode eigenvectors shows that three ferroelectric and six antiferrodistortive displacement modes are dominant at all misfit strains considered, with the relative contributions from each varying systematically with strain. Additional *A*-site displacement modes contribute to the atomic displacements in $CaTiO_3$ and $SrHfO_3$, which serve to optimize the coordination of the undersized *A*-site cation.

Further, an effort is made to identify alternative vanadate perovskite-derivative systems similar to the well-studied pressure-stabilized PVO structure. To achieve this, the stability of perovskite-derivative thin-film structures of KVO_3 and $NaVO_3$ are studied under compressive biaxial strain. The electronic structure and polar properties of these compounds are computed as a function of biaxial strain, and the results are compared to those obtained for experimentally-observed $PbVO_3$ structures. It is demonstrated that the substitution of Pb with monovalent K or Na cations increases the strength of the vanadyl bond due to the removal of the spatially extended Pb 6*p* states. Both KVO_3 and $NaVO_3$ exhibit epitaxially stabilized perovskite-derivative phases having large polarizations and low misfit strain energies. The calculated epitaxial phase diagram for KVO_3 predicts a strain-induced phase separation from -4% to 1.5% misfit strain into a ferroelectric *Cm* phase, having square-pyramidal coordination of the *B*-site, and a paraelectric *Pbcm* phase, having tetrahedral coordination of the *B*-site. The results show that strain-stabilized polar vanadate compounds may occur for other compositions in addition to PVO, and that changes in the *A*-site species can be used to tune bonding, structure, and functional properties in these systems.

Contents

Acknowledgments

To my research advisor, Professor Mark Asta, for inspiring me to achieve my fullest potential and for providing patient guidance throughout my PhD.

To my family, for encouraging intellectual curiosity from an early age.

To my wife, Ami, for her unyielding love and support of everything I do.

This work was supported by the U.S. Department of Energy, Office of Science, Office of Basic Energy Sciences, Materials Sciences and Engineering Division, Contract No. DE-AC02-05-CH11231: Materials Project program KC23MP. T.A. acknowledges support from a National Science Foundation Graduate Research Fellowship (grant No. DGE1106400). This research used resources of the National Energy Research Scientific Computing Center, which is supported by the Office of Science of the U.S. Department of Energy under Contract No. DE-AC02-05-CH11231.

CHAPTER 1

Introduction

For many decades, ferroelectric materials have provided functionalities crucial to a wide variety of technological applications. The discovery of barium titanate in the 1940s kick-started the rapid proliferation of novel electronic devices based on the ferroelectric effect, and many of these devices are still used in modern-day technologies [1]. Demand in the electronics industry for smaller components have motivated the recent focus on integrating the functionality of the ferroelectric effect into microelectronic devices. To achieve this, ferroelectric materials can be grown as epitaxial thin films having constrained dimensions ammenable to device miniaturization. More than just a change in shape accompanies this tranformation, as ferroelectrics in thin film form genrally have properties that can differ significantly from those in the bulk. In particular, the strain conditions imposed on the film during growth have a large impact on properties, and subsequent control of these conditions comprises the field of epitaxial strain engineering. Understanding how epitaxial boundary conditions influence the properties of ferroelectric thin films is therefore fundamental to discovering and designing improved materials for microelectronic applications.

1.1 Epitaxial Growth of Thin Films

Growth of thin films can be accomplished using a variety of deposition processes, but the most relevant to strain-engineered ferroelectrics are those leading to epitaxial growth. Epitaxy is the process of film growth in which the presence of a substrate significantly influences the crystallographic structure of the deposited film. Homoepitaxy is the process of depositing a material onto a substrate of the same composition, while heteroepitaxy is the growth of one material onto another of distinct composition. Heteroepitaxy is useful in the context of strain engineering ferroelectric thin films, as it can lead to biaxial strains in the film. In heteroepitaxy, the extent to which the substrate controls structural ordering in the material growing on top of it, termed the epilayer, is controlled by the degree of matching between the crystal structures of the substrate and film along the interface [2].

1.1.1 Accommodation of the Epilayer

Figure 1.1 shows a schematic of the different interactions a deposited film (black circles) can have with the underlying substrate (white circles) under heteroepitaxy. In the simplest case illustrated in Fig. 1.1a, the deposited material and substrate have crystal structures with the same periodicities. Matching at the interface is exact, and no strain in the epilayer results. This is termed coherent growth. More often, the crystal structure of the epilayer has different spacings compared to the substrate. In this case, three different cases of growth can occur. In Fig. 1.1b, the structures of the substrate and film have different symmetries and lattice spacings and the interfaces formed are not well matched. This situation is referred to as incoherent growth and is common when the atoms in the film and substrate phases interact weakly, *e.g.*, through van der Waals forces [3]. Figure 1.1c shows an example of when the film material's natural lattice parameter in the bulk is larger than that of the substrate, but matching at the interface still persists. As a result, the epilayer is strained in order to match with the substrate below. This is the growth case most useful to strain engineering of ferroelectric films, as it results in a film with homogeneous biaxial strain. Finally, Fig. 1.1d shows the case in which the elastic energy that would result from the formation of a strained epitaxially matched film leads to the formation of misfit dislocations to accommodate the difference between the film and substrate lattice constants. In this case, the epilayer is still strained, but with some of the stress relieved by the formation of dislocations. The cases shown in Figs. 1.1c and d are discussed in more detail below.

Parts a, c, and d of Fig. 1.1 show a film which exhibits some degree of matching between the deposited material and the underlying substrate. Under the appropriate conditions, film growth often displays this behavior. The basic driving force for films to match with a substrate is the minimization of potential energy at the atomic sites. Ordered crystalline structures commonly appear in nature because their highly symmetric sites tend to provide low-energy bonding environments for atoms, and flaws in crystals interrupt symmetry and thus tend to increase the potential energy of atomic sites. In this manner, crystal surfaces and interfaces give way to excess energies per unit area. A film material that is being deposited on a crystalline substrate will attempt to merge symmetries of the two crystals by maximizing the density of bonds across the interface, thereby retaining the preferred bonding environment for each atomic site. The successful epitaxial growth of a film is dependent on a number of factors, including the ability of the film crystal structure to match with the substrate, density of defects and imperfections at the substrate interface, chemical compatibility between the film and substrate materials, and sufficiently high temperature to allow for depositing atoms to rearrange before being buried by the next layer [4].

When a deposited material has a high degree of matching with the underlying substrate, and few defects disrupt the periodicity of this matching, the result is a coherently strained epitaxial thin film. In addition, if epitaxial growth is precisely controlled, the resulting interface can be atomically abrupt [2]. If the atomic periodicity of the substrate and coherently

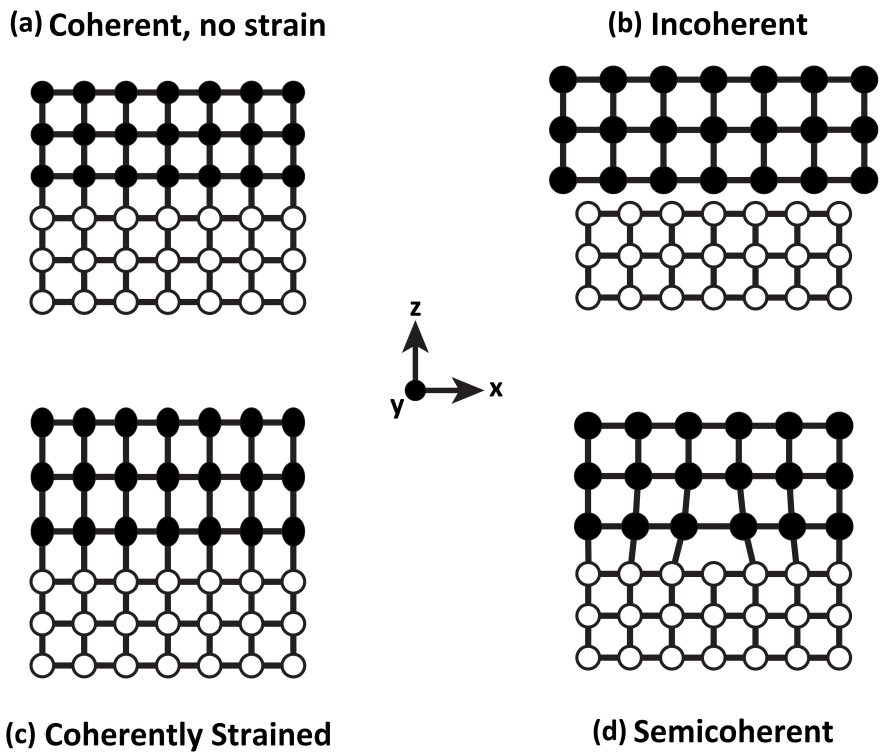

Figure 1.1: Ways in which the epilayer lattice (solid circles) can be accommodated by the substrate lattice (white circles).

strained film materials are not quite aligned, a biaxial strain in the deposited film results. The fractional mismatch between two crystal structures is defined as:

$$\bar{\eta} = \frac{a_e - a_s}{a_e}, \tag{1.1}$$

where a_e and a_s are relevant atomic spacings along the interfacial film and substrate surface directions, respectively. If the thermal-expansion coefficients of the film and substrate materials are different, $\bar{\eta}$ is also a function of temperature. A general rule [3] for epitaxy is that $|\bar{\eta}| < 0.1$ to obtain a coherently strained thin film. If the mismatch is any greater than this threshold, not enough bonds at the interface are aligned to make coherent matching energetically favorable. The exact threshold is dependent on film and substrate composition, as well as film thickness, as discussed below. Figure 1.2 shows an example coherently strained perovskite film on a perovskite substrate with a slightly larger in-plane lattice constant. The epilayer is subsequently subjected to tensile biaxial strain in the interface plane, with an associated Poisson contraction in the [001] direction. The interface is shown to be atomicly abrupt with no defects.

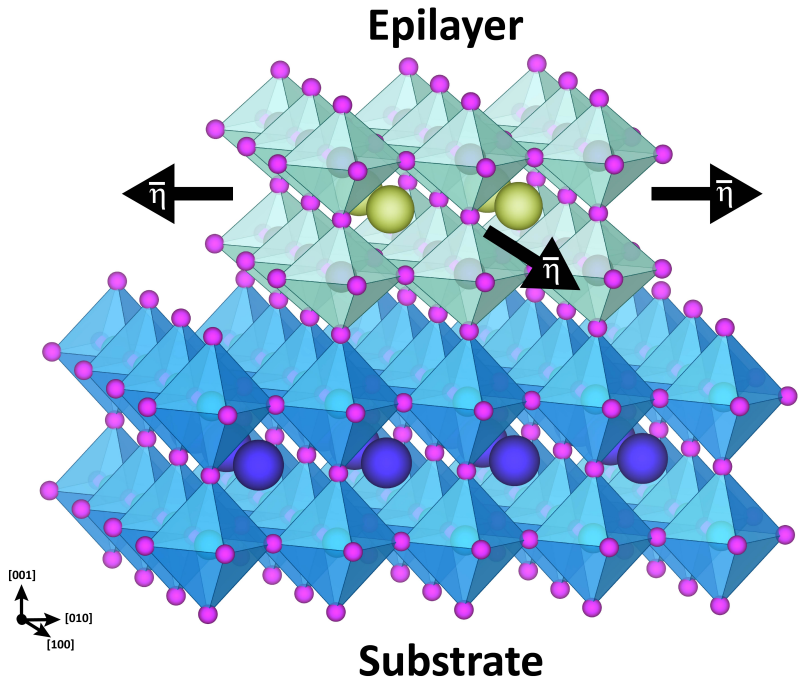

Figure 1.2: Schematic of a coherently strained epitaxial thin film for perovskite heteroepitaxy. The largest spheres indicate the perovskite A-cation, commonly a mono- or divalent metal, the small pink spheres indicate the anion, commonly oxygen, and the center of the anion octahedra are occupied by the B-cation, commonly a tetra- or pentavalent transition metal. Redrawn, based on Fig. 1 of Ref. [2].

Under commensurate growth, unique mechanical boundary conditions persist within the epilayer. An assumption that is commonly made is that, due to the much greater thickness of the substrate as compared to the epilayer, the substrate is considered to be completely rigid. The resulting biaxial strain from epitaxy is thus isolated in the epilayer, and, in the case of a substrate with four-fold symmetry, it is simply equal to the opposite of the degree of mismatch:

$$\epsilon_{xx} = \epsilon_{yy} = -\bar{\eta}. \tag{1.2}$$

The imposition of a strain in the epilayer has an associated biaxial stress and corresponding tetragonal strain. For an elastically isotropic material, the stress and strain are given by:

$$\sigma_{xx} = \sigma_{yy} = \frac{Y}{1-\nu}\epsilon_{xx}, \tag{1.3}$$

and

$$\epsilon_T = \epsilon_{zz} - \epsilon_{xx} = -\frac{1+\nu}{1-\nu}\epsilon_{xx}, \tag{1.4}$$

where Y and ν are the Young's modulus and Poisson's ratio of the film, respectively. Equation 1.4 shows that, under biaxial compression (substrate lattice periodicity is smaller than film's), a typical film expands out-of-plane, while under biaxial tension (substrate lattice periodicity is larger than film's), the film contracts in the out-of-plane direction.

1.1.2 Strain Relaxation through Dislocation Formation

In discussing Fig. 1.1d above, it was mentioned that, in cases where mismatch is larger than a critical threshold, defects form in order to relieve the elastic energy. These defects are often undesirable in the context of strain engineering ferroelectric thin films, as they lead to inhomogenous strain in the film and often degraded properties. Dislocations in biaxially strained thin films release energy due to reduction in the biaxial strain, but their formation also increases the interfacial energy. By quantifying these two competing energetic terms, the conditions under which strain relaxation occurs through dislocation formation can be specified. The treatment given here follows that found in Ref. [3]. The scope of this treatment is limited to giving a broad overview of the underlying physics of dislocation formation in thin films, and thus a number of simplifying assumptions are made. In particular, isotropic and homogenous elasticity of the film and substrate is assumed throughout.

The strain energy as a function of parameters of the film and degree of mismatch is given by:

$$U_\epsilon(J/m^2) = \frac{Y}{1-\nu}\epsilon_{xx}^2 h, \tag{1.5}$$

where h is the film thickness. This expression is obtained by integrating the force applied as the film is compressed from the relaxed state to the contrained commensurate epilayer state. When compression or tension is applied, shear stresses along certain crystallographic planes in the film develop. If these stresses become great enough, planes will begin to slip, in a way similar to when bulk materials reach a critical applied shear stress. The slipping is facilitated by the breaking and reforming of bonds, and the result is the formation of misfit dislocations. A grid of such dislocations will form in the interface of the substrate-epilayer bicrystal, with the density of the grid depending on various conditions and materials properties.

The energy of a dislocation can be partly attributed to its core, and partly to the strain field generated around this core. For a mixed dilocation with Burgers vector $\mathbf{b}$ and shear modulus of elasticity G_s, the strain energy per unit length is:

$$U_d'(J/m) \approx \frac{G_s b^2}{4\pi(1-\nu)} ln\left(\frac{4h}{b}\right). \tag{1.6}$$

Here, b is the magnitude of the Burgers vector, and the factor of 4π in Eq. 1.6 comes from the radial symmetry of the strain field. This expression is derived from a continuum model, wherein the outer radius of the strain field is assumed to be equal to the film thickness, h, and the inner radius, which accounts for the energy of the dislocation core, is arbitrarily set to $\frac{1}{4}b$. The generation of dislocations affects the degree of biaxial strain in the epilayer:

$$\epsilon_{x,y} = \pm \rho_l b sin(\beta) cos(\gamma) - \bar{\eta}. \tag{1.7}$$

Here, ρ_l (lines/m) is the linear density of the array of dislocations, the angle β measures the degree of partial screw character ($\beta = 90^o$ for pure edge and $\beta = 0^o$ for pure screw), and γ is the angle the glide plane makes with the substrate interface.

The balance between dislocation excess energy and strain energy release results in an equilibrium degree of misfit strain in the epilayer. Figure 1.3 gives an example schematic of possible energy curves of a film calculated at two different film thicknesses. This figure illustrates that, for a sufficiently thin film (h in this example), the amount of strain energy relieved does not compensate the dislocation excess energy, and a film having no dislocations results. However, for a sufficiently thick film ($3h$ in this example), forming dislocations relieves strain energy faster than the dislocation excess energy increases, and an equilibrium degree of strain relaxation occurs. In this latter case, over half of the original misfit strain is relieved by dislocations. On the top axis, β measures the degree of partial screw character, and γ is the angle the glide plane makes with the substrate interface. For purposes of visualization, U_d is shown to be independent of film thickness, h, even though it has a logarithmic dependence, as in Eq. 1.6.

1.1.3 Critical Film Thickness

Under conditions of isotropic and homogenous elasticity, an analytical solution exists mapping the critical misfit strains, $\bar{\eta}_c$, at which dislocation formation is favorable as a function of film thickness [3]:

$$\bar{\eta}_c = \frac{1}{h}\left(\pm \frac{b}{(8\pi(1+\nu)sin(\beta)cos(\gamma)}\right) ln\left(\frac{4h}{b}\right). \tag{1.8}$$

The relationship in Eq. 1.8 shows that there is a nearly inverse relationship between the critical misfit strain and film thickness. If a film's thickness doubles, the misfit strains that can be sustained in the film decreases by approximately half, assuming the film thickness is large enough so that the logarithmic term varies slowly. Figure 1.4 gives an example state diagram for this relationship for the case of Si(001) epitaxy, with the white area denoting regions where no dislocations exist in the epilayer, and the gray area denoting regions where strain relaxation has occurred through formation of misfit dislocations.

1.1.4 Consequences for Ferroelectric Thin Films

The phenomena of epitaxy and strain relaxation have important consequences for the properties of ferroelectric thin films. The properties of these ferroelectrics are often strongly

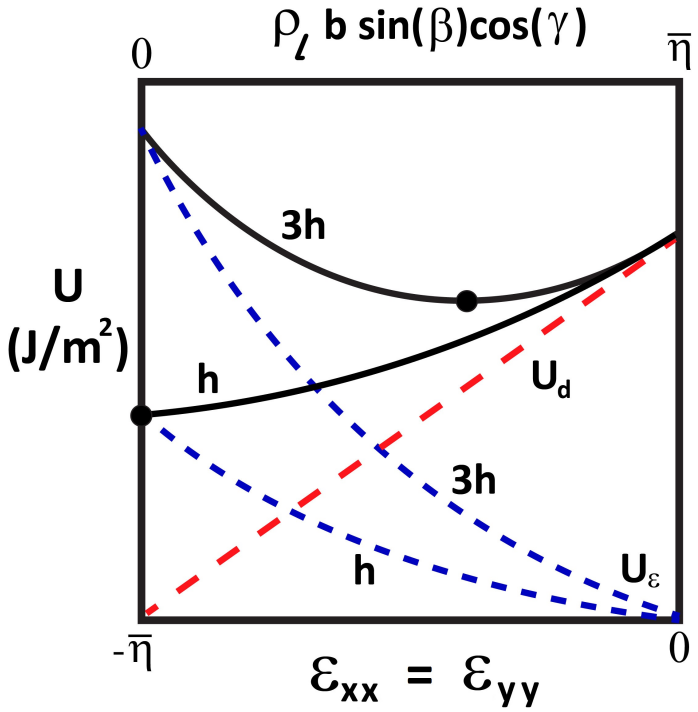

Figure 1.3: Film internal energy as a function of misfit strain. In this plot, $U = U_\epsilon + U_d$ is the total energy, as shown by the black solid line, U_d is the dislocation energy, as shown by the red dashed line, and U_ϵ is the film strain energy, as shown by the blue dashed line. Points of equilibrium strains for the two different film thicknesses are shown as filled circles. Redrawn, based on Fig. 6.25 from [3]

coupled to misfit strain. If this strain is reduced through strain relaxation, the polarization of the film will change as well. Thus, properties of the film can be very sensitive to the thickness at which the film is grown.

Epitaxial ferroelectric thin films offer a number of advantages compared to their bulk counterparts. As will be discussed in the next section in greater detail, the polar properties of a ferroelectric crystal couple strongly to its strain state. Often times, application of large amounts of non-hydrostatic strain can enhance polarization and lower the curie temperature compared to the bulk. Epitaxy provides the means by which strain conditions in a system may be tuned. Compared to bulk, in which cracking occurs for very small strains, thin films can withstand non-hydrostatic strains of several percent. Further, the growth orientation of a ferroelectric film can be controlled based on the preparation of the substrate. This is important when the property of interest is anisotropic, and a rotation of the film leads to a larger response in the direction of interest. The degree of strain and orientation can be precisely tuned in modern heteroepitaxy, leading to additional means by which properties of ferroelectrics can be improved. Lastly, epitaxial films can be grown atomically smooth and eliminate any grain boundaries. These properties lead to materials with desirably homoge-

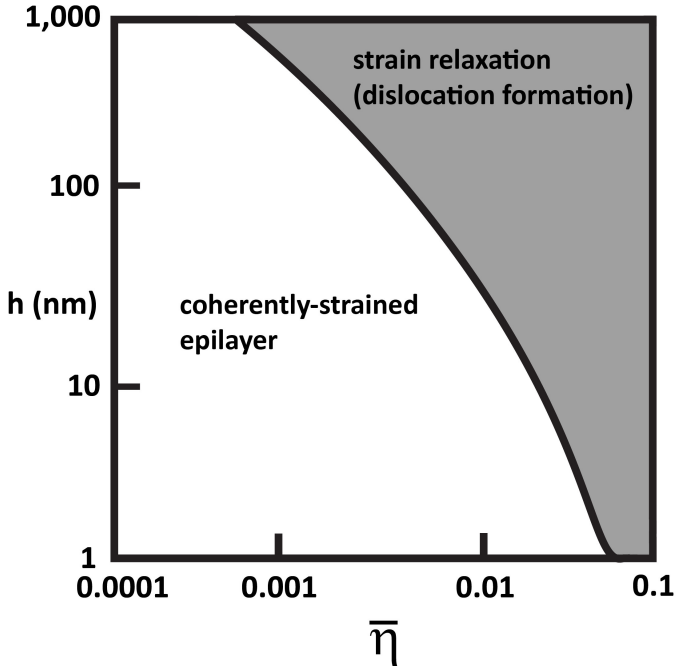

Figure 1.4: Relationship between critical thickness and degree of misfit strain for Si(001) epitaxy, with $\nu = 0.22$, $b = 0.38$ nm, $\gamma = 55^o$, and $\beta = 60^o$. Redrawn, based on Fig. 6.26 of Ref. [3].

neous properties.

1.2 Physics of Ferroelectrics

While the above section discussed the mechanical factors that determine a film's strain state under various epitaxial boundary conditions, it is the coupling of the mechanical strain with electro-static interactions in thin-film ferroelectrics that enable tuning of their functional properties. The following section provides a brief overview of the physics driving these polar response properties.

1.2.1 Macroscopic Polarization

Materials are composed of substituent particles having positive and negative charges. Charged particles generate electric fields in their vicinities, which results in electrostatic forces given by the Coulombic interaction. In insulators, the negatively charged electrons are strongly bound to the atomic nuclei, and the influence of a uniform electric field will displace positively charged particles in the direction of the field and negatively charged

particles in the opposing direction. This separation of charge results in an electric dipole moment, given by:

$$\mathbf{p} = \sum q_n \mathbf{r}_n, \tag{1.9}$$

where the summation is taken over all particles in the system, q_n gives the charge on the nth particle, and $\mathbf{r}_n$ is the position of the nth particle.

Each dipole moment formed within a material emits its own electric field given by:

$$\mathbf{E}(\mathbf{r}) = \frac{3(\mathbf{p}\cdot\mathbf{r})\mathbf{r} - r^2\mathbf{p}}{4\pi\epsilon_0 r^5}, \tag{1.10}$$

where ϵ_0 is the permittivity of free space. The macroscropic polarization, $\mathbf{P}$, is defined as the dipole moment per unit volume of a system. Whenever an electric field is applied to electrical insulators, or dielectrics, a macroscopic polarization develops. The connection between polarization, $\mathbf{P}$, and an applied electric field, $\mathbf{E}$, is characterized in the simplest cases by the constant of dielectric susceptibility, χ, such that:

$$\mathbf{P} = \epsilon_0 \chi \mathbf{E}. \tag{1.11}$$

In more complicated cases in which the developing polarization is not always aligned with the direction of the applied electric field, the dielectric susceptibility becomes a rank three tensor.

1.2.2 Response Properties

In general, the various mechanical, thermal, electric, and magnetic properties of materials are dependent on each other. Some commonly coupled material properties are illustrated in the Heckman diagram [5] shown in Fig. 1.5. As an example, when a stress, σ, is applied to a material, this material will deform, giving way to a distribution of strain, ϵ. This distribution will depend on the mechancial response properties of the material, such as the stiffness tensor in the case of a linear response, that mathematically relate stresses and strains.

Couplings between properties do not have to remain within one property group. For example, mechanically compressing a gas can affect its temperature (thermodynamic coupling), applying a stress to a material can generate a polarization through the piezoelectric effect (electro-mechanical), and applying an electric field to a material can cause that material to evolve or absorb heat (thermo-electric). These less common couplings are critical to some of the most important technological devices created in recent decades, such as sensors, memory storage devices, and micro-electro-mechanical devices [1].

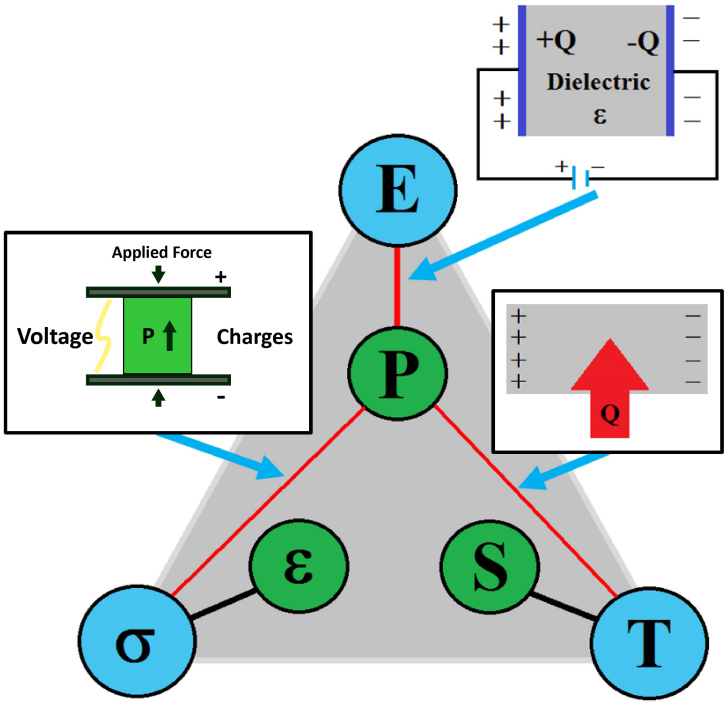

Figure 1.5: A Heckman diagram illustrating some of the commonly coupled properties within materials. The red lines illustrate some of the most important electric couplings for ferroelectric materials used in technological applications, as well as schematics showing the physical processes associated with the couplings.

1.2.3 Ferroelectrics and Switching

Ferroelectric materials are characterized by the unique nature of their couplings between the macroscopic electric field and polarization. For a subset of dielectrics, a macroscopic polarization is present within the material even when no electric field has been applied. In these cases, the materials retain spontaneous polarizations, the presence of which is one of the requirements of ferroelectrics. An additional requirement for a material to be a ferroelectric is that application of a sufficiently strong electric field must be able to "switch" the material between two or more stable atomic arrangements, each having a spontaneous polarization [6]. As a result of this property, ferroelectrics exhibit a hysteresis loop when the applied electric field is cycled back and forth between opposing directions. Figure 1.6 shows a schematic of this process.

Within the simplified schematic of Fig. 1.6, the material begins in state A with zero applied field, a spontaneous polarization of P_s, and positively ions shifted slightly upward relative to negatively charged ions. In state A, the majority of ferroelectric domains within

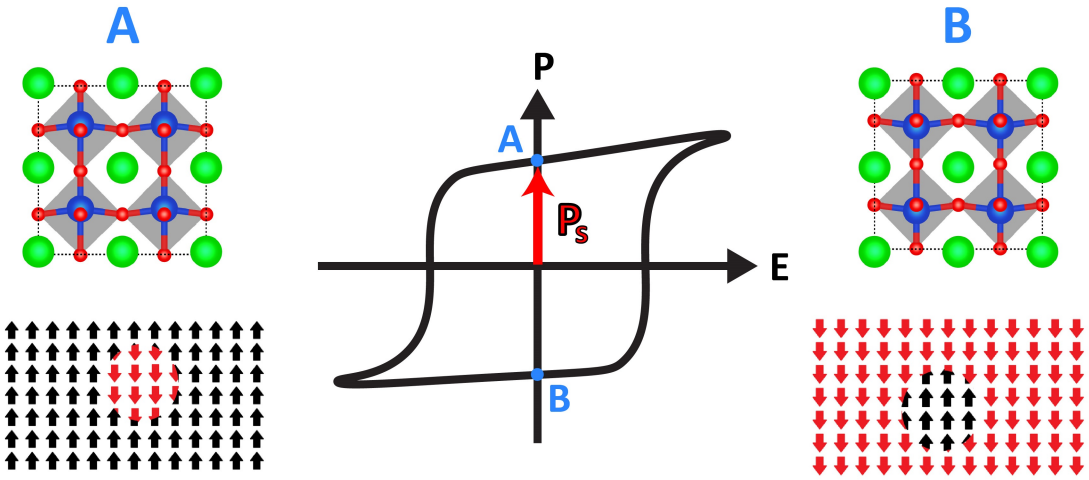

Figure 1.6: A schematic of ferroelectric switching and the hysteresis loop. The middle shows the relation between polarization and electric field, the top left and top right schematics show example atomic arrangements in the poled-up and poled-down states, and the bottom left and bottom right schematics show examples of domains forming of opposite polarization within the material.

the material are aligned upward (red arrows), with a small number of minority domains aligned downward (black arrows). Ferroelectric domains are defined as regions of crystal in which the spontaneous polarization is oriented in the same direction, which are separated from differently oriented domains by domain walls. As an electric field (E) is applied in the direction of the spontaneous polarization (positive values of the x-axis), the polarization increases slightly until it saturates, as the domains of the material have all aligned their polarization. If the electric field is then directed opposite to the direction of P_s and is sufficiently strong, domains will begin to nucleate having polariziations aligned opposite to the original direction of P_s, or downward in this case. At a critical value of E, the majority of domains have their polariziations aligned with E, and the material rapidly undergoes ferroelectric switching. If the electric field is then lowered back to zero, the material is in state B shown in Fig. 1.6. In this state, the majority of domains are now aligned downward, with a small minority of domains aligned upward.

1.3 Applications of Thin-Film Ferroelectrics

The ability to tune the polar properties of thin-film ferroelectrics through the strain state of the system has many promising technological applications, some of which are already used in modern devices. There are many examples in the literature of interesting phenomena that can result from misfit-strain control of ferroelectrics. Because of the expanded tunable parameter space created when the extra degree of freedom of strain tuning is added, computational methods for materials design become increasingly important due to

their low cost compared to experiments.

1.3.1 Misfit-Strain Controlled Phenomena

There exist many examples in the literature of how the coupling of misfit strain and polar properties in thin-film ferroelectric can be exploited for device applications. The general theme of these applications is that thin-films enable property control unachievable in bulk systems, and the constrained dimensions of thin films offer the additional advantage of ammenability to microelectronic devices. The effect of misfit strain on the response properties of $SrTiO_3$ offers a clear example.

Systems having a ferroelectric to paralectric transition near room temperature can be very useful for high-frequency microelectronic devices. This is because of the high degree of dielectric tunability these materials can provide, with small changes in a bias volatage applied across the material resulting in large shifts in dielectric constant. The traditional method of tuning the ferroelectric transition temperature to be near room temperature is by chemical substitional. An example of this is the solid solution of $BaTiO_3$ with $SrTiO_3$. However, it is desirable to find alternatives to this approach, as compositional heterogeneity in the solution can significantly broaden the phase transition temperature range and degrade device performance [7]. One such alternative is through strain tuning, as Haeni *et al.* demonstrate for the case of $SrTiO_3$ thin films. In bulk form, $SrTiO_3$ is a paraelectric material at all temperatures. However, thin films of $SrTiO_3$ epitaxially grown at 1% tensile misfit strain allow this material to exhibit room-temperature ferroelectricity and a high degree of dielectric tunability [7]. The application of misfit strain drives a polar instability in $SrTiO_3$, rendering the cubic centro-symmetric $Pm\bar{3}m$ phase unstable. The misfit phase diagram schematic in Fig. 1.7 illustrates the significant impact biaxial strain can have on the phases of $SrTiO_3$. The modest application of half a percent tensile strain at room temperature drives a transition to a ferroelectric phase.

Another area in which strain-controlled phenomena are of special technological interest is multiferroic materials. These are materials in which magnetism and ferroelectricity coexist, with the potential for magnetic states to strongly couple to electric fields. This coupling allows for the potential to manipulate the magnetic state of a system through application of an electric field, which would be very useful in the context of computer memory devices. In Ref. [8], Martin *et al.* show that a perovskite-derivative phase of $PbVO_3$, which is unstable under ambient conditions, can be stabilized when grown under epitaxy on an $LaAlO_3$ (001) substrate. This phase is strongly polar, and has a single occupied *d*-state, making it a candidate multiferroic system. This work illustrates the important phenomenon of phase stabilization through application of particular epitaxial boundary conditions. Further, the phase stabilized has promising properties unachievable in its bulk form. The existence of a polar $PbVO_3$ multiferroic-candidate system under biaxial strain is just one example of the

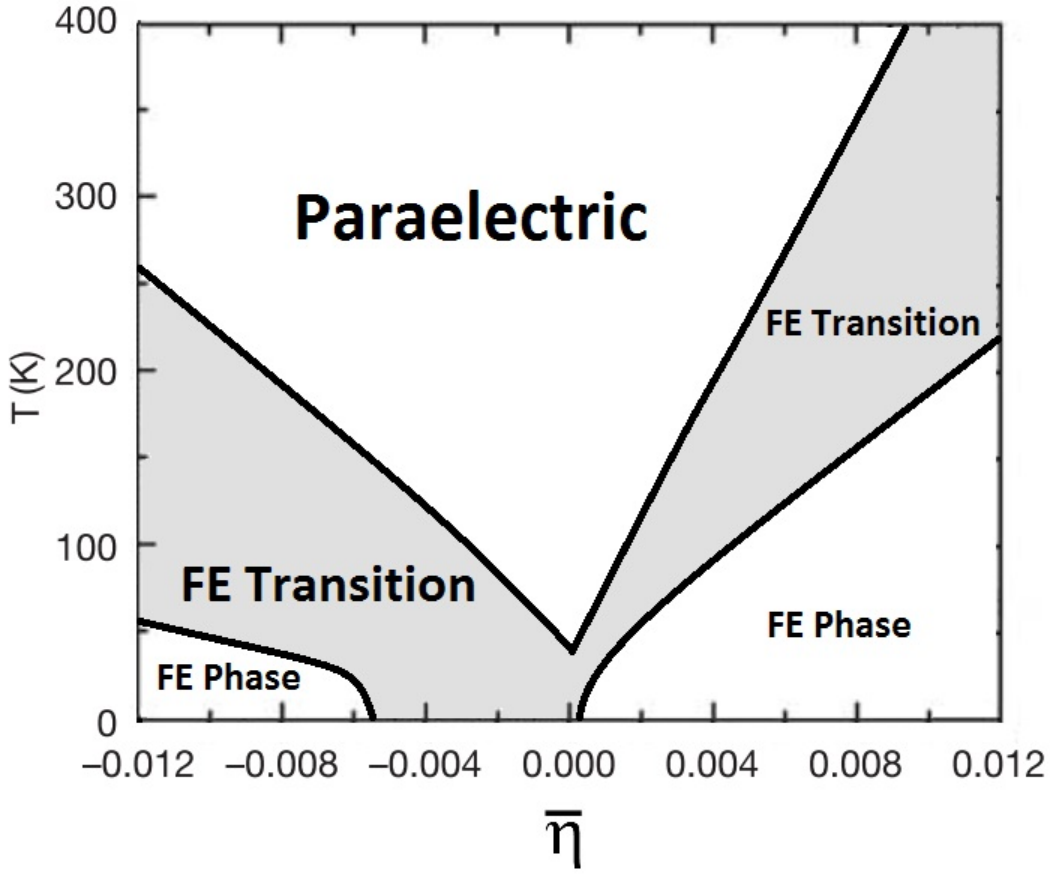

Figure 1.7: A schematic of the phase diagram of $SrTiO_3$ as a function of misfit strain. At room temperature, $SrTiO_3$ is paraelectric, but application of moderate biaxial compression or tension drives a transition to a ferroelectric phase. Redrawn based on Fig. 1 in [7].

potentially vast collection of unexplored systems exhibiting novel properties under conditions of epitaxy.

1.3.2 Role of First-Principles Methods

The overarching goal of the present work is to develop and apply first-principles-based workflows for determining the properties of thin-film ferroelectric materials as a function of applied misfit strain. The combined parameter space of composition and misfit strain is difficult to systematically explore through experimental methods, and many yet-unexplored thin-film systems could exhibit interesting phenomena similar to those described in the previous section. By calculating and making available the properties of a large number of thin-film systems, insights into the physics driving thin-film ferroelectrics can be attained, and materials discovery can be facilitated.

A significant body of literature has laid the groundwork for calculating the properties of thin-film ferroelectrics as a function of misfit strain. In the earliest studies, King-Smith and Vanderbilt developed the KSV method for mapping the energy landscape and ground-state phases of ferroelectric perovskite oxides using expansions of the total energy with respect to the amplitudes of unstable phonon modes and strain [9]. Dieguez et al. [10] later expanded this approach to include the misfit strain as a degree of freedom, and were thereby able to calculate the ground-state phases of eight perovskite oxides as a function of misfit strain. Additional studies have produced similar misfit-strain phase diagrams for a broader range of compositions [11–15] by means of direct DFT calculations. These phase diagrams are a useful guide for thin-film growth experiments of coherently-strained perovskite oxides on substrates, as they indicate the degree of polarization and phases to be expected. However, these studies only treat a small range of compositions, only consider the (001) growth orientation, and neglect the potential impact of antiferrodistortive distortions that can strongly affect the polarization of perovskite oxides [16]. The work in this dissertation aims to expand on these limitations by developing automated methods for computing thin-film properties, considering a more complex range of competing thin-film phases, and by studying unexplored compositions.

1.4 Dissertation Outline

The remainder of this dissertation is organized as follows. Chapter 2 provides an overview of the computational methodology that underlies all of the work in this thesis, i.e., the first-principles framework of electronic density functional theory (DFT). Chapter 3 presents an automated computational approach for determining the polar and energetic properties of the ground-state structures of ferreoelectric perovskite oxide thin-films. This approach is applied to 42 perovskite oxide thin-film systems, and results for representative individual thin-film systems are discussed. Major trends in the polarization and energetic data across the various compositions are presented and the causes of these trends are discussed.

In chapter 4, an automated approach for treating thin-film ferroelectrics with non-zone-centered distortions is presented. This approach is based on expansions of the total energy as a function of strain and displacement-mode degrees of freedom. The approach is applied to three systems, $SrTiO_3$, $CaTiO_3$, and $SrHfO_3$, in a demonstration of its effectiveness. The effect of non-zone-center distortions, such as octahedral rotations and *A*-site anti-polar distortions are discussed in detail.

Chapter 5 describes a computational effort to discover perovskite-based vanadate thin-films alternative to the previously studied PVO system. Properties of the perovskite-based epitaxial structures of KVO_3 and $NaVO_3$ are calculated as a function of biaxial strain applied in the (100) plane. Electronic structures of the minimum energy epitaxial phases for these two systems are calculated and compared to that of PVO. Finally, chapter 6 gives a summary highlighting the major results and conclusions from chapters 3, 4, and 5, and directions for future work related to these research efforts are suggested.

CHAPTER 2

Theoretical Framework

2.1 First-Principles Methods

Computational modeling plays an important role in modern materials research. Results computed from theory can often supplement those from experiment in useful ways, and the precise control offered by theoretical methods can provide data that can be highly challenging to obtain directly by experimental measurements. Computational simulations of materials systems can take many forms, each categorized broadly by the characteristic length scale considered by the model, as well as whether or not empirical data must be used to fit the model. Those which do not rely on input from experimental observations are termed first-principles computational modeling methods, as they are built starting with the fundamental quantum mechanical equations that describe the fundamental atomic interactions in a material.

In the study of epitaxial ferroelectric thin-films, the properties of interest are sensitively dependent on the interactions amongst the system's electrons and atomic nuclei. Because of this, accurate descriptions of the structures, polarizations, and energies of these systems requires the use of quantum-mechanical theory, as practically implemented through the formalism of density functional theory (DFT). The approaches used in chapters 3-5 make extensive use of DFT in order to calculate various properties of ferroelectric thin-films. In the following subsections, a brief introduction to DFT and its quantum mechanical basis is provided.

2.1.1 Schrödinger Equation for a Solid

A key quantity that must be accurately determined when modeling solids is the lowest, or ground-state energy of a collection of atoms as a function of their positions. This quantity is called the *adiabatic potential energy surface* of the atoms, and it depends on both electronic and nuclear interactions and is described through the formalism of quantum mechanics. The ground-state energy of an arbitrary system of multiple nuclei interacting with N electrons is given (neglecting electron spin) by the lowest eigenvalue of the general time-independent Schrödinger equation:

$$\left[-\frac{\hbar^2}{2m}\sum_{i=1}^{N}\nabla_i^2+\sum_{i=1}^{N}V(\mathbf{r}_i)+\sum_{i=1}^{N}\sum_{j<i}U(\mathbf{r}_i,\mathbf{r}_j)\right]\psi=E\psi, \tag{2.1}$$

Here, m is the mass of an electron, V is the potential energy surface created by the atomic nuclei, U is the energetic interaction term between two electrons, and ψ is the electron wave function. This wave function is a function of the positions of the N electrons in the system, *i.e.* $\psi(\mathbf{r}_1,...,\mathbf{r}_N)$. The first term on the left side of Eq. 2.1 accounts for the kinetic energy of the electrons, the second for the interaction energy between the electrons and atomic nuclei, and the third for the interaction energy between electrons. Due to the many-body nature of the problem, Eq. 2.1 is largely insoluble. DFT reformulates this problem in a way that the ground-state energy can be computed for complex systems, given certain approximations, as described in the next section.

2.1.2 Density Functional Theory

Density functional theory is a first-principles computational modeling technique that allows for efficient and accurate calculation of the ground state electronic structure of condensed matter. Its formalism provides a practical means of computing the energy for a many-electron system with the Schrödinger equation given mathematically by Eq. 2.1 [17]. The usefulness of DFT has been demonstrated extensively in recent decades. For instance, DFT has been used to predict crystal structures, calculate band structures, explore diffusion properties, and determine surface energies [18]. In the realm of materials discovery, DFT is increasingly being used for the computational design of lithium-ion batteries, hydrogen production and storage materials, thermoelectric materials, and various other important materials technologies, as discussed in Ref. [19] and references therein.

Within the DFT formalism, matter is modeled under a few very fundamental atomistic principles; namely, atomic nuclei can be (usually) treated as classical particles with a positive charge and set mass, electrons are spin-one-half particles obeying the Pauli Exclusion Principle and described kinetically by quantum mechanics, and interactions are governed by Coulombs law [18]. DFT is general to all elements and can be used to describe materials with metallic, covalent, or ionic bonding character.

Density funcitonal theory calculations are based upon the theorem of Hohenberg and Kohn (1961), stating that, for a given external potential, such as the Coulomb potential of atomic nuclei, the energy of the corresponding electronic system is a functional of the electron density within a solid. Deviations of this density from that associated with the ground state lead to positive definite changes in the total energy of the system. Thus, the ground-state energy can be found by searching through possible densities, $n(\boldsymbol{r})$, until E_{total} is minimized [18]. The energy functional of a solid can be written as:

$$E\left[n(\boldsymbol{r})\right]=T_0\left[n(\boldsymbol{r})\right]+E_H\left[n(\boldsymbol{r})\right]+U_{ext}\left[n(\boldsymbol{r})\right]+E_{XC}\left[n(\boldsymbol{r})\right]+E_{ion}, \tag{2.2}$$

where

$$n(\boldsymbol{r}) = \sum_{occ} |\phi_i(\boldsymbol{r})|^2 \tag{2.3}$$

is the electron density, and $\phi_i(\boldsymbol{r})$ are the occupied Kohn-Sham states. The kinetic energy term is defined as:

$$T_0[n(\boldsymbol{r})] = -\left(\frac{\hbar^2}{2m}\right) \sum_{occ} \int \phi_i^*(\boldsymbol{r}) \nabla^2 \phi_i(\boldsymbol{r}) \, d\boldsymbol{r}. \tag{2.4}$$

The Hartree expression for the Coulomb interaction energy between the electrons is given by:

$$E_H[n(\boldsymbol{r})] = \left(\frac{e^2}{2}\right) \iint \frac{n(\boldsymbol{r}) n(\boldsymbol{r}')}{|\boldsymbol{r} - \boldsymbol{r}'|} d\boldsymbol{r} d\boldsymbol{r}', \tag{2.5}$$

and

$$U_{ext}[n(\boldsymbol{r})] = -e \int n(\boldsymbol{r}) V_{ext}(\boldsymbol{r}) d\boldsymbol{r} \tag{2.6}$$

corresponds to the interaction of the electrons with the potential field of the nuclei.

The term $E_{XC}[n(\boldsymbol{r})]$ that appears in the total energy functional includes the exchange energy, which is the energy obtained because the electrons obey the Pauli principle, and the correlation energy, which accounts for the fact that the energy due to electron interactions is not accurately described by the Hartree energy. This functional cannot be precisely determined, but many useful approximations have been applied. A few examples of functionals commonly used are given in Section 2.1.3.

By substituting the various separate terms of Eqs. (2.3)-(2.6) back into the expression for the total energy given in Eq. (2.2), and upon minimizing the energy, it is found that the wave functions satisfy Schrodinger-like equations called the Kohn-Sham equations:

$$-\left(\frac{\hbar^2}{2m}\right) \nabla^2 \phi_i(\boldsymbol{r}) + v_{KS}(\boldsymbol{r}) \phi_i(\boldsymbol{r}) = \epsilon_i \phi_i(\boldsymbol{r}). \tag{2.7}$$

Density funcitonal theory is put into practice using an iterative four-step approach [17]:

1. Define a trial density $n(\boldsymbol{r})$.
2. Solve the Kohn-Sham equations (2.7) using this guessed $n(\boldsymbol{r})$ to find the Kohn-Sham wave functions $\phi_i(\boldsymbol{r})$.
3. Calculate a new $n'(\boldsymbol{r})$ from these wave functions.
4. If $n'(\boldsymbol{r})$ and $n(\boldsymbol{r})$ are equal within a defined tolerance, $n(\boldsymbol{r})$ is that of the ground state, and $n(\boldsymbol{r})$ is used to determine E_{total}. If not, update trial $n(\boldsymbol{r})$ and reiterate starting with step two.

It is noted that DFT calculations cannot give exact solutions to the Schrodinger equation because $E_{XC}[n(\boldsymbol{r})]$ is not known exactly. Thus, comparisons to experiment or higher levels of theory must be used to determine the degree of accuracy of DFT for a given class of materials.

2.1.3 Common Exchange-Correlation Functionals

Because the exchange correlation functional, $E_{XC}[n(\boldsymbol{r})]$, cannot be determined exactly, one must choose the level of approximation used for this term. In choosing how to approximate the exchange correlation functional, a balance must be maintained between how much computational complexity the term requires and how much physical information it carries. The most basic approach is to use the Local Density Approximation (LDA), which assumes that the local contribution to the exchange-correlation energy is identical to that of a uniform electron gas of the same density [18]. Under the LDA, the local exchange-correlation potential takes the form of:

$$V_{XC}^{LDA}(\boldsymbol{r}) = V_{XC}^{electron\ gas}(\boldsymbol{r})\left[n(\boldsymbol{r})\right]. \tag{2.8}$$

This approximation is astonishingly accurate for inhomogeneous systems such as crystals, and it is thus practically applied in many studies. Beyond the LDA, the generalized gradient approximation (GGA) includes information related to the spatial inhomogeneity of the electron density through its local gradient, as follows:

$$V_{XC}^{GGA}(\boldsymbol{r}) = V_{XC}(\boldsymbol{r})\left[n(\boldsymbol{r}), \nabla n(\boldsymbol{r})\right]. \tag{2.9}$$

Although GGA includes more physical information about the system than LDA, it is not necessarily more accurate, as discussed in more detail below in the case of perovskite-based oxide compounds. There are many ways to fit the information carried in the GGA functional, but one of the most common is the Perdew-Burke-Ernzerhof (PBE) functional, due to its high accuracy and computational efficiency. Finally, inclusion of the Laplacian of the electron density, $\nabla^2 n(\boldsymbol{r})$ leads to meta-GGA functionals. One recently developed example is the strongly constrained and appropriately normed (SCAN) functional, which has been shown to systematically improve over LDA/PBE for a variety of systems [20].

When calculating the properties of perovskite oxides, such as lattice parameters and spontaneous polarization, LDA tends to show better agreement with experimental results [20]. GGA tends to underperform LDA in predictive accuracy for these properties in this class of compounds, because of the so-called 'supertetragonality' problem, whereby the c/a ratio is signficantly overestimated [21]. SCAN meta-GGA functionals tend to perform the best for perovskite-structured oxides, usally representing modest improvement over LDA [20], but with an associated increase in computational resources required. For most of the work in this dissertation, LDA is used. In a few cases in the work presented in this dissertation, SCAN is applied to ensure the results are not highly sensitive to choice of functional.

2.1.4 Density Functional Perturbation Theory

While density functional theory can provide information about the groundstate electron density and total energy, it is formally unable to describe excited states of a system. For small perturbations of the system, one can apply density functional perturbation theory (DFPT) in order to predict various response properties [22]. The types of properties that can be computed include first order responses, such as forces or stresses, second order, such as phonon dynamical matrices, elastic constants, or piezoelectric tensors, and third order responses, such as non-linear dielectric susceptibilities. Within this dissertation, DFPT is primarily used to calculate the force-constant matrix of systems in order to verify their dynamic stability with respect to atomic displacements. For a comprehensive treatment of DFPT, see Ref. [22].

2.2 Modern Theory of Polarization

For non-periodic systems with no net charge, such as molecules or nano-particles, Eq. 1.9 can be easily evaluated in order to determine the electric dipole moment, and thus the polarization of the system. The summation is simply taken over the collection of charges at the respective positions of each. However, for bulk solids, such as the crystals dealt with in the present work, Eq. 1.9 can no longer be simply applied to evaluate the net dipole moment of the system. Intuitively, one would start by evaluating this expression over some periodic unit cell describing the crystal. However, if this method is performed, one will end up with different values of dipole moment per unit cell depending on choice of the unit cell [23]. For an example of this inconsistency in the simple case of a one-dimensional chain of atoms, see Ref. [23].

To rectify this problem, the *Modern theory of polarization* [24] was developed. In this theory, rather than probing the absolute value of polarization in a system, changes in polarization are considered. These changes are well-defined, and can be compared to experimentally measurable observables. The Berry phase approach is used in this work whenever polarization of ferroelectric thin films is performed. The corresponding calculation results in a lattice of polarization vectors, rather than a single vector, with repeat units defined modulo a polarization quantum given by $e\mathbf{R}_i/\Omega$, where e is the fundamental unit of charge on an electron, $\mathbf{R}_i$ is one of three lattice vectors of the crystal, and Ω is the unit cell volume. As a result, care must be taken to select the appropriate vector from the polarization lattice. The simplest approach, which is applied in this work, is to repeat the calculation for a nearby non-polar reference state, and to find the shortest branch connecting the two values. The difference between these two polarization vectors is then taken to be the polarization of the system, as long as the actual polarization is not larger than the polarization quantum, which tends to be large compared to values of observed polarization. For a comprehensive treatment of this approach, see Ref. [24].

2.3 High-Throughput Computing

One of the most powerful aspects of first-principles methods is that many calculations can be automated and applied to a large number of materials with relative ease as compared to experimental approaches. The ability to calculate properties over a large number of materials is appealing for the purposes of screening the collection of candidate systems, thereby reducing the search space significantly and accelerating design and optimization of new materials [25]. Many tools have been developed in order to facilitate these high-throughput approaches, such as the Python Materials Genomics (pymatgen) library [25], a robust open-source Python library for materials analysis. In recent years, multiple initiatives have been developed with the aim to use high-throughput first-principles calculations to aid material design through generation of large databases of materials properties. For example, the Materials Project [26] strives to calculate the properties of all known inorganic materials and make this data publicly available to the scientific community. To date, this project has screened over 100,000 compounds, with properties including ground-state phases, elastic constants, and piezoelectric tensors [27, 28].

The work presented in this dissertation is intended to provide similar workflows for the high-throughput calculation of properties relevant to the design of ferroelectric thin-films. The goal of producing this data is to guide the discovery and design of this technologically important class of materials. Although application of the workflows described in this work are only applied to a handful of systems, the methods are created with scaling in mind, having the potential to be applied to a vast number of compositions with minimal alteration of the underlying calculation framework.

CHAPTER 3

Orientation-Dependent Properties of Epitaxially Strained Perovskite Oxide Thin Films

3.1 Motivation and Overview

The discovery of new functional materials (*e.g.*, ferroelectrics, ferromagnets, and ferroelastics) has periodically led to paradigm shifts in technological applications. For example, the technological value of the ferroelectric effect was not realized until the discovery of $BaTiO_3$, a robust and stable ceramic ferroelectric [1]. This led to a rapid proliferation of new devices that are pervasive in many modern technologies [29]. Subsequent searches for other ferroelectrics focused primarily on tuning composition, leading to the discovery of a number of other useful materials, such as $PbZr_{1-x}Ti_xO_3$ [30]. Despite the immense impact of finding next generation functional materials, the search effort has relied extensively on serendipitous discoveries, rather than being based on a systematic exploration over the relevant structural and compositional spaces available.

In recent decades, focus has been placed on the integration of ferroelectric thin films into electronic devices [1]. The constrained dimensions of these films make them amenable to device miniaturization. Furthermore, compared to bulk ceramics or single crystals, ferroelectric thin films offer novel routes to property tuning [31]. One such route is applied strain. Ferroelectrics grown as coherently strained thin films can withstand non-hydrostatic strains of several percent [2]. This biaxial strain is provided by the lattice mismatch between the film and the single-crystal substrate, on which the film is grown. Recent improvements in thin-film growth techniques have enabled the direct exploitation of misfit strain in order to finely tune the properties of oxide films [32]. As one example, Haeni *et al.* demonstrated that $SrTiO_3$, normally a paraelectric at all temperatures, exhibits room temperature ferroelectricity and dielectric properties that are promising for device applications when epitaxially grown at 1% tensile misfit strain [7]. Another route to property tuning is the control of film orientation [33–36]. By changing the orientation of the substrate, the thin film is subjected to

The work in this chapter was published by T. Angsten, L. W. Martin, and M. Asta in Physical Review B **95**, 174110 (2017), and is reproduced here with permission of the co-authors.

different mechanical boundary conditions that can result in the stabilization of entirely different crystal symmetries [37]. For example, Wu *et al.* showed, using a Landau-Devonshire based thermodynamic model, that the strain-temperature phase diagram of $BaTiO_3$ exhibits significantly different phases and physical properties when subjected to (100), (110), and (111) epitaxial mechanical boundary conditions [38]. More comprehensive reviews of the observed effects of strain and orientation on the phases and properties of thin films, along with a wide range of relevant examples, can be found in Refs. [2, 4, 31, 39].

The advent of integrated complex-oxide thin films has created a demand for new materials with properties well-suited to the wide array of potential applications [40]. However, just as with bulk ferroelectrics, the search for improved ferroelectric thin-film materials has relied upon chance discovery or incremental improvement of well-known materials. Furthermore, the majority of experimental thin-film growth has focused on (100)-oriented films of well-known perovskite oxides over a small range of strain [2, 31, 40]. Given the recent experimental work demonstrating the unique properties of coherently strained films grown on (110) and (111) substrates [34–36], as well as the possibility of observing novel phases at large misfit strains [41], it is clear that the search for new ferroelectric thin-film materials would benefit from a systematic exploration of the expanded parameter space associated with these materials. One route to a more thorough exploration is provided by automated first-principles computational approaches.

Automated workflows based on density-functional-theory methods have been developed and applied in high-throughput searches for new materials, in applications spanning energy, structural, and functional materials (*e.g.*, Refs. [42–46], and references therein). Furthermore, previous theoretical work has developed and applied first-principles methods for determining how the structural and polar properties of perovskite thin films depend on epitaxial strain [9–15, 24]. In these methods, epitaxial constraints are imposed on the in-plane lattice vectors of a bulk periodic crystal, thereby isolating the effect of strain from other factors associated with the substrate/film interface and film surface [4]. The result is a mapping of the minimum energy phase and corresponding polarization as a function of misfit strain.

Despite the existence of a first-principles methodology for modeling ferroelectric thin films, high-throughput approaches based on this methodology have not been systematically applied to aid in their design by screening over a large number of epitaxial systems. Similar to the situation in experimental studies summarized above, the focus of prior theoretical studies has been primarily on a small set of commonly grown perovskites on substrates with square-lattice symmetry, *i.e.*, (100)-growth orientations. Of the first-principles studies that have looked at the effects of epitaxial strain applied under (110)- and (111)-oriented growth, only very commonly studied perovskites, such as $BaTiO_3$ and $PbTiO_3$, have been treated [47–49]. A systematic application of current first-principles computational methods to a wide range of systems would provide a preliminary map of ferroelectric polar properties over the thin-film parameter space, which could prove useful to experimentalists attempting to discover new and improved ferroelectric thin-film materials. This map would ideally screen over a large range of the parameter space, weeding out systems unlikely to have interesting properties, and identifying a subset of systems worth more comprehensive study.

In this work, a first step is taken toward generating such results by applying an automated first-principles computational workflow, based on a methodology similar to that employed by Diéguez *et al.* [15], to study the structure and polarization of non-magnetic ferroelectric oxide films with perovskite-derived structures. This work extends previous related studies [9–15] by considering an expanded range of compositions and by modeling the effects of epitaxial strain in the (110)- and (111)-oriented films (Sections 3.3.2 and 3.3.3), in addition to the commonly studied (100)-oriented films. In all, 14 perovskite oxides are considered with epitaxial constraints imposed on the (100), (110), and (111) planes of the cubic perovskite structure. Each of these 42 (14×3) thin-film systems are modeled over an 8% (-4 to 4%) misfit strain range.

3.2 Approach

An automated density functional theory (DFT)-based workflow has been developed and used to investigate a broad composition-strain-orientation parameter space in order to elucidate fundamental physical trends, as well as search for previously undiscovered polar phases that have the potential to be realized in thin-film growth experiments. To achieve this, the procedure described in Section 3.2.2 is used to predict the minimum energy phases and corresponding structural, energetic, and polarization properties for a number of thin-film systems subjected to various misfit strains and growth orientations. In order to make the search over such a broad parameter space computationally feasible, this workflow employs simplifying assumptions related to the types of crystal structures considered.

Specifically, consideration is given only to structures that can be derived from the primitive cell of the cubic perovskite compound through application of homogeneous strains and atomic displacements, as illustrated in Fig. 3.1. Thus, this work neglects the consideration of effects such as octahedral rotations and anti-ferroelectric ordering. These symmetry-lowering effects are expected to suppress polarization rather than enhance it [16], allowing for results in this work to effectively provide upper bounds to the polarization behaviors of the systems considered. Those systems found to be interesting from this initial level of screening can be studied in further detail by applying more rigorous approaches, such as supercell, phonon [50], and molecular dynamics calculations [51], as well as global structure searching algorithms [52–54]. The goal of this effort is to demonstrate a method for such a first level of screening, as well as to identify fundamental trends of thin-film polarization behavior resulting from variations in composition, misfit strain, and orientation, without the additional effects associated with the structural complexities listed above.

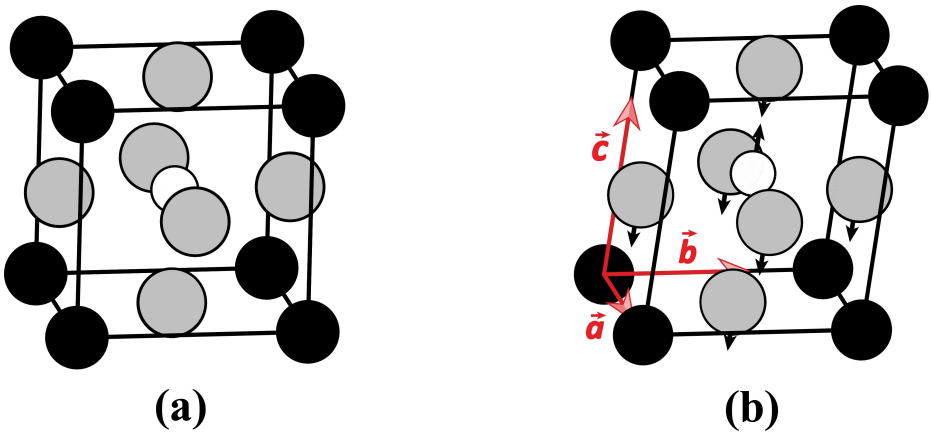

Figure 3.1: a) Perfect cubic perovskite structure with the A cation at the corners (black), the B-cation in the body-center (white), and the oxygen atoms at the face centers (gray). b) A possible perovskite-based five-atom unit cell relaxed under (100)-growth orientation constraints. Relative to the cubic structure, this cell has undergone a compressive biaxial misfit strain of $\bar{\eta}$, tensile out-of-plane strain, out-of-plane shear strain, and various (exaggerated) atomic displacements. For (100)-orientated systems, $\vec{a} = \vec{b} = \vec{a}_0 * \bar{\eta}$, and $\vec{c}$ is free to relax. This figure was created using VESTA [55].

3.2.1 Selection of Compositions

ABO_3 compositions in which the B cations have d^0 electronic configurations in their formal charge state are considered. This subset enables a simplification of the workflow due to the absence of spin-polarized states and the need to consider magnetic-ordering degrees of freedom. Furthermore, only compositions having Goldschmidt tolerance factors [56] ranging between 0.95 and 1.1 are considered. The tolerance factor t is defined as follows:

$$t = \frac{R_{A-O}}{\sqrt{2}R_{B-O}},$$

where R_{A-O} and R_{B-O} are the ideal A-O and B-O perovskite structure bond lengths calculated from the bond valence model [57, 58]. For $t > 1$, the B-cation is too small for its octahedral cage, favoring a polar distortion. For $t < 1$, octahedral rotations are likely to optimize the A-cation bonding with its 12 neighboring oxygen atoms [59]. For deviations of t far from unity, the perovskite-based structure is likely to become energetically unfavorable relative to other polymorphs. By considering systems with tolerance factors in a constrained range, the chance of a non-perovskite based polymorph competing with the thin-film phases considered in this work is reduced.

3.2.2 Calculation Procedure

For each composition considered, the DFT-optimized perfect cubic perovskite structure (space group $Pm\bar{3}m$) is the reference used for reporting misfit strain. To calculate the

ground-state phase under particular epitaxial conditions, misfit strain is applied to the appropriate plane [one of (100), (110), or (111)] of the reference cubic structure, and the symmetry is broken by displacing the B-cation and oxygen atoms (see next paragraph for details). The positions of all atoms and the lattice vectors are then relaxed until the Hellmann-Feynman forces and out-of-plane stress tensor components converge to magnitudes within 0.001 eV/Å and 0.005 eV/f.u., respectively, where eV/f.u. is per five-atom formula unit. These relaxation criteria give energies converged to within at least 0.05 meV/f.u., although in almost all cases the forces and stresses are much less than these thresholds, and better convergence is achieved.

In performing the structural relaxations, the mechanical boundary conditions associated with epitaxial growth for a prescribed orientation are enforced. To clearly define these constraints, a convention is used wherein the x, y, and z components of the strain and stress tensors correspond to the choice of axes illustrated in Fig. 3.2. In terms of these coordinate systems, the mechanical boundary conditions are defined as:

$$\epsilon_{xx} = \epsilon_{yy} = \bar{\eta}, \quad \epsilon_{xy} = 0$$
$$\sigma_{zz} = \sigma_{yz} = \sigma_{xz} = 0$$

where ϵ and σ are the rotated strain and stress tensors, respectively. Thus, the mechanical boundary conditions are different for each of the three orientations considered in this work. All predicted phases resulting from the structural relaxations correspond to the minimum energy perovskite-based, single-domain, homogeneously-strained, periodic structures under epitaxial mechanical boundary conditions and at zero temperature. For all substrate orientations, the misfit strain is calculated as $\bar{\eta} = a/a_0 - 1$, where a_0 is the lattice constant of the cubic reference structure, and a is the necessary lattice constant of a cubic substrate that would impart the given misfit strain. To clarify, an epitaxial lattice constant with a given value a of 4.0 Å refers to the same cubic substrate for the (100), (110), and (111)-growth orientations, the difference being the preparatory cut of such a substrate crystal.

In the structural relaxations, there are often multiple metastable perovskite-based phases that are very close in energy, especially for misfit strains near a phase transition. The following strategies are employed to ensure the minimum energy perovskite-based phase is found. For each value of misfit strain, at least three of the structural optimizations described above are performed, and the lowest energy of these is taken. For each repetition, the atomic coordinates of the starting structure are randomly seeded with displacements of the atomic positions from the ideal strained perovskite structure having magnitudes up to 0.015 Å for each cartesian component of each atom position. These displacements generally remove all symmetry for each initial structure, making the space group $P1$. After an initial pass, inspection of the energy curve as a function of strain can still reveal discontinuities where calculations must be re-run. This process of searching for the true ground state at each misfit strain is continued until the energy curve and polarization properties are smooth functions of misfit strain away from first-order phase transitions. For more discussion of the calculation

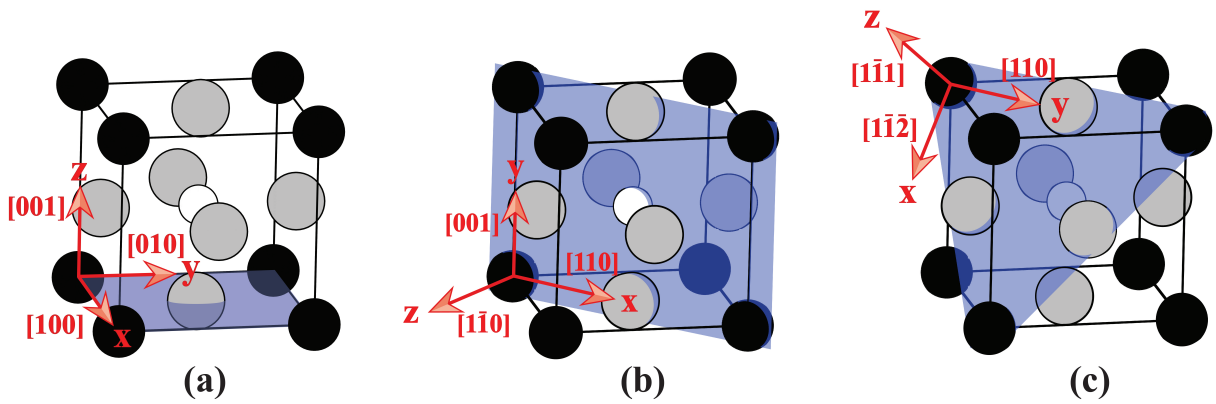

Figure 3.2: Orientations of measurement axes for the a) (100)-, b) (110)-, and c) (111)-growth orientations. Cubic crystallographic directions are indicated in square brackets. This figure was created using VESTA [55].

procedure and the details that enable it to be highly automated, see Section A.1 of the appendix.

3.2.3 Calculation Methods

All DFT calculations make use of the Vienna *ab initio* simulation package (VASP) [60–63] version 5.4.1. A conjugate-gradient algorithm is used to relax ionic positions to their ground state. As the standard VASP software package does not allow for arbitrary constraints to be placed on the strain tensor during relaxation, custom modification of the code was required. These modifications set certain components of the stress gradient tensor to zero during conjugate-gradient minimization, allowing for the mechanical boundary constraints (see above) of the three different growth orientations to be simulated.

All calculations use the Ceperley-Alder form of the local density approximation (LDA) exchange-correlation functional as parameterized by Perdew and Zunger [64], and the electron-ion interaction is described using the projector augmented wave method [65,66]. In multiple cases, metastable phases are only a fraction of an meV higher in energy compared to the lowest energy phase. Consequently, highly-converged calculation parameters are required. A 900 eV plane-wave cutoff energy, 6x6x6 Monkhorst-Pack sampling of the Brillouin zone [67], and tetrahedron method with Blöchl corrections [68] are used. The Berry phase approach, as described in the modern theory of polarization [24], is used to calculate the electric polarization vector at each misfit strain. All calculations assume a fixed (vanishing) external electric field corresponding to thin-films surrounded by perfectly charge-compensating electrodes. The relevance of this "short-circuit" boundary condition to thin-film growth is discussed in Refs. [69,70].

It should be noted that use of the LDA in the present work leads to well-known errors in the calculated lattice constants, which amount to an underestimation of their values on

Table 3.1: Listing of the 14 compositions considered, along with their cubic lattice constants and Goldschmidt tolerance factors.

Formula	a_0 (Å)	Tolerance Factor t
$BaHfO_3$	4.13	1.007
$BaSnO_3$	4.10	1.016
$BaTiO_3$	3.95	1.063
$BaZrO_3$	4.16	1.000
$KNbO_3$	3.96	1.090
$KTaO_3$	3.96	1.085
$NaNbO_3$	3.91	0.972
$NaTaO_3$	3.92	0.968
$NaVO_3$	3.68	1.028
$PbSnO_3$	4.04	0.955
$PbTiO_3$	3.89	0.999
$SrHfO_3$	4.07	0.949
$SrSnO_3$	4.03	0.957
$SrTiO_3$	3.86	1.001

the order of a percent. Previous calculations for perovskite oxide compounds have shown that these errors tend to be systematic across a broad range of chemistries [4, 10], and that quantitative values predicted by the LDA are generally in better agreement with experiment relative to those obtained by the generalized gradient approximation [21]. The LDA errors are mentioned explicitly below in those cases where they are relevant in the presentation of the results.

3.3 Results and Discussion

Table 3.1 lists the chemical formulas, calculated cubic reference lattice constants, and tolerance factors of the 14 compositions considered. The measurement axes used for reporting direction-dependent properties are different for each of the three growth orientations, as illustrated in Fig. 3.2.

Figure 3.3 shows, for all compositions and growth orientations considered, the calculated in-plane ($\sqrt{P_x^2 + P_y^2}$) and out-of-plane ($|P_z|$) polarizations of the thin-film systems plotted against the lattice constant of a corresponding cubic substrate. The x-axis has been curtailed to the experimentally relevant range of available in-plane lattice constants, and calculated

data may extend beyond this range for some systems. It should be noted that the epitaxial lattice constants presented in the horizontal axis of Fig. 3.3, as well as in Figs. 3.4–3.6 below, correspond to misfit-strain values based on the LDA calculations, and are thus expected to be on the order of a percent smaller than true experimental values.

The results plotted in Fig. 3.3 display several trends, which can be analyzed in relation to previously published observations. For a smaller set of (100)-oriented perovskite oxide compounds, previous works [4, 12] have demonstrated trends of out-of-plane and in-plane polarization enhancement under compressive and tensile misfit strain, respectively. The top two plots in Fig. 3.3 reveal the generality of these two trends across the wider compositional range considered in this work; all (100)-oriented systems show increasing out-of-plane polarization under compression (moving to smaller in-plane lattice parameters) and increasing in-plane polarization under tension (moving to larger in-plane lattice parameters). Interestingly, the trend of in-plane polarization enhancement under tension applies rather generally to all orientations (top-, middle- and bottom-left plots). The out-of-plane polarization for (110)-oriented systems (middle-right) is largely enhanced by compression, but less so than for the (100)-oriented systems. The out-of-plane polarization for the (111)-oriented systems shows a variety of behaviors, in addition to enhancement with compression. In the case of only one system, $BaTiO_3$, there is a significantly diminishing out-of-plane polarization with increasing biaxial compression. Many other (111)-oriented systems have large regions of nearly unchanging out-of-plane polarization.

Previous calculations have shown, for bulk ferroelectric perovskites, that c-axis elongation stabilizes polar distortions with atomic displacements in the out-of-plane direction [71]. The above-discussed polarization trends with misfit strain imply that polar distortions can be described in terms of a simple Poisson effect. That is, distortions tend to occur in the general direction of tension, whether it be out of plane or in plane, while distortions tend to be suppressed in compressed directions. In-plane misfit compression causes lattice expansion out of the plane, generally stabilizing out-of-plane polar displacements. Conversely, in-plane misfit tension causes a contraction of the lattice in the out-of-plane direction, disfavoring out-of-plane displacements and stabilizing in-plane polar distortions. Interestingly, this effect occurs irrespective of orientation of the applied misfit strain, as shown by the generality of the trend for the (110) and (111) orientations. Furthermore, the anomalously diminishing out-of-plane polarization witnessed in (111)-oriented $BaTiO_3$ correlates with this system's relatively small out-of-plane lattice elongation when subjected to in-plane compression. This case is discussed in more detail in Section 3.3.3.

Another trend apparent in Fig. 3.3 regards the nature of phase transitions between the various orientations. The (100)-oriented systems are largely characterized by smooth curves, featuring second-order transitions between the different phases with changing misfit strain. By contrast, the (110)- and (111)-oriented variants more commonly show first-order transitions, characterized by discontinuities in the polarization (and associated atomic displacements) with changing misfit strain. As sudden switches between polarization states are often intriguing for device applications (*e.g.*, ferroelectric random access memories [4]), film orientation could be a means by which this beneficial behavior is promoted.

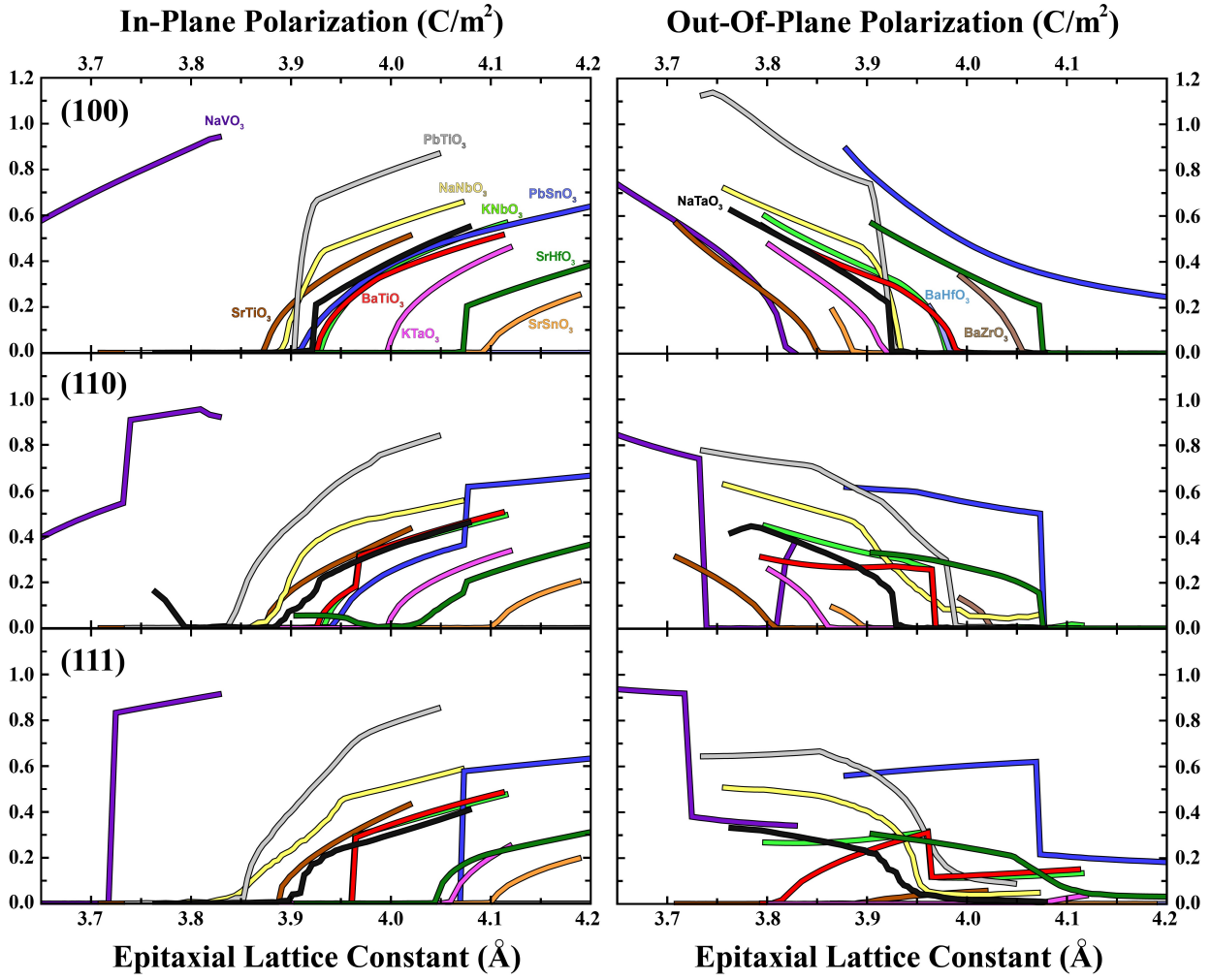

Figure 3.3: In-plane (left column) and out-of-plane (right column) polarization magnitudes versus cubic substrate lattice constant for the (100)- (top row), (110)- (middle row), and (111)- (bottom row) oriented systems. The same colors correspond to the same compositions for all six panels.

Analysis of the full data set produced in this work leads to clear relations between the energetic and polarization properties of various compositions. For a given orientation, there exists a small number of distinct energetic and polarization behaviors by which compositions can be categorized. In fact, each of the 14 compositions can be associated with one of four distinct behavioral groups, and, across different orientations, these groups tend not to change. For example, for the (100)-oriented systems, $BaTiO_3$, $KNbO_3$, $PbSnO_3$, and $NaVO_3$ show similar phase transition behavior and polarization curves. These four compositions furthermore show similar behavior relative to each other under the (110) and (111) orientations, even though the general behavior of this group is significantly different between these three orientations. The organization of these behavioral groups can be clearly visualized in Figs. A.1–A.3 in the appendix, and an in-depth analysis of these groups is given in Section 3.3.4.

The remainder of this section is divided into three subsections corresponding to highlighted results for the (100)-, (110)-, and (111)-oriented systems. Only a subset of the data produced in this work is presented in these sections, and, for analogous plots for all of the calculated data, the reader is referred to Figs. A.4–A.10 in the appendix. In each subsection, a subset of four representative systems for each orientation is discussed in detail in order to demonstrate the variety of phases and phase-transition behaviors that are observed in the full data set. These four systems are most representative of the four different behavior groups described above.

3.3.1 (100)-Oriented Systems

Table 3.2 summarizes the different (100)-oriented phases predicted along with their space group symmetries and a description of the polarization and homogeneous strain state (relative to a cubic reference structure). The (100)-oriented phases predicted in this work are consistent with those found previously in related phenomenological and first-principles computational studies [10, 11, 72].

Figure 3.4 presents representative results illustrating the calculated misfit strain dependence of the energy and polarization for four different compositions. For each, the energy versus misfit strain is plotted in the upper panel, and the values for the magnitude (dashed line) and out-of-plane (blue diamonds) and in-plane (green triangles and red squares) components of the polarization are plotted in the bottom panel. The horizontal scale on the top of each figure gives the corresponding lattice constant a of a cubic substrate required to produce the given value of misfit: $a = a_0(\bar{\eta} + 1)$, in terms of the reference lattice constant for the given compound a_0. Energies, unless noted otherwise, are referenced to the value corresponding to the equilibrium (likely non-cubic) bulk perovskite-based structure for the given composition, and their values can thus be interpreted as representing the strain energy of the epitaxially constrained phase. The more positive the energy, the higher the driving force for strain relaxation, *e.g.*, through formation of misfit dislocations. In the top panel, the space groups for the epitaxial phase with the lowest energy are indicated, and the dashed vertical lines indicate values of the misfit strain corresponding to phase transitions.

Table 3.2: Summary of the observed (100) epitaxial phases, including the commonly used phase name, space group, polarization vector, and Voigt-notated strain tensor. Strains are relative to a cubic $Pm\bar{3}m$ reference structure. p_i and s_i are arbitrary non-zero constants, while $\bar{\eta}$ is the misfit strain. The polarization vector and strain tensor components correspond to the coordinate system shown in Fig. 3.2a.

Phase	Space Group	(P_x, P_y, P_z)	$(\epsilon_{xx}, \epsilon_{yy}, \epsilon_{zz}, \epsilon_{yz}, \epsilon_{xz}, \epsilon_{xy})$
p	P4/mmm (123)	$(0, 0, 0)$	$(\bar{\eta}, \bar{\eta}, s_1, 0, 0, 0)$
c	P4mm (99)	$(0, 0, p_1)$	$(\bar{\eta}, \bar{\eta}, s_1, 0, 0, 0)$
aa	Amm2 (38)	$(p_1, p_1, 0)$	$(\bar{\eta}, \bar{\eta}, s_1, 0, 0, 0)$
a	Pmm2 (25)	$(p_1, 0, 0)$	$(\bar{\eta}, \bar{\eta}, s_1, 0, 0, 0)$
ac	Pm (6)	$(p_1, 0, p_2)$	$(\bar{\eta}, \bar{\eta}, s_1, s_2, 0, 0)$
r	Cm (8)	(p_1, p_1, p_2)	$(\bar{\eta}, \bar{\eta}, s_1, s_2, s_2, 0)$

Figure 3.4a presents calculated results for $BaTiO_3$, where the reference bulk structure for the energy calculations is a rhombohedral phase with space group $R3m$, and a=3.96 Å and α=89.93^o. Since this energetic reference structure is not cubic, while the structure used to define the reference for misfit strain is, the epitaxial strain with the lowest energy does not occur at $\bar{\eta}$=0 in Fig. 4a, but rather at a slightly positive value of $\bar{\eta}$=0.3%. Starting from the highest compressive strains and increasing $\bar{\eta}$ to more tensile values, Fig. 4a shows that the predicted sequence of phases for $BaTiO_3$ is $c - r - aa$ (corresponding to space groups of $P4mm$, Cm, and $Amm2$, respectively, as indicated in Table 3.2). This result is consistent with previous first-principles computed results [10,11]. The predicted misfit strain at which the c-r transition occurs is very close to that of Ref. [11], but the r-aa phase transition is predicted in this work to be at around 1% strain, whereas Ref. [11] predicts this transition to occur at just under 0.7%. This difference is likely attributable to minor variations in calculation parameters, as the energies of the r and aa phases are calculated, in the present work, to be within 0.1 meV/f.u. of each other at 0.7% misfit strain.

The calculated polarizations plotted in the lower panel show the onset of an in-plane polarization at the $c - r$ transition, which grows in magnitude with increasing values of $\bar{\eta}$. The out-of-plane polarization decreases in magnitude with increasing tensile misfit strain, vanishing for values of $\bar{\eta}$ beyond the $r-aa$ transition. Three other systems, including $KNbO_3$, $PbSnO_3$, and $NaVO_3$, have phase sequences and qualitative polarization dependences on misfit strain that are very similar to that shown in Fig. 3.4a for $BaTiO_3$. $KNbO_3$ (Fig. A.6 in the appendix) is the most similar to $BaTiO_3$, having the same phase sequence and nearly the same transition misfit strains, but with a slightly higher average polarization magnitude. $PbSnO_3$ (Fig. A.8) and $NaVO_3$ (Fig. A.8) also have the same qualitative polarization

behavior, but with much broader r (Cm) phase regions. For $PbSnO_3$, this r phase region is so broad that the Amm2 phase does not appear in the strain range considered, with the out-of-plane polarization remaining non-zero under the largest tensile strain considered, 4%. Likewise, for $NaVO_3$, the P4mm phase never appears in the range considered, with in-plane polarization remaining non-zero throughout. Such extended r phase regions and gradual phase transitions have not been predicted for (100)-oriented systems in previous studies [10, 11, 13, 15]. Finally, compared to $BaTiO_3$, $PbSnO_3$ and $NaVO_3$ have average polarization magnitudes more than twice as large, around 1 C/m^2 in the case of $NaVO_3$.

Figure 3.4b illustrates a second type of phase behavior observed in the calculations, represented by the specific case of $SrTiO_3$. At zero misfit strain, $SrTiO_3$ is predicted to assume the paraelectric p (P4/mmm) phase. Under sufficient compression ($< -0.4\%$), a non-zero out-of-plane polarization develops and the c (P4mm) phase is predicted. Under $> 0.3\%$ misfit tension, a non-zero in-plane polarization with equal x and y components appears, corresponding to the aa (Amm2) phase. The predicted phase order and polarization magnitudes are consistent with Ref. [13], although the paraelectric region in the present work is narrower by about 0.5% misfit strain (again, this discrepancy is likely due to differences in calculation parameters). Five other systems exhibit qualitative behavior similar to that illustrated in Fig. 3.4b for $SrTiO_3$, including $KTaO_3$ (Fig. A.6), $BaZrO_3$ (Fig. A.5), $SrSnO_3$ (Fig. A.10), $BaHfO_3$ (Fig. A.4), and $BaSnO_3$ (Fig. A.4). These systems all have in common a paraelectric p phase region of varying width around 0% misfit strain surrounded by a c phase region to the left and a phase with all in-plane polarization on the right (aa or a). In some cases the paraelectric phase region is very large, and for $BaSnO_3$, it extends across the entire range considered.

In previous studies of (100)-epitaxially strained systems [10,11,13,15], the phase sequences observed follow the pattern of c - (r, p, or phase separation) - (a or aa) with smooth, second-order transitions between different phases. With the expanded compositions treated in this work, an additional behavior is predicted having a direct transition from out-of-plane to in-plane polarization. Figure 3.4c illustrates this behavior for the specific case of $SrHfO_3$. For this system, there is a direct transition from c (P4mm) to a (Pmm2) at 0.2% misfit strain. To the limit of the resolution of this work's calculations, a direct transition between these two phases occurs without the region of intervening r (Cm) phase found for $BaTiO_3$ and related systems. The other system demonstrating this behavior is $NaTaO_3$ (Fig. A.7), which has a c (P4mm) to aa (Amm2) transition at just above 0% strain. This type of behavior is intriguing from the standpoint of the design of a memory device, since the calculations predict that, at around zero misfit strain, the application of a modest in-plane electric field could bias the c phase to transition to a metastable a or aa phase, leading to an extinction of the out-of-plane component of the polarization.

Figure 3.4d shows the polarization and energetic behavior of $PbTiO_3$. Like $BaTiO_3$, the phase sequence is predicted to follow the sequence of c-r-aa with increasing tensile strain. However, due to the presence of a region of strain with concave curvature in the energy, there is a finite range of $\bar{\eta}$ values for which the lowest-energy state is a two-phase mixture of phases having lower and higher values of misfit strain. This strain-induced phase coexistence

is similar to phase segregation in alloys of immiscible components, but with strain playing the analogue of composition [73]. A visual indicator of this behavior is the existence of a common tangent line that falls below the total energy curve. In the case of $PbTiO_3$, the monodomain r-phase is higher in energy than a mixture of c and aa phases between misfit strains of -0.3 and 1.7%, as indicated by the red dashed line in Fig. 3.4d. This phase-separation behavior for epitaxially strained $PbTiO_3$ has also been predicted in Ref. [10].

Other (100)-oriented systems predicted to exhibit strain-induced phase separation behavior are $NaNbO_3$ and $NaVO_3$. $NaNbO_3$ has a similar phase ordering to $PbTiO_3$ but with a broader predicted range of strains corresponding to the two-phase state, and less pronounced energetic driving force for phase separation (Fig. A.7 in the appendix). $NaVO_3$ is predicted to have a mixture of the r and aa phases between 2% and 4% misfit strain (Fig. A.8). The upper bound of this region is verified by calculations extending beyond 4% strain (Fig. A.11). In a real system, these regions of phase coexistence could be narrower than predicted due to factors not accounted for in the present study, such as interface coherency [73].

Of the three systems predicted to display phase coexistence, $PbTiO_3$ is the only one for which there is a significant driving force for this effect to take place. This could be due to the unique bonding characteristics of this system. Previous electronic structure calculations have outlined the pronounced covalency between Pb and O due to the hybridization of the Pb $6s$ electronic states with the O $2p$ states [74]. This is contrasted with a system such as $BaTiO_3$, in which the A cation acts as a spherical, nearly completely ionized Ba^{2+} ion. The resulting effect for $PbTiO_3$ is a stronger energetic dependence on atomic displacements, larger ferroelectric distortions, and increased sensitivity of the energy to non-hydrostatic strains [74]. The effect of strain-induced phase coexistence in $PbTiO_3$ is potentially useful for device applications, as has been appreciated in recent experimental and computational work [6, 73].

Interestingly, the three systems displaying phase coexistence feature soft biaxial elastic responses (*i.e.*, increases in strain energy with increasing misfit strain magnitude) compared to the other (100)-oriented films, as can be appreciated from a comparison of the associated calculated energy curves. This could have important practical applications, as the lower strain energies, for a given misfit strain, should lead to larger values for the critical thickness for misfit-dislocation formation.

3.3.2 (110)-Oriented Systems

Table 3.3 summarizes the different (110)-oriented phases observed in the present calculations, along with their space group symmetries and a description of the polarization and homogeneous strain state (relative to a cubic reference structure). Unlike the situation for (100)-oriented films, the authors are unaware of a standard nomenclature for the different phases that can be derived from the perovskite structure for (110)- and (111)-oriented films, and, in what follows, these are referred to by their space group symbols.

Figure 3.5a plots the polarization and energy versus misfit strain for $BaTiO_3$ with the (110)-growth orientation. The polarization behavior for (110)-oriented $BaTiO_3$ is predicted

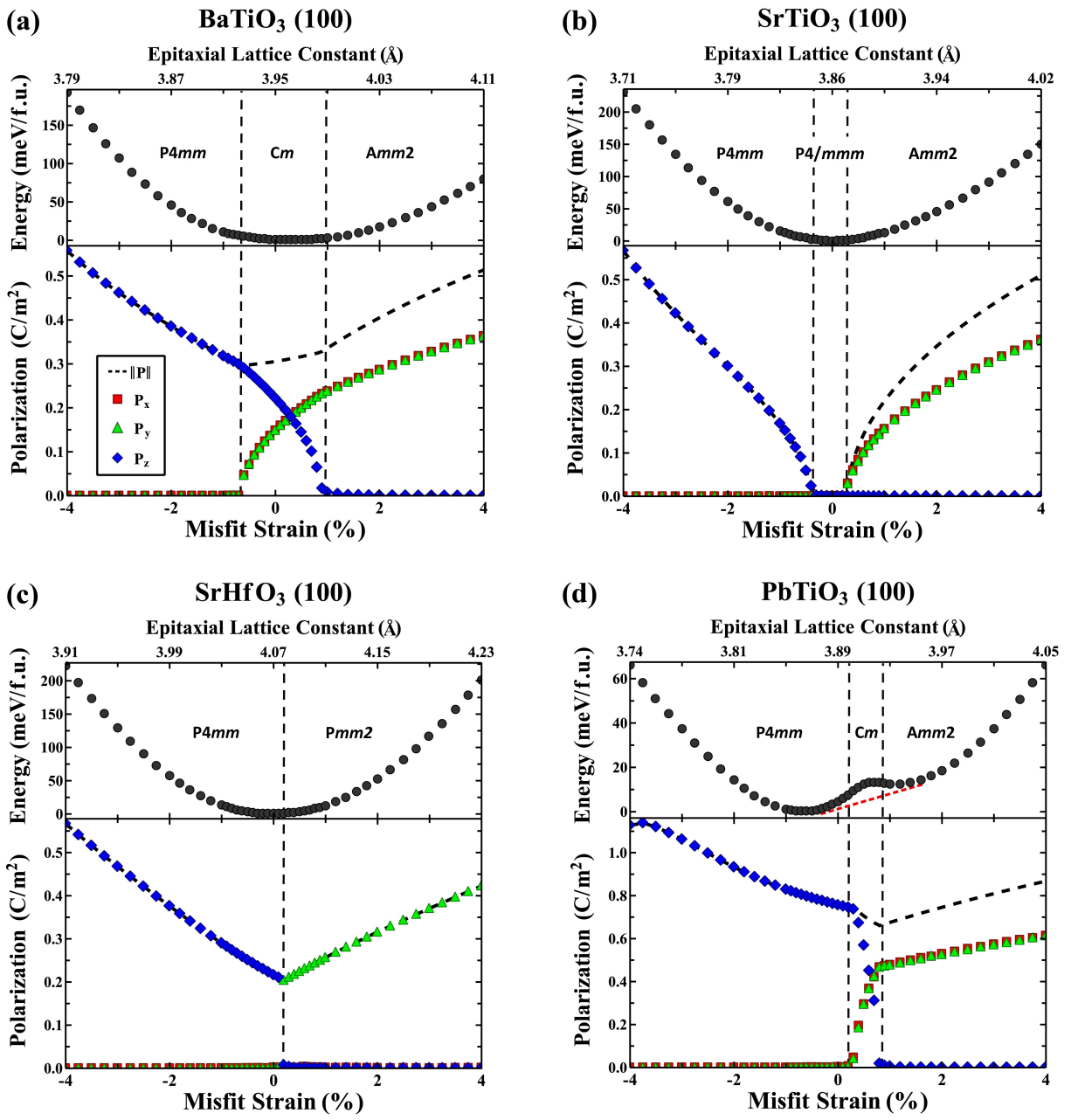

Figure 3.4: Energy and polarization as a function of misfit strain for a) $BaTiO_3$, b) $SrTiO_3$, c) $SrHfO_3$, and d) $PbTiO_3$ on (100). Energies are given in the top panel of each sub-figure and are referenced to the corresponding relaxed bulk perovskite-based structure. Regions of phase stability are labeled with the space group symbol and separated by vertical dashed lines. Absolute values of the polarization components have been taken for the purpose of visualization. Polarization vectors are relative to the axes given in Fig. 3.2a.

Table 3.3: Summary of the observed (110) epitaxial phases, including the space group, polarization vector, and strain tensor given in Voigt notation. Strains are relative to a cubic $Pm\bar{3}m$ reference structure. p_i and s_i are arbitrary non-zero constants, while $\bar{\eta}$ is misfit strain. The polarization vector and strain tensor components correspond to the coordinate system shown in Fig. 3.2b.

Space Group	(P_x, P_y, P_z)	$(\epsilon_{xx}, \epsilon_{yy}, \epsilon_{zz}, \epsilon_{yz}, \epsilon_{xz}, \epsilon_{xy})$
Cmmm (65)	$(0, 0, 0)$	$(\bar{\eta}, \bar{\eta}, s_1, 0, 0, 0)$
A$mm2$ (38)[1]	$(0, 0, p_1)$	$(\bar{\eta}, \bar{\eta}, s_1, 0, 0, 0)$
C$mm2$ (35)	$(0, p_1, 0)$	$(\bar{\eta}, \bar{\eta}, s_1, 0, 0, 0)$
Cm (8)	$(p_1, p_2, 0)$	$(\bar{\eta}, \bar{\eta}, s_1, 0, 0, 0)$
Cm^* (8)[2]	$(0, p_1, p_2)$	$(\bar{\eta}, \bar{\eta}, s_1, s_2, 0, 0)$
Pm (6)	$(p_1, 0, p_2)$	$(\bar{\eta}, \bar{\eta}, s_1, 0, s_2, 0)$
P1 (1)	(p_1, p_2, p_3)	$(\bar{\eta}, \bar{\eta}, s_1, s_2, s_3, 0)$

to be significantly different from the (100)-oriented case. Under large compression, a broad region of the A$mm2$ phase is observed, with a polarization that is oriented out of plane and nearly constant in magnitude versus strain. At small compressive strain, a non-zero P_y component develops and a transition to the Cm^* phase occurs. Finally, at around $\bar{\eta} = 0.4\%$, there is a sudden disappearance of out-of-plane polarization paired with a jump in P_x, signifying a first-order transition to a distinct Cm phase. (110)-oriented $BaTiO_3$ has been studied in Ref. [47], using a first-principles effective Hamiltonian approach with Monte Carlo simulations. The present work predicts the same order of phases versus strain as found in Ref. [47] at the lowest temperature considered (5 K), although the exact values of the strains where the phase transitions occur show slight differences, presumably because of the different computational approaches employed. Three other systems, $KNbO_3$ (Fig. A.6), $PbSnO_3$ (Fig. A.8), and $NaVO_3$ (Fig. A.8) have the same phase sequences and very similar qualitative behavior as $BaTiO_3$. In the case of $NaVO_3$, a P1 phase appears at very large tensile misfit strains, with the out-of-plane polarization re-emerging. $NaVO_3$ furthermore has the largest average polarization at nearly 1 C/m^2.

Figure 3.5b gives the polarization and energy dependence on misfit strain for $SrTiO_3$ with the (110)-growth orientation. The qualitative polarization behavior is similar to that for the (100)-oriented case, with a paraelectric region (Cmmm phase) surrounded by phases with out-of-plane polarization under compression (A$mm2$) and in-plane polarization under tension (C$mm2$ - Cm). However, the width of this paraelectric region is larger for (110)-oriented $SrTiO_3$ and is shifted toward the compressive regime compared to the (100)-oriented case. Once again, five other systems exhibit qualitative behavior similar to that illustrated in Fig. 3.5b for $SrTiO_3$, including $KTaO_3$ (Fig. A.6), $BaZrO_3$ (Fig. A.5), $SrSnO_3$ (Fig.

A.10), $BaHfO_3$ (Fig. A.4), and $BaSnO_3$ (Fig. A.4). In the (110)-oriented case, both $BaSnO_3$ and $BaHfO_3$ have paraelectric Cmmm phase regions that extend across the entire range considered.

Figure 3.5c shows the polarization and energetic behavior of $SrHfO_3$ with the (110)-growth orientation. The general behavior is similar to (100)-oriented $SrHfO_3$ shown in Fig. 3.4c, both having a first-order transition at 0.2% misfit strain that takes the system from primarily out-of-plane polarization to primarily in-plane polarization. For (110)-oriented $SrHfO_3$, the predicted phase sequence is Pm, with non-zero P_x and P_z polarization components, to Amm2, with exclusively non-zero P_z, back to Pm, and finally to Cmm2, with exclusively non-zero P_y. $NaTaO_3$ (Fig. A.7) has a very similar polarization behavior, with slightly higher polarization magnitudes and an additional intermediate P1 phase.

Figure 3.5d shows the polarization and energetic behavior of $PbTiO_3$ with the (110)-growth orientation. A comparison of the results with those for the (100) orientation in Fig. 3.4d, illustrates the pronounced effect that film orientation can have on the polarization and energetic behavior. Unlike (100)-oriented $PbTiO_3$, strain-induced phase separation is not predicted in any strain regime for the (110) orientation. Instead, four phases appear in roughly evenly spaced strain regimes, with a phase ordering of Amm2 - Pm - P1 - Cmm2. The P1 to Cmm2 phase transition is first order, with a sudden drop in P_x and P_z, which is replaced by the appearance of a P_y component. Furthermore, the average total polarization magnitude is slightly diminished and much more consistent with changing strain as compared to the (100)-oriented case. Overall, the polarization behavior is much more nuanced for the (110) orientation, with all three components of the polarization growing or diminishing at various strain regimes. Finally, the effective strain energy versus misfit strain rises much more rapidly in the (110)-oriented case compared to the (100)-oriented structure. $NaNbO_3$ (Fig. A.7) shows similar polarization behavior to that shown in 3.5d for $PbTiO_3$, having an Amm2 - Pm - P1 phase sequence. The first-order transition from P1 to Cmm2 seen for $PbTiO_3$ is, in this case, replaced by an extended P1 phase region with smoothly increasing in-plane polarization and smoothly decreasing out-of-plane polarization. The total polarization magnitude in this region remains roughly constant at around 0.5 C/m^2.

3.3.3 (111)-Oriented Systems

Table 3.4 summarizes the different (111) phases observed in the present calculations, along with their space group symmetries and a description of the polarization and homogeneous strain state (relative to a cubic reference structure). It is interesting to compare the observed phases with the list of all symmetry-allowed perovskite phases consistent with (111) epitaxy determined in Ref. [49] (see Table I of Ref. [49] for the list of phases and their symmetries). In the present calculations, only a subset of the possible symmetries listed in Ref. [49] are observed. Specifically, the non-polar phases with R32, and C2/m symmetry as well as the polar phase with the C2 symmetry are not observed as stable among the systems considered. In Ref. [49], it is argued that the lowest-symmetry P1 phase is unlikely to form in (111)-

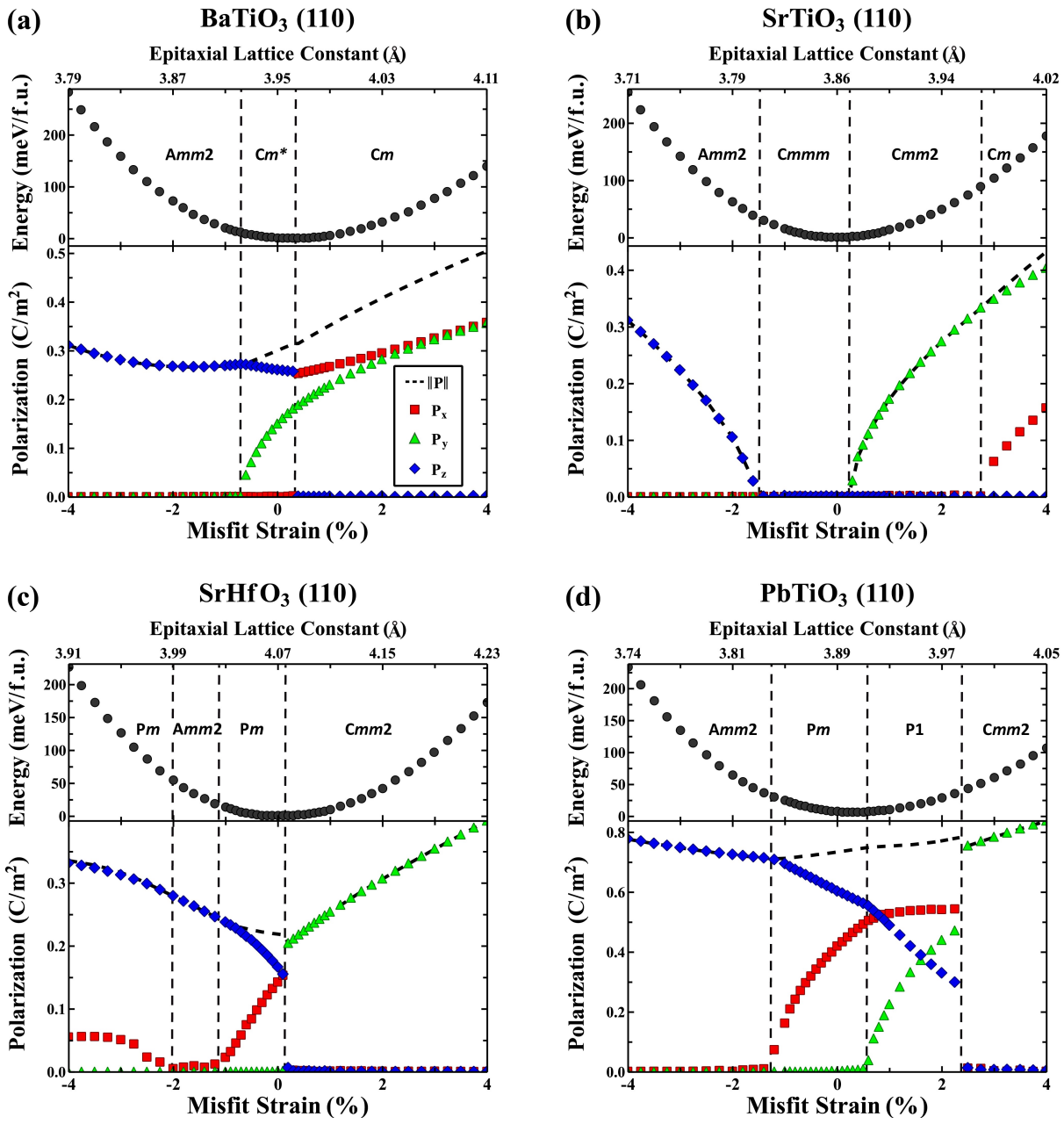

Figure 3.5: Energy and polarization as a function of misfit strain for a) $BaTiO_3$, b) $SrTiO_3$, c) $SrHfO_3$, and d) $PbTiO_3$ on (110). Energies are given in the top panel of each plot and are referenced to the corresponding relaxed bulk perovskite-based structure. Regions of phase stability are labeled with the space group symbol and separated by vertical dashed lines. Absolute values of the polarization components have been taken for the purpose of visualization. Polarization vectors are given relative to the axes given in Fig. 3.2b.

Table 3.4: Summary of the observed (111) epitaxial phases, including the space group, polarization vector, and strain tensor given in Voigt notation. Strains are relative to a cubic $Pm\bar{3}m$ reference structure. p_i and s_i are arbitrary non-zero constants, while $\bar{\eta}$ is misfit strain. The polarization vector and strain tensor components correspond to the coordinate system shown in Fig. 3.2c

Space Group	(P_x, P_y, P_z)	$(\epsilon_{xx}, \epsilon_{yy}, \epsilon_{zz}, \epsilon_{yz}, \epsilon_{xz}, \epsilon_{xy})$
R$\bar{3}m$ (166)	$(0, 0, 0)$	$(\bar{\eta}, \bar{\eta}, s_1, 0, 0, 0)$
R3 (146)	$(0, 0, p_1)$	$(\bar{\eta}, \bar{\eta}, s_1, 0, 0, 0)$
R3m (160)	$(0, 0, p_1)$	$(\bar{\eta}, \bar{\eta}, s_1, 0, 0, 0)$
Cm (8)	$(p_1, 0, p_2)$	$(\bar{\eta}, \bar{\eta}, s_1, 0, s_2, 0)$
Cm $(8)^3$	$(p_1, \sqrt{3}p_1, p_2)$	$(\bar{\eta}, \bar{\eta}, s_1, \sqrt{3}s_2, s_2, 0)$
P1 (1)	(p_1, p_2, p_3)	$(\bar{\eta}, \bar{\eta}, s_1, s_2, s_3, 0)$

oriented perovskite films, while this phase is observed in the present calculations for the $SrSnO_3$ and $SrTiO_3$ systems over small strain regimes.

Before turning to a discussion of the observed results for the (111) orientation, it is noted that the R3 phase in Table IV has a space group that is a subgroup of that for the R3m phase; these two phases share the same polarization direction, but additional atomic displacements in the former case break the mirror symmetry in the latter. Also, the two Cm phases listed in Table IV are energetically equivalent and differ only by an in-plane rotation of the cell by 60°. This difference is equivalent to an in-plane rotation of the measurement axes and is not physically significant.

Figure 3.6a plots the polarization and energy versus misfit strain for $BaTiO_3$ with the (111)-growth orientation. Under very large compressive misfit strains, the paraelectric R$\bar{3}m$ phase is predicted to be energetically stable. With decreasing compressive strain, this phase undergoes a second-order transition to the R3m phase with polarization directed normal to the epitaxial plane. At $\bar{\eta}$=0.2%, the R3m phase undergoes a first-order transition to the Cm phase with mixed P_x and P_z components. Most striking for this system is the anomalous out-of-plane polarization behavior, which is diminished under compression. This behavior has been predicted previously [48, 49], although the paraelectric regions in these works occur at smaller compressive strains. This difference in phase boundary position is again likely to be associated with the details of the calculation methods, due to the near energetic degeneracy of the paraelectric R$\bar{3}m$ phase with the R3m phase for less than -1% compressive strains.

No other (111)-oriented systems considered in this work show this anomalous out-of-plane polarization decrease with increasing compressive strains to any significant extent. $KNbO_3$ (Fig. A.6), $PbSnO_3$ (Fig. A.8), and $NaVO_3$ (Fig. 3.6c) have similar first-order R3m to Cm transitions under tension, but due to the lack of diminishing P_z under compression, these

three systems, which have been grouped with $BaTiO_3$ in the (100)- and (110)-oriented cases, are separately discussed below with $NaVO_3$ as the representative system (Fig. 3.6c). The unique behavior of $BaTiO_3$ can be explained in terms of elastic arguments. At -4% misfit strain, the out-of-plane tensile strains of $BaTiO_3$, $KNbO_3$, $PbSnO_3$, and $NaVO_3$ are 2.5%, 3.8%, 5.0%, and 6.2%, respectively, showing that $BaTiO_3$ has a significantly smaller out-of-plane strain than the other three systems. This relatively small Poisson ratio for $BaTiO_3$ is not present in the (100)- and (110)-growth orientations. It is suggested in Ref. [48] that the anomalous paraelectric transition of $BaTiO_3$ is the result of compression forcing the oxygen spacing to contract the hollow space above and below the Ti cation, pushing this atom back to its central position. This description, however, does not generalize to the other three similar systems in this work, because they are able to significantly expand in the out-of-plane direction, thereby creating space for the B-cation to remain off-center.

Figure 3.6b shows the polarization and energetic behavior of $SrTiO_3$ with the (111)-growth orientation. From large compressive until modest tensile strain, the R$\bar{3}m$ paraelectric phase is stable. From 0.7% to 1.2% misfit strain, a small region of P1 phase is stable, followed by a transition to Cm. Both of these $SrTiO_3$ polar phases have predominantly in-plane polarization. As was the case for the (100) and (110) orientations, five other systems exhibit qualitative behavior similar to that illustrated in Fig. 3.6b for $SrTiO_3$, including $KTaO_3$ (Fig. A.6), $BaZrO_3$ (Fig. A.5), $SrSnO_3$ (Fig. A.10), $BaHfO_3$ (Fig. A.4), and $BaSnO_3$ (Fig. A.4). In the (111)-oriented case, $BaSnO_3$, $BaZrO_3$, and $BaHfO_3$ all have paraelectric R$\bar{3}m$ phase regions that extend across the entire misfit strain range considered. This polarization behavior group is similar to the paraelectric group in the (100)- and (110)-oriented cases, except with the absence of a phase with predominantly out-of-plane polarization, even under very large compression.

Figure 3.6c shows the polarization and energetic behavior of $NaVO_3$ with the (111)-growth orientation. This system has a very large and consistent polarization magnitude of around 1 C/m^2 in all strain regimes. Under compression, the R3m phase with large out-of-plane polarization is predicted, while the Cm phase with mixed polarization contributions is predicted under tension. A first-order phase transition between R3m and Cm occurs at just over 1% misfit strain (3.71 Å) and coincides with the point of lowest predicted elastic energy. Given the relative stability and large, sudden change in polarization at this point, moderately tensile-strained $NaVO_3$ could provide interesting properties for device applications. Furthermore, the region of stability is predicted to be broad, showing less than 25 meV metastability relative to the fully-relaxed bulk phase throughout -1% to 3% misfit strain (3.64-3.79 Å). This stability is, in part, due to the pronounced asymmetry of the energy curve. For $NaVO_3$, the maximum metastability under 4% compression is over 250 meV, while the maximum under 4% tension is only 50 meV. Two other systems, $KNbO_3$ (Fig. A.6) and $PbSnO_3$ (Fig. A.8), fall into the same polarization behavior group as $NaVO_3$, both having smaller average polarization magnitudes. Note that the Cm phases are the same for these three systems, as discussed above. These three systems follow the same phase transition sequence as $BaTiO_3$ (Fig. 3.6a), but have been separately grouped due to their nearly constant (and non-vanishing) out-of-plane polarizations under compression.

Figure 3.6d gives the polarization and energy dependence on misfit strain for $PbTiO_3$ with the (111)-growth orientation. Compared to the (100)- (Fig. 3.4d) and (110)-oriented (Fig. 3.5d) cases, (111)-oriented $PbTiO_3$ shows very broad phase regions connected by smooth, second-order transitions and a slightly diminished average polarization magnitude. This system exhibits a single second-order phase transition between an R3m phase having all out-of-plane polarization, and a Cm phase having an additional in-plane polarization component. With increasing tension in the Cm phase, the out-of-plane polarization gradually gives way to predominantly in-plane polarization. As for the (100)- and (110)-oriented cases, $NaNbO_3$ (Fig. A.7) shows polarization behavior very similar to $PbTiO_3$ for the (111)-growth orientation. Two additional systems, $SrHfO_3$ (Fig. A.9) and $NaTaO_3$ (Fig. A.7), display the same qualitative behavior. $NaNbO_3$, $SrHfO_3$, and $NaTaO_3$ have additional R3 - R3m phase transitions under large compression, which have no effect on the polarization direction (see R3 symmetry discussion above). It is interesting to note that, $SrHfO_3$ (Fig. A.9) and $NaTaO_3$ (Fig. A.7), comprising a distinct polarization behavior group in the (100)- and (110)-oriented cases, show behavior similar to $PbTiO_3$ and $NaNbO_3$ under the (111)-growth orientation.

3.3.4 Analysis of Polarization Behaviors

There exists a small number of distinct energetic and polarization behaviors by which compositions considered in this work can be categorized. Six of the 14 systems considered exhibit non-polar phases over significant ranges of misfit strain. Another four systems, $BaTiO_3$, $KNbO_3$, $PbSnO_3$, and $NaVO_3$ have very similar phase orderings and polarization behaviors in all three orientations. The remaining four systems, $SrHfO_3$, $NaTaO_3$, $PbTiO_3$, and $NaNbO_3$ only loosely group together, having a more diverse set of behaviors and less consistency in their internal groupings across the three orientations. These behavioral groups can be visualized in Figs. A.1-A.3 in the appendix.

These groupings can be partially explained from geometric considerations. From this perspective, a polar distortion develops to optimize bond lengths, as determined by ionic radii. The Goldschmidt tolerance factor (t) characterizes the propensity of a given perovskite chemistry to distort. Values near unity favor cubic, non-polar structures, while values far from unity favor distortions. Given the five-atom restriction of the model presented in this work, these distortions must always be polar. The six compositions (tolerance factors) for the behavior group having large non-polar phase regions are $SrTiO_3$ (t = 1.001), $KTaO_3$ (1.085), $BaZrO_3$ (1.000), $SrSnO_3$ (0.957), $BaHfO_3$ (1.007), and $BaSnO_3$ (1.016). Four of the six systems have tolerance factors very near unity. However, it is unusual that $KTaO_3$ and $SrSnO_3$ should maintain any regions of paraelectricity given the ratios of their ionic radii. Furthermore, it is unclear why $BaSnO_3$ does not undergo a polar distortion under any amount of misfit strain given that its tolerance factor deviates from unity by a non-negligible amount. The four compositions (tolerance factors) composing the second behavior group are $BaTiO_3$ (t = 1.063), $KNbO_3$ (1.090), $PbSnO_3$ (0.955), and $NaVO_3$ (1.028). Three of the four systems have B cations that are relatively too small in the cubic perovskite structure, while

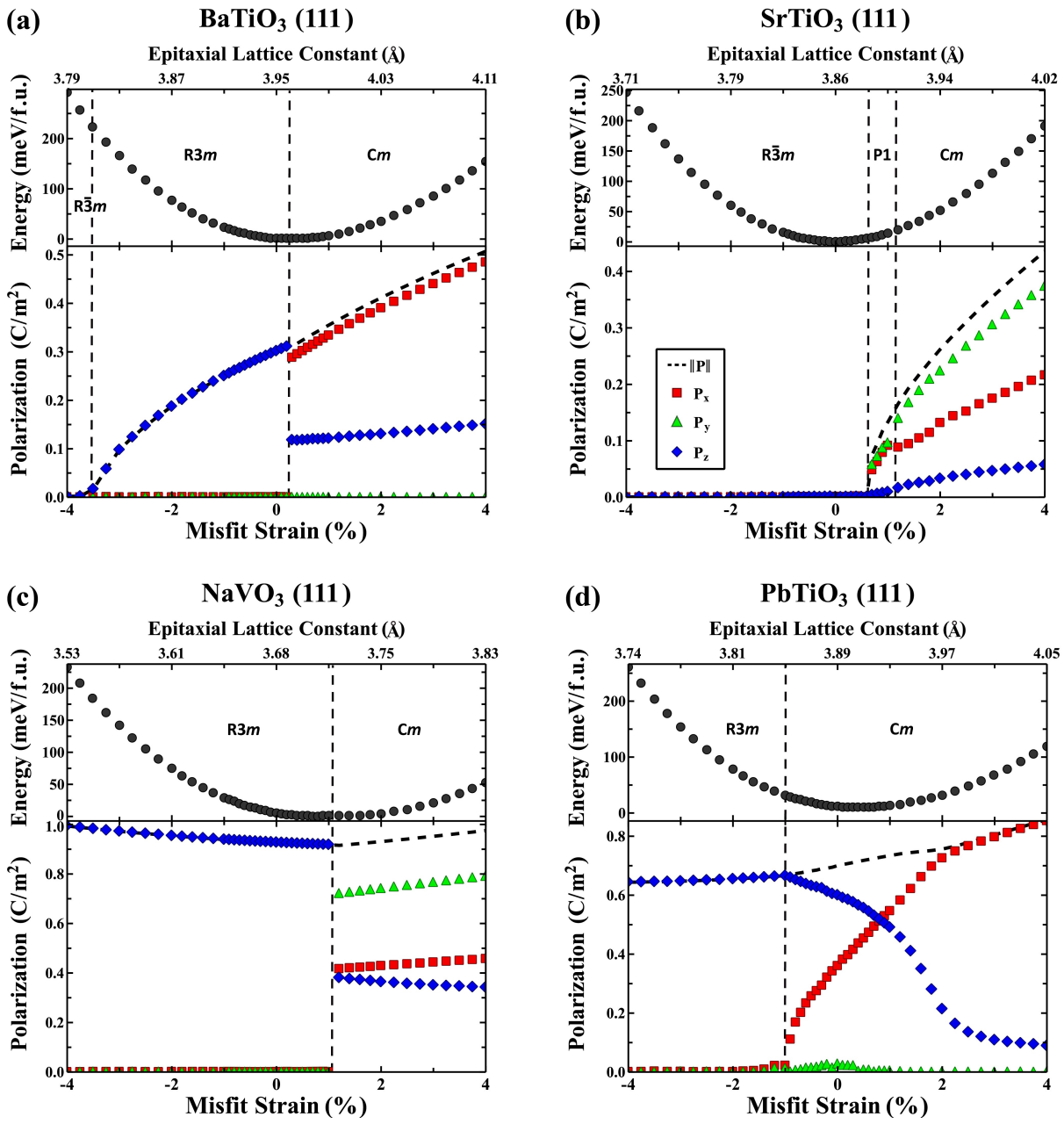

Figure 3.6: Energy and polarization as a function of misfit strain for a) $BaTiO_3$, b) $SrTiO_3$, c) $NaVO_3$, and d) $PbTiO_3$ on (111). Energies are given in the top panel of each plot and are referenced to the corresponding relaxed bulk perovskite-based structure. Regions of phase stability are labeled with the space group symbol and separated by vertical dashed lines. Absolute values of the polarization components have been taken for the purpose of visualization. Polarization vectors are relative to the axes given in Fig. 3.2c.

$PbSnO_3$ is seemingly anomalous, having an A cation that is too large and is thus expected to have differing polarization behavior from the other three. The final group of compositions (tolerance factors) are $SrHfO_3$ ($t = 0.949$) $NaTaO_3$ (0.968), $PbTiO_3$ (0.999), and $NaNbO_3$ (0.972). The seemingly anomalous system in this case is $PbTiO_3$, which, based on ionic radii, should group with the six non-polar compositions. To reconcile the exceptional systems, we consider additional features of the bonding.

From an electronic standpoint, ferroelectricity is not favored in a perovskite system that features purely ionic bonding. Rather, polar distortions are understood to be stabilized by the development of covalent character in the bonding of one or more cations with oxygen [75]. Two ways in which this mixed ionic-covalent bonding appears are through lone-pair s electronic states on the A cation (*e.g.*, Pb^{2+}) as well as energetically low-lying empty d orbitals on the B cation (*e.g.*, Ti^{4+}, Nb^{5+}). In both cases, these electronic states hybridize with occupied oxygen $2p$ orbitals to stabilize a polar distortion [76]. These considerations help explain some of the anomalies described above. For example, $SrSnO_3$ and $BaSnO_3$ have A cations that lack lone-pair electrons and B cations that lack empty d orbitals. These two systems are expected to exhibit more ionic character in their bonding, which in turn could explain the tendency of these two systems to remain non-polar over a larger misfit strain regime than expected. Furthermore, $PbSnO_3$ has an A cation with lone-pair electrons but a B cation lacking empty d orbitals. Thus, for this system, the A cation is expected to feature enhanced covalent character in its bonding with oxygen, while the B cation will be primarily ionic. This is the reverse of the behavior of the other three systems sharing a behavior group with $PbSnO_3$. Under these circumstances, it is possible that a system with tolerance factor less than one can behave similarly to those with tolerance factors greater than one if the electronic character of the cation species is swapped. Finally, $PbTiO_3$ ($t = 0.999$), is highly susceptible to covalency, having both A and B cations capable of hybridizing with oxygen. This could possibly explain why a non-polar phase is never predicted, despite this system's geometric amenity to a non-polar structure. The qualitative considerations above serve to highlight the geometrical and bonding factors that underlie the main trends in the computed results. However, more work is required to develop quantitative theories for the strain dependencies of polarization. This is highlighted by the case of $KTaO_3$. Based on geometric and electronic considerations, this system should behave most similarly to systems in the $BaTiO_3$ group, but instead $KTaO_3$ exhibits a non-polar phase over a large range of misfit strain.

3.4 Summary

The effects of epitaxial misfit strain on the structure, polarization, and energetic behavior of 42 non-magnetic perovskite thin-film systems have been investigated using an automated first-principles computational approach. These 42 systems are comprised of 14 compositions modeled for the (100)-, (110)-, and (111)-growth orientations. The results indicate robust trends of in-plane polarization enhancement under tension for all growth orientations and

out-of-plane polarization enhancement with compression for the (100)- and (110)-oriented systems. For the (111)-growth orientation, a wider variety of out-of-plane polarization behaviors is seen, with $BaTiO_3$ exhibiting an anomalously diminishing out-of-plane polarization with compression.

The computational results further reveal a clear tendency for compounds with different compositions to form behavior groups, characterized by their phase sequences and polarizations versus misfit strain. Two (100)-oriented systems, $SrHfO_3$ and $NaTaO_3$, exhibit unique polarization dependencies on misfit strain, having phase transitions near 0% misfit strain whereby a phase with all out-of-plane polarization gives way to a phase with all in-plane polarization. The three (100)-oriented systems showing strain-induced phase coexistence, $PbTiO_3$, $NaNbO_3$, and $NaVO_3$, have relatively soft biaxial elastic responses compared to the other compounds where this phenomenon is absent. This suggests that softness of the in-plane biaxial elastic response is an important factor in predicting whether or not strain-induced phase coexistence will occur in a film.

This work demonstrates the profound effect of growth orientation on the polarization behavior of thin films. For example, the smooth, second-order phase transitions and strain-induced phase coexistence exhibited by (100)-oriented $PbTiO_3$ are replaced by a complex interplay of the three polarization components and a first-order transition in (110)-oriented $PbTiO_3$. While most of the other compounds show similar sensitivity to growth orientation, the six compositions, $SrTiO_3$, $KTaO_3$, $BaZrO_3$, $SrSnO_3$, $BaHfO_3$, and $BaSnO_3$, show similar paraelectric behavior between the (100), (110), and (111) orientations. Further, the (110)- and (111)-oriented films more commonly feature first-order phase transitions as a function of misfit strain, relative to the (100) case. An example is (111)-oriented $NaVO_3$, having a first-order phase transition at small misfit tension with a very large shift in polarization direction. As sudden changes in polarization state are often useful for device applications, the relatively unexplored realm of (110)- and (111)-oriented films could provide a fruitful domain for materials discovery.

CHAPTER 4

Epitaxial Phase Diagrams Including the Role of Antiferrodistortive and *A*-Site Displacement Modes

4.1 Motivation and Overview

Ferroelectric thin films based on perovskite-structured oxide compounds are widely researched for a variety of microelectronic device applications [1]. Thin-film forms of these ferroelectric materials are of interest due to their reduced dimensionality, as well as the novel properties that arise from epitaxial constraints [4]. In particular, epitaxial strain has been shown to have a strong effect on the polarization and domain behavior of ferroelectrics [31], and it thus provides a means of tuning properties for device applications.

To exploit such epitaxial effects, predictive first-principles computational models based on density-functional theory (DFT) have been developed and applied to predict the structure and polarization of oxide ferroelectrics as a function of biaxial strain. In such modeling efforts, a few different approaches have been employed. In early studies [9,10], expansions of the total energy with respect to the amplitudes of unstable phonon modes and strain were determined and used to compute stable structures and associated energetics and polarizations as a function of misfit strain. Although effective for prototypical perovskites like $BaTiO_3$, a limitation in the approach was the consideration of only zone-centered soft-phonon modes, and the associated neglect of octahedral rotations, which have been shown to suppress polarization in many perovskites [16]. In more recent studies that have considered a broader range of compositions [11–15,77], direct DFT relaxations of candidate perovskite-based structures were undertaken as a function of biaxial strain. In some of these studies, candidate structures were limited to those that could be derived only from distortions and zone-center displacements in the primitive five-atom unit cell, again neglecting structural distortions associated with octahedral rotations. In other first-principles computational studies, more complex structures have been considered, derived from experimental measurements [78,79]. These latter studies have accounted for important effects of non-zone-centered displacement

The work in this chapter was published by T. Angsten and M. Asta in Physical Review B **97**, 134103 (2018), and is reproduced here with permission of the co-author.

modes, such as antiferrodistortive (AFD) octahedral rotations or A-site displacement modes, but they have been limited to the relatively few compositions where experimentally measured crystallographic data for strained thin films are available.

In the present work, a methodology is presented extending previous efforts to account for non-zone-centered modes in the calculation of ground-state structures and associated polarizations in epitaxially-strained perovskite thin films. The approach makes use of direct DFT optimizations of candidate structures corresponding to local minima in expansions of the energy with respect to strain and the amplitudes of the nine most unstable phonon modes of reference high-symmetry perovskite structures. The expansions are carried out at several strain states, and the full set of structures corresponding to the minima identified in the energy expansions are used as input to DFT energy minimizations as a function of biaxial strain. From the lowest-energy structures identified, epitaxial phase diagrams and polarization plots similar to those presented in Ref. [11] are constructed, but accounting for more complex polymorphs that feature non-zone-centered displacement modes.

This approach is employed in the present work in a DFT-based study of the ground-state phase diagrams of epitaxially-strained $SrTiO_3$, $CaTiO_3$, and $SrHfO_3$ compounds. While $SrTiO_3$ and $CaTiO_3$ are more commonly studied perovskite oxides and thus serve as good reference compounds for comparisons to other methods, $SrHfO_3$ is a lesser-studied system in the context of thin films. $SrHfO_3$ was chosen due to its similarity to $CaTiO_3$ with respect to ratios of ionic radii, thus facilitating an analysis of the effect of composition on thin-film properties, but also because of its promising polar response properties. In Ref. [27], a metastable $P4mm$ phase of $SrHfO_3$ was selected out of a first-principles screening of nearly a thousand piezoelectric tensors due to its large piezoelectric response, having a maximal longitudinal modulus of $||e_{ij}||_{max} \approx 10$ C/m^2. It is thus worthwhile to determine in the present work whether this $P4mm$ $SrHfO_3$ phase can be epitaxially stabilized by measuring its degree of metastability, and also to see if this system retains a large polarization under epitaxy.

Ground-state structures and associated energetics and polarization properties are calculated for $SrTiO_3$, $CaTiO_3$, and $SrHfO_3$ as a function of epitaxial strain state, corresponding to biaxial tension and compression in the (001) plane. In the remainder of this chapter, the computational approach is described in detail in Section 4.2, and results obtained are presented in Section 4.3. Insights derived from these results, as they relate to the role of non-zone-centered phonons on the stability and polarization properties of epitaxially-strained perovskite thin films are discussed in Section 4.4, and the main conclusions are summarized in Section 4.5.

4.2 Method

In the present computational approach, epitaxial thin films are modeled as bulk compounds subjected to biaxial strain in the (001) plane, neglecting explicit surface and interface effects. In discussing crystallographic structures and strain states, we employ throughout a

coordinate system in which the x and y directions are along [100] and [010] directions of a reference tetragonal perovskite unit cell, and z is the direction normal to the plane of biaxial strain. In what follows, a description is given for the nature of the energy expansions used to identify candidate structures for DFT optimizations (Section 4.2.1), the way in which resulting optimized structures are used to construct epitaxial ground-state phase diagrams (Section 4.2.2), and the associated details of the DFT calculations (Section 3.2.3).

4.2.1 Total Energy Expansions

For each composition, the lattice constant of an ideal cubic perovskite structure (space group $Pm\bar{3}m$) is calculated. Tensile strains are then applied to the x and y directions by a misfit strain $\bar{\eta}$, considering values of -2, -1, 0, 1, and 2%. For each biaxial strain state, the out-of-plane (c-axis) lattice constant is relaxed, and 40-atom ($2 \times 2 \times 2$) supercells are then constructed from these structures to serve as reference states for subsequent expansions of the total energy.

The total energy expansions consider both homogeneous strain and atomic displacement degrees of freedom. Regarding strain, the mechanical boundary conditions for a coherently strained epitaxial thin film are defined as:

$$\epsilon_{xx} = \epsilon_{yy} = \bar{\eta}, \quad \epsilon_{xy} = 0; \sigma_{zz} = \sigma_{yz} = \sigma_{xz} = 0, \tag{4.1}$$

where ϵ and σ are the strain and stress tensors, respectively, and $\bar{\eta}$ is the misfit strain, calculated as $\bar{\eta} = a/a_0 - 1$, where a_0 is the lattice constant of the reference cubic perovskite (with zero misfit strain), and a corresponds to the lattice constant of a cubic substrate. At fixed misfit strain, ϵ_{zz}, ϵ_{xz}, and ϵ_{yz} constitute the three strain degrees of freedom. For the following total energy expansions, the two out-of-plane shear strains ϵ_{xz} and ϵ_{yz} are assumed to be relatively unimportant in dictating candidate energy minima in the potential-energy landscape, and only ϵ_{zz} is considered explicitly.

Regarding atomic positional degrees of freedom, the most basic approach is to include all x-, y-, and z-displacements of each atom in the reference structure. However, this leads to $(40 \times 3) - 3 = 117$ additional degrees of freedom and a prohibitive number of coefficients that must be evaluated. A more efficient technique is to choose a set of displacement variables that still forms a complete basis but can be prioritized by relative importance for the energy landscape. This is accomplished most simply by considering unstable and soft modes of the force-constant matrix [9].

The force-constant matrix, $D^{\tau,\tau'}_{\alpha,\beta}$, is defined as:

$$D^{\tau,\tau'}_{\alpha,\beta} = \left. \frac{\partial^2 E}{\partial \upsilon^{\tau}_{\alpha} \partial \upsilon^{\tau'}_{\beta}} \right|_0 . \tag{4.2}$$

In this work, $D^{\tau,\tau'}_{\alpha,\beta}$ is always a 120×120 matrix, with $\vec{v}$ denoting the 120-component atomic displacement vector in Cartesian coordinates, τ and τ' denoting atom indices (1 through 40),

and α and β denoting Cartesian indices (x, y, or z). For each composition, a force-constant matrix is calculated at each of the five biaxially strained reference structures defined above.

For each force-constant matrix, the eigenvectors and eigenvalues are determined by the eigenequation:

$$\sum_{\beta\tau'} D^{\tau,\tau'}_{\alpha,\beta}\xi^{\tau'}_{\beta}(j) = \lambda(j)\xi^{\tau}_{\alpha}(j). \tag{4.3}$$

Here, j is a mode index running from 1 to 120, $\lambda(j)$ is the j^{th} real-valued eigenvalue, and $\xi(j)$ is the j^{th} 120-component real-valued eigen-displacement vector.

The eigenvectors $\xi(j)$ form a complete orthonormal basis capable of describing any pattern of displacement having wavelengths commensurate with the supercell dimensions. This basis is more convenient than Cartesian coordinates under the assumption that the $\xi(j)$ corresponding to lower $\lambda(j)$ eigenvalues dominate in the lowest-energy structures. Because the eigenvalues $\lambda(j)$ track the curvature of the energy with respect to that displacement mode, very positive curvatures will tend to prohibit the appearance of these displacement modes in low energy structures.

The vector corresponding to the displacements within the 40-atom supercell can be written in terms of these eigenvectors $\xi(j)$ as:

$$\vec{v} = \sum_{j} u_j \xi(j). \tag{4.4}$$

Here, u_j is the j^{th} eigenmode coordinate, a real-valued scalar whose absolute value, the eigenmode amplitude, represents the degree to which the j^{th} eigenmode displacement pattern, $\xi(j)$, contributes to the atomic displacements. For any arbitrary structure considered in this study, the eigenmode coordinate is determined by a projection of the Cartesian displacement vector onto the eigenbasis:

$$u_j = \sum_{\tau\alpha} \xi^{\tau}_{\alpha}(j)\upsilon^{\tau}_{\alpha}. \tag{4.5}$$

An expansion of the total energy about the reference state is separated into four terms: [10]

$$E(\epsilon_{zz}, u_j; \bar{\eta}) = E_0 + E^{elas}(\epsilon_{zz}) + E^{disp}(u_j) + E^{int}(\epsilon_{zz}, u_j). \tag{4.6}$$

The misfit strain, $\bar{\eta}$, is a parameter that defines the reference state in the expansion and is not an expansion variable. Thus, E_0 is the energy of the tetragonally relaxed reference structure, and ϵ_{zz} is the out-of-plane strain relative to this reference.

As σ_{zz}, σ_{yz}, σ_{xz}, and atomic forces in the reference structures are zero, no first-order terms persist in the expansions. The pure elastic contributions to the total energy are thus described as:

$$E^{elas}(\epsilon_{zz}) = B_2\epsilon^2_{zz} + B_3\epsilon^3_{zz} + B_4\epsilon^4_{zz}. \tag{4.7}$$

For pure displacement terms, second-order cross terms ($u_i u_j$) also cannot persist due to the choice of eigenbasis, and third-order terms vanish due to centrosymmetry of the chosen reference structures under arbitrary homogeneous strain, ensuring that $E(\epsilon_{zz}, v_\alpha^\tau) = E(\epsilon_{zz}, -v_\alpha^\tau)$. The resulting fourth-order expansion for the pure displacement energy contribution is:

$$E^{disp}(u_j) = \sum_j \frac{1}{2}\lambda_j u_j^2 + C_j u_j^4, \tag{4.8}$$

where j is chosen in this work to include the nine most unstable (or soft) modes. For the interaction terms describing strain-displacement couplings, all second-order terms ($\epsilon_{zz} u_j$) vanish due to centrosymmetry, and the lowest-order term in the expansion, which is the only one retained in the current work, has the form:

$$E^{int}(\epsilon_{zz}, u_j) = \sum_j A_j \epsilon_{zz} u_j^2. \tag{4.9}$$

It is noted that there is a unique expansion for each composition at each misfit strain, resulting in $3 \times 5 = 15$ sets of expansion coefficients. There are many options for deciding the number of terms to keep in the above expansions. Although $(40 \times 3) - 3 = 117$ different eigenmode degrees of freedom exist, only up to nine are explicitly included in this work. By considering up to the nine softest eigenmodes, it is ensured that the three ferroelectric (FE) modes and the six octahedral rotational modes can always be considered if they are the most unstable. As these modes are commonly observed among perovskite oxides, they are essential in capturing common complex ground-state structures [80]. Further, although the above expansions can be taken to arbitrary order, this work truncates E^{elas} and E^{disp} to fourth order, truncates E^{int} to third order, and does not include cross-coupling displacement mode terms (*i.e.*, $u_i^2 u_j^2$-type terms). These truncations result in the smallest number of terms that still give rise to an expression that is guaranteed to have a bounded minimum. Higher-order terms could be included and would improve the accuracy, but the expansions of the present workflow are used only to find candidate metastable structures for subsequent input into DFT geometry optimizations, and thus the truncation to low order still provides sufficient accuracy for the purposes of the present work. Further, the present workflow's use of a distinct energy expansion at each misfit strain greatly helps to reduce the role that higher-order terms play in dictating the local minima of the potential energy landscape.

Validation of the assumptions underlying this approach are undertaken through comparisons to previous work (see Section 4.4.2), and for the compounds considered, the approach is found to be effective in identifying ground-state structures. For other systems requiring a more refined approximation to the energy landscape, the present approach can be extended straightforwardly by including more degrees of freedom and/or including additional higher-order terms.

The expansion coefficients defined in this section are determined through fitting to results of DFT calculations that consider different finite displacements and distortions of the

reference structures [15]. Details are discussed in Section A.2 of the appendix, which gives an example for the case of $SrTiO_3$.

4.2.2 Construction of Epitaxial Phase Diagrams

For each of the three compositions, and at each of five misfit strains, a set of candidate structures is generated by analytically solving for all minima of the total energy expansion defined in Section 4.2.1. These candidate structures are subsequently used as the starting configuration for a DFT calculation in which the structure is relaxed, keeping the in-plane strains fixed at the relevant value of $\bar{\eta}$. After all of the candidate structures have been relaxed, the DFT energies are compared to identify the most energetically stable (i.e., the lowest energy) state. The result is a set of five low-energy structures, one for each value of the misfit strain ($\bar{\eta}$ = -2, -1, 0, 1 and 2 %). For each of these five structures, an energy versus misfit strain curve is generated by re-relaxing the structures, with the in-plane strain fixed at several values of $\bar{\eta}$ on a finer grid spanning values between -4 to 4 %. Prior to these structural relaxations, the atom positions are given small random displacements in order to reduce the symmetry to $P1$, guaranteeing the final structures are stable with respect to distortions of the forty-atom cells. It is emphasized that out-of-plane shear strain degrees of freedom are not constrained during these structural optimizations, and the resulting lattice need not be tetragonal. The lowest energy phase at each misfit strain comprises the set of ground-state structures based on the 40-atom supercells, and from these structures the zero-temperature phase diagram versus misfit strain is thus produced.

4.2.3 Calculation Methods

All *ab initio* DFT calculations made use of the Vienna *ab initio* simulation package (VASP) [60–63] version 5.4.1. A conjugate-gradient algorithm was used for all structural relaxations. As the standard VASP software package does not allow for arbitrary mechanical boundary conditions, the relaxations under fixed in-plane strain made use of a custom modified version of the software in which certain components of the stress tensor are constrained to zero.

Calculations used the Ceperley-Alder form of the local density approximation (LDA) exchange-correlation functional, as parameterized by Perdew and Zunger [64], with the electron-ion interaction described by the projector augmented wave method [65, 66]. Force-constant matrices were calculated by Density Functional Perturbation Theory (DFPT) [22] at the zone center for each of the reference $2\times2\times2$ supercells. For all calculations required to compute expansion coefficients, and for the subsequent relaxations of candidate structures, use was made of a 600 eV plane-wave cutoff energy, $3 \times 3 \times 3$ Monkhorst-Pack sampling of the Brillouin zone [67], and Gaussian smearing of 0.01 eV.

More refined computational parameters were used in the final relaxations and polarization calculations in the construction of the ground-state phase diagrams. In these more refined calculations, an 800 eV plane-wave cutoff energy and a $4\times4\times4$ Monkhorst-Pack sampling of the Brillouin zone were used. All relaxations of the structures were continued until the forces

and out-of-plane stresses converged to magnitudes within 0.001 eV/Å and 0.005 eV/f.u., respectively, where eV/f.u. is per five-atom formula unit. The resulting level of convergence in energy differences is to within 0.1 meV/f.u.

The Berry phase approach, as described in the modern theory of polarization [24], was used to calculate the electric polarization vector at each misfit strain. All calculations assume a fixed (vanishing) external electric field corresponding to thin-films surrounded by perfectly charge-compensating electrodes, as discussed in Refs. [69, 70]. Further, use of the LDA in the present work leads to well-known systematic errors in the calculated lattice constants, amounting to an underestimation of their values on the order of a percent [4, 10]. Further discussion of the effect of the exchange correlation functional is given in Section A.3 of the appendix, in which the phase diagram for $CaTiO_3$ is recalculated using the SCAN meta-GGA functional [20]. A comparison between the LDA and SCAN results suggests that the predicted phases and their order with respect to misfit strain are equivalent, with the phase boundaries of SCAN shifted to epitaxial lattice constants that are approximately 1% larger in magnitude compared to LDA.

4.3 Results

4.3.1 Properties of Bulk Systems

The ground-state structures of bulk, unstrained $SrTiO_3$, $CaTiO_3$, and $SrHfO_3$ were calculated for use as energetic references, and their properties are listed in Table 4.1. $SrTiO_3$ adopts the tetragonal $I4/mcm$ structure, obtained by condensing an out-of-phase rotational instability (R_4^+ in the irreducible representation notation of Ref. [81]) about the direction of elongation. $CaTiO_3$ and $SrHfO_3$ adopt the orthorhombic $Pnma$ structure, obtained by condensing equal amplitudes of the R_4^+ mode about two axes and a unique amplitude of an in-phase rotational instability (M_3^+) about a third axis. Additional A-site displacement modes further contribute to these latter two structures, and these modes are discussed in more detail in the context of epitaxial structures in Section 4.4.4. None of the three bulk structures exhibits a macroscopic polarization.

4.3.2 Eigenmode Properties and Expansion Coefficients

Table 4.2 gives the properties of the nine most unstable or softest stable displacement eigenmodes at five misfit strains for $SrTiO_3$, $CaTiO_3$, and $SrHfO_3$. Properties listed include the Glazer system (detailed in Ref. [80]), eigenvalue, and mode polarization vector, $\vec{Z}$, which is defined as the dot product of the Born effective charge tensor [76] of the reference structure with the associated eigenvector:

$$\vec{Z}_i = \sum_{\tau\alpha} \xi_\alpha^\tau(i) Z_\alpha^{*\tau}. \tag{4.10}$$

Table 4.1: Bulk properties of the three compositions considered, including calculated cubic lattice constants, Goldschmidt tolerance factors [56], and spacegroups and Glazer systems [80] of the bulk ground-state phase.

Formula	a_0 (Å)	Tolerance Factor t	Spacegroup	Glazer System
$SrTiO_3$	3.86	1.001	$I4/mcm$	$a_0^0 a_0^0 c_0^-$
$CaTiO_3$	3.81	0.946	$Pnma$	$a_0^- a_0^- c_0^+$
$SrHfO_3$	4.07	0.949	$Pnma$	$a_0^- a_0^- c_0^+$

This vector represents the macroscopic polarization that develops per small increase in the i^{th} eigenmode coordinate. For plots of the eigenvalues of many of the eigenmodes listed in Table 4.2, see the bottom panels of Fig. 4.1. Table A.1 of the appendix lists the expansion coefficients defined in Section 4.2.1 for five values of the misfit strain for $SrTiO_3$, $CaTiO_3$, and $SrHfO_3$.

4.3.3 Epitaxial Phase Diagrams

Figure 4.1 plots the energies, polarization components, eigenmode amplitudes of the epitaxial ground-state structures, and the force-constant matrix eigenvalues of the tetragonal reference structures versus misfit strain for $SrTiO_3$, $CaTiO_3$, and $SrHfO_3$. The top panel of each plot corresponds to the energy and polarization of the ground-state structure as a function of misfit strain. The reference energy for each compound is that of the corresponding bulk, fully relaxed structure listed in Table 4.1. The energy values plotted in Fig. 4.1 can thus be interpreted as the elastic energy of the epitaxially constrained phase, and the more positive this energy is, the higher the driving force for strain relaxation, *e.g.*, through formation of misfit dislocations. Misfit strains corresponding to phase transitions are indicated by dashed vertical lines, and the spacegroups of the epitaxial phases in each misfit strain regime are indicated in the top panels. The horizontal scale given at the top of each figure indicates the cubic substrate lattice constant, a, required to produce the given degree of misfit strain, with $a = a_0(\bar{\eta} + 1)$.

The eigenmode amplitudes shown in the middle panels are determined by Eq. 4.5. These measure the degree to which the three FE eigenmodes at Γ (Fig. 4.2a) and six rotational displacement eigenmodes at the M (Fig. 4.2b) and R (Fig. 4.2c) boundary points of the Brillouin zone of the cubic perovskite compound have condensed in the ground-state epitaxial structures. The eigenvalues corresponding to these nine modes are plotted in the bottom panels and are determined from diagonalization of the force-constant matrices of the tetragonal reference structures.

Figure 4.1a plots the ground-state epitaxial properties for $SrTiO_3$. Under strong biaxial compression, a polar $I4cm$ phase is predicted having two displacement modes activated,

Table 4.2: Properties of the nine softest eigen-displacement modes at various misfit strains for $SrTiO_3$, $CaTiO_3$, and $SrHfO_3$. Properties listed include the tilt system of each eigenmode, as denoted by the modified Glazer notation, the eigenvalue, λ_i ($eV/Å^2$), of the i^{th} displacement mode, and the mode polarization vector, $\vec{Z}_i$ (C/m^2), as defined in Eq. 4.10 of Section 4.3.2. A '*' denotes a trivial translational eigenmode which must have an eigenvalue of zero and vanishing polarization vector, while 'N/A' denotes a displacement mode that cannot be described by the Glazer notation.

$SrTiO_3$		Eigenmode Index								
Misfit Strain		1	2	3	4	5	6	7	8	9
	Glazer	$a_0^0a_0^0c_+^0$	$a_0^0a_0^0c_0^-$	$a_0^0a_0^0c_0^+$	$a_0^-b_0^0b_0^0$	$a_0^0b_0^-a_0^0$				$a_0^+b_0^0b_0^0$
-2%	λ_i	-2.06	-1.1	-0.69	-0.46	-0.46	*	*	*	0.07
	$\vec{Z}_i$	(0 0 0.9)	**0**	**0**	**0**	**0**				**0**
	Glazer	$a_0^0a_0^0c_+^0$	$a_0^0a_0^0c_0^-$	$a_0^-b_0^0b_0^0$	$a_0^0b_0^-a_0^0$	$a_0^0a_0^0c_0^+$	$a_0^+b_0^0b_0^0$	$a_0^0b_0^+a_0^0$		
-1%	λ_i	-0.81	-0.76	-0.49	-0.49	-0.33	-0.01	-0.01	*	*
	$\vec{Z}_i$	(0 0 0.9)	**0**	**0**	**0**	**0**	**0**	**0**		
	Glazer	$a_0^-b_0^0b_0^0$	$a_0^0b_0^-a_0^0$	$a_0^0a_0^0c_0^-$	$a_0^+b_0^0b_0^0$	$a_0^0b_0^+a_0^0$	$a_0^0a_0^0c_0^+$			
0%	λ_i	-0.49	-0.49	-0.48	-0.05	-0.05	-0.04	*	*	*
	$\vec{Z}_i$	**0**	**0**	**0**	**0**	**0**	**0**			
	Glazer	$a_+^0b_0^0b_0^0$	$a_0^0b_+^0a_0^0$	$a_0^-b_0^0b_0^0$	$a_0^0b_0^-a_0^0$	$a_0^0a_0^0c_0^-$	$a_0^+b_0^0b_0^0$	$a_0^0b_0^+a_0^0$		
1%	λ_i	-1.18	-1.18	-0.52	-0.52	-0.27	-0.12	-0.12	*	*
	$\vec{Z}_i$	(0.9 0 0)	(0 0.9 0)	**0**	**0**	**0**	**0**	**0**		
	Glazer	$a_+^0b_0^0b_0^0$	$a_0^0b_+^0a_0^0$	N/A	N/A	$a_0^-b_0^0b_0^0$	$a_0^0b_0^-a_0^0$	$a_0^+b_0^0b_0^0$	$a_0^0b_0^+a_0^0$	$a_0^0a_0^0c_0^-$
2%	λ_i	-2.81	-2.81	-1.4	-1.4	-0.52	-0.52	-0.14	-0.14	-0.11
	$\vec{Z}_i$	(0.9 0 0)	(0 0.9 0)	**0**	**0**	**0**	**0**	**0**	**0**	**0**
$CaTiO_3$		1	2	3	4	5	6	7	8	9
	Glazer	$a_0^0a_0^0c_0^-$	$a_0^0a_0^0c_+^0$	$a_0^0a_0^0c_0^+$	$a_0^-b_0^0b_0^0$	$a_0^0b_0^-a_0^0$	$a_0^+b_0^0b_0^0$	$a_0^0b_0^+a_0^0$	$a_+^0b_0^0b_0^0$	$a_0^0b_+^0a_0^0$
-2%	λ_i	-3.53	-3.27	-3.23	-3.05	-3.05	-2.69	-2.69	-1.2	-1.2
	$\vec{Z}_i$	**0**	(0 0 0.8)	**0**	**0**	**0**	**0**	**0**	(0.67 0 0)	(0 0.67 0)
	Glazer	$a_0^0a_0^0c_0^-$	$a_0^-b_0^0b_0^0$	$a_0^0b_0^-a_0^0$	$a_0^0a_0^0c_0^+$	$a_0^+b_0^0b_0^0$	$a_0^0b_0^+a_0^0$	$a_0^0a_0^0c_+^0$	$a_+^0b_0^0b_0^0$	$a_0^0b_+^0a_0^0$
-1%	λ_i	-3.15	-2.94	-2.94	-2.84	-2.61	-2.61	-2.35	-1.47	-1.47
	$\vec{Z}_i$	**0**	**0**	**0**	**0**	**0**	**0**	(0 0 0.76)	(0.69 0 0)	(0 0.69 0)
	Glazer	$a_0^-b_0^0b_0^0$	$a_0^0b_0^-a_0^0$	$a_0^0a_0^0c_0^-$	$a_0^+b_0^0b_0^0$	$a_0^0b_0^+a_0^0$	$a_0^0a_0^0c_0^+$	$a_+^0b_0^0b_0^0$	$a_0^0b_+^0a_0^0$	$a_0^0a_0^0c_+^0$
0%	λ_i	-2.83	-2.83	-2.8	-2.53	-2.53	-2.5	-1.91	-1.91	-1.77
	$\vec{Z}_i$	**0**	**0**	**0**	**0**	**0**	**0**	(0.72 0 0)	(0 0.72 0)	(0 0 0.71)
	Glazer	$a_0^-b_0^0b_0^0$	$a_0^0b_0^-a_0^0$	$a_0^0a_0^0c_0^-$	$a_+^0b_0^0b_0^0$	$a_0^0b_+^0a_0^0$	$a_0^+b_0^0b_0^0$	$a_0^0b_0^+a_0^0$	$a_0^0a_0^0c_0^+$	$a_0^0a_0^0c_+^0$
1%	λ_i	-2.73	-2.73	-2.53	-2.5	-2.5	-2.45	-2.45	-2.22	-1.4
	$\vec{Z}_i$	**0**	**0**	**0**	(0.75 0 0)	(0 0.75 0)	**0**	**0**	**0**	(0 0 0.66)
	Glazer	$a_+^0b_0^0b_0^0$	$a_0^0b_+^0a_0^0$	$a_0^-b_0^0b_0^0$	$a_0^0b_0^-a_0^0$	$a_0^+b_0^0b_0^0$	$a_0^0b_0^+a_0^0$	$a_0^0a_0^0c_0^-$	$a_0^0a_0^0c_0^+$	$a_0^0a_0^0c_+^0$
2%	λ_i	-3.24	-3.24	-2.61	-2.61	-2.35	-2.35	-2.29	-1.98	-1.21
	$\vec{Z}_i$	(0.78 0 0)	(0 0.78 0)	**0**	**0**	**0**	**0**	**0**	**0**	(0 0 0.61)
$SrHfO_3$		1	2	3	4	5	6	7	8	9
	Glazer	$a_0^0a_0^0c_0^-$	$a_0^0a_0^0c_0^+$	$a_0^-b_0^0b_0^0$	$a_0^0b_0^-a_0^0$	$a_0^+b_0^0b_0^0$	$a_0^0b_0^+a_0^0$	$a_0^0a_0^0c_+^0$	N/A	N/A
-2%	λ_i	-2.74	-2.46	-2.27	-2.27	-1.91	-1.91	-1.31	-0.48	-0.45
	$\vec{Z}_i$	**0**	**0**	**0**	**0**	**0**	**0**	(0 0 -0.45)	**0**	**0**
	Glazer	$a_0^0a_0^0c_0^-$	$a_0^-b_0^0b_0^0$	$a_0^0b_0^-a_0^0$	$a_0^0a_0^0c_0^+$	$a_0^+b_0^0b_0^0$	$a_0^0b_0^+a_0^0$	$a_0^0a_0^0c_+^0$	$a_+^0b_0^0b_0^0$	$a_0^0b_+^0a_0^0$
-1%	λ_i	-2.33	-2.11	-2.11	-2.04	-1.8	-1.8	-0.72	-0.21	-0.21
	$\vec{Z}_i$	**0**	**0**	**0**	**0**	**0**	**0**	(0 0 -0.42)	(0.38 0 0)	(0 0.38 0)
	Glazer	$a_0^-b_0^0b_0^0$	$a_0^0b_0^-a_0^0$	$a_0^0a_0^0c_0^-$	$a_0^+b_0^0b_0^0$	$a_0^0b_0^+a_0^0$	$a_0^0a_0^0c_0^+$	$a_+^0b_0^0b_0^0$	$a_0^0b_+^0a_0^0$	$a_0^0a_0^0c_+^0$
0%	λ_i	-1.98	-1.98	-1.97	-1.69	-1.69	-1.68	-0.41	-0.41	-0.39
	$\vec{Z}_i$	**0**	**0**	**0**	**0**	**0**	**0**	(0.39 0 0)	(0 0.39 0)	(0 0 0.39)
	Glazer	$a_0^-b_0^0b_0^0$	$a_0^0b_0^-a_0^0$	$a_0^0a_0^0c_0^-$	$a_0^+b_0^0b_0^0$	$a_0^0b_0^+a_0^0$	$a_0^0a_0^0c_0^+$	$a_+^0b_0^0b_0^0$	$a_0^0b_+^0a_0^0$	N/A
1%	λ_i	-1.88	-1.88	-1.67	-1.61	-1.61	-1.38	-0.74	-0.74	-0.41
	$\vec{Z}_i$	**0**	**0**	**0**	**0**	**0**	**0**	(0.39 0 0)	(0 0.39 0)	**0**
	Glazer	$a_0^-b_0^0b_0^0$	$a_0^0b_0^-a_0^0$	$a_0^+b_0^0b_0^0$	$a_0^0b_0^+a_0^0$	$a_0^0a_0^0c_0^-$	$a_0^0a_0^0c_0^+$	$a_+^0b_0^0b_0^0$	$a_0^0b_+^0a_0^0$	N/A
2%	λ_i	-1.78	-1.78	-1.53	-1.53	-1.41	-1.12	-1.11	-1.11	-0.77
	$\vec{Z}_i$	**0**	**0**	**0**	**0**	**0**	**0**	(0.39 0 0)	(0 0.39 0)	**0**

an out-of-plane octahedral rotation R_4^+ mode (orange diamonds in the middle and bottom panels) and an out-of-plane zone-centered FE mode (blue diamonds). These are also the two most unstable modes of the reference tetragonal structures in the compressive regime, as indicated in the bottom panel. As the strain becomes less compressive, both modes gradually diminish until the FE mode entirely vanishes, giving way to the paraelectric $I4/mcm$ phase beginning at -1% misfit strain. In this region, only the R_4^+ mode persists, and its amplitude continues to diminish until 0.25% misfit strain, at which point the polar $Ima2$ phase sets in through a first-order transition. The $Ima2$ phase consists of four active displacement modes, including two in-plane octahedral rotation R_4^+ modes (gray squares and purple triangles) and two in-plane zone-centered FE modes (red squares and green triangles). These are also the four most unstable modes of the reference tetragonal structures in the tensile strain regime, as shown in the bottom panel. With increasing tensile strain, the two in-plane octahedral rotation R_4^+ modes in the $Ima2$ phase tend to remain approximately constant in their eigenmode amplitudes, while the in-plane FE modes gradually increase in eigenmode amplitude. The elastic energy curve for $SrTiO_3$ is symmetric with respect to misfit strain, having a minimum at 0% misfit strain and approximately 150 meV/f.u. of elastic energy at the extremes of compressive and tensile misfit strain considered.

Figure 4.1b plots the ground-state epitaxial properties for $CaTiO_3$. Compared to $SrTiO_3$, the predicted phases of $CaTiO_3$ involve a more complicated interplay of a larger number of displacement modes. From -4% to -2.5% misfit strain, the polar Pm phase is predicted as a ground-state structure, for which the atomic displacements involve a combination of an out-of-plane FE, in-plane R_4^+ rotation, in-plane M_3^+ rotation, and out-of-plane R_4^+ rotation mode. As the magnitude of biaxial compressive strain is reduced, the two in-plane rotational modes slightly increase in amplitude, while the two out-of-plane modes diminish. At -2.5% misfit strain, the amplitude of the out-of-plane FE mode vanishes, and the non-polar $P2_1/m$ parent phase becomes stable in a smooth second-order transition. This phase persists from -2.5% to 0% misfit strain, over which the in-plane rotation modes continue to slowly increase in amplitude while the out-of-plane rotation mode continues to diminish. At zero misfit strain, the three octahedral modes are discontinuously replaced by two in-plane FE, one out-of-plane M_3^+ rotation, and two in-plane R_4^+ rotation modes in a first-order transition to the polar $Pmn2_1$ phase. This phase persists to the extreme of tensile strain considered, with the in-plane FE modes gradually growing and the octahedral modes remaining roughly constant in amplitude. The elastic energy curve of $CaTiO_3$ has its minimum shifted to -1% misfit strain. This shift is possible because the energy curve is referenced to the fully relaxed bulk $CaTiO_3$ structure, while the misfit strain is referenced to the equilibrium lattice constant of a bulk cubic structure. The energy curve reflects this with 100 meV/f.u. of elastic energy at -4% misfit strain and 250 meV/f.u. at 4% misfit strain.

Figure 4.1c plots the calculated properties for $SrHfO_3$. Like $CaTiO_3$, this system exhibits a complicated interplay of many displacement modes. Under large compressive strain, a paraelectric $I4/mcm$ phase is predicted, having only an out-of-plane R_4^+ rotation mode active. At -3% misfit strain, there is a first-order transition to a paraelectric $P2_1/m$ phase. Continuing to -1% misfit strain, there is another first-order phase transition to a paraelectric

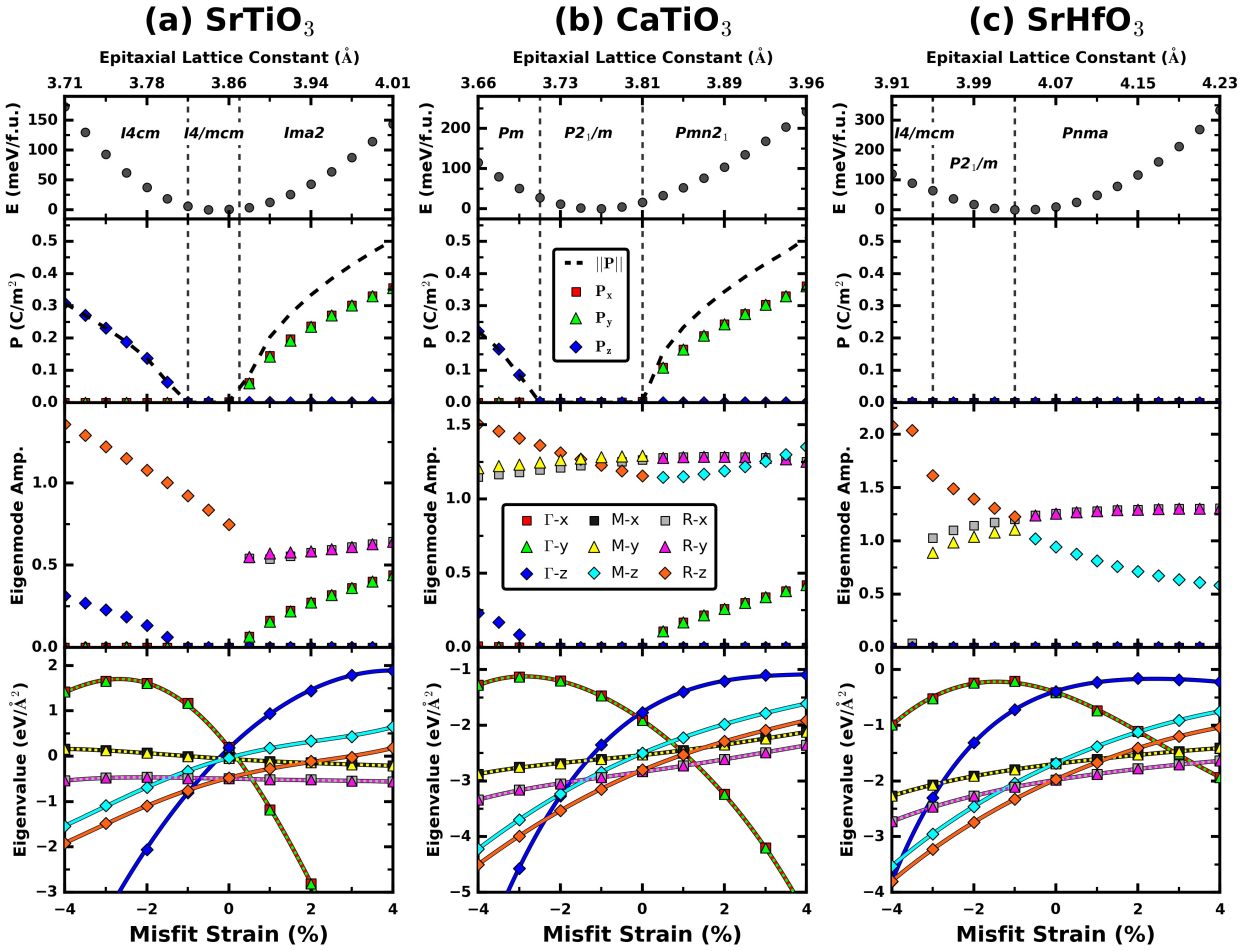

Figure 4.1: Plots of ground-state epitaxial structure energies, polarization components, eigenmode amplitudes, and tetragonal reference structure eigenvalues versus misfit strain for a) $SrTiO_3$, b) $CaTiO_3$, and c) $SrHfO_3$. Absolute values of polarization components are taken for visualization purposes. The in-plane lattice constant of the epitaxial structure at each misfit strain is indicated by the top axis. The lower legend corresponds to the eigenmodes shown in Fig. 4.2 realized down the x, y, or z axes.

Pnma phase that is like the bulk *Pnma* phase, but with a tetragonal lattice instead of orthorhombic. An orthorhombic rather than tetragonal space group is adopted in this case due to symmetry-lowering atomic displacements in the epitaxial ground-state structure. This *Pnma* phase remains stable to the extreme of tensile strain considered, with the in-plane R_4^+ rotation mode amplitudes remaining nearly constant, and the out-of-plane M_3^+ mode amplitude diminishing. The elastic energy curve for $SrHfO_3$ is asymmetric, having a -1% shift in the minimum, 100 meV/f.u. elastic energy at -4% misfit strain, and over 300 meV/f.u. elastic energy at 4% misfit strain.

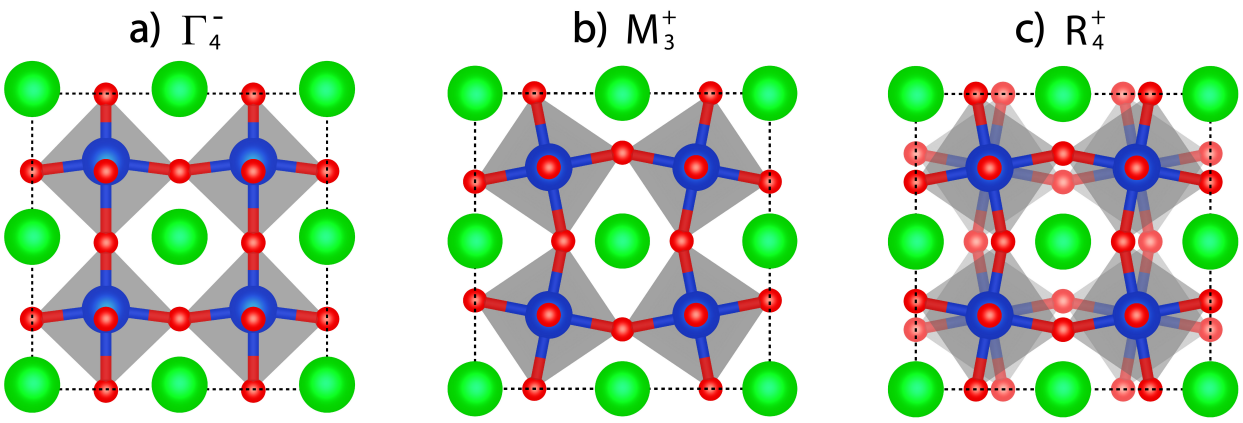

Figure 4.2: The three most dominant unstable eigenmodes for epitaxial $SrTiO_3$, $CaTiO_3$, and $SrHfO_3$. a) The zone-centered FE mode, often transforming like the irrep Γ_4^-, b) the in-phase AFD octahedral rotation, transforming like the irrep M_3^+, and c) the out-of-phase AFD octahedral rotation, transforming like the irrep R_4^+. All three can be independently realized down each of the three unit-cell axes. This figure was created using VESTA [55].

4.4 Discussion

4.4.1 Comparison to Previous Calculations

In order to validate the accuracy of the present computational approach, results are compared in this section to previous DFT calculations that include some form of input from experimental observations or phenomenological theory. As discussed below, the present work correctly leads to the identification of stable phases reported previously for epitaxially strained $SrTiO_3$ and $CaTiO_3$. Quantitative discrepancies with these previous computational investigations, that do not relate to the efficacy of the present structure optimization approach, are found and attributed to differences in the numerical parameters in the underlying DFT calculations.

Lin *et al.* [79] use DFT to calculate the epitaxial phase diagram of $SrTiO_3$ by considering all phases predicted by phenomenological Landau theory [82]. The general polarization behavior and stable phases at the extremes of misfit strain compare very well to that of the present work. Specifically, the results from both studies feature the stability of an $I4cm$ phase with enhanced out-of-plane polarization under compression and an $Ima2$ phase with enhanced in-plane polarization under tension. Near 0% misfit strain, the two works differ in their predicted phases. While the present work predicts a paraelectric $I4/mcm$ phase near 0% misfit strain, Ref. [79] predicts a total of three phases in this same region of strains, including, in addition to the $I4/mcm$ phase, two other polar phases with $Ima2$ and $Fmm2$ symmetries. These differences arise due to the near energetic degeneracy of the competing phases, such that differences in the parameters underlying the DFT calculations can influence conclusions about relative stability. To ensure this is the case, rather than being due to the

underlying structural optimization procedure of the present workflow, the energy of the $Ima2$ and $Fmm2$ phases were computed using the computational parameters given in Section 4.2.3, featuring a plane wave cutoff nearly twice as large as that employed in Ref. [79]. Consistent with the results shown in Fig. 4.1, with the DFT parameters employed in the present work, it was verified that the lowest energy structure was the one with $I4/mcm$ symmetry, with the $Ima2$ and $Fmm2$ polymorphs being higher in energy and therefore metastable.

For $CaTiO_3$, Eklund *et al.* [78] computed epitaxial phase diagrams using DFT by considering the relative stability of a number of candidate phases derived from the experimentally observed bulk phase. There is good agreement between the present results and the work in Ref. [78] in terms of the stable phases predicted, with both studies determining the $P2_1/m$ phase to be stable under moderate compression and the $Pmn2_1$ phase to be stable under tension. The strain corresponding to the transition between these two phases is quantitatively different in the two studies, however: Eklund *et al.* find a value of $\bar{\eta} = 0\%$ while in the present work this value is approximately 2%. As above, these quantitative differences are likely a consequence of the different DFT parameters employed in the two studies.

4.4.2 Role of Non-Zone-Center Displacement Modes

In previous work by the authors [77], epitaxial phase diagrams were calculated using a similar approach as described here, but disallowing relaxations associated with non-zone-center displacement modes. In other words, the work in Ref. [77] considered only phases that could be derived from the perovskite structure through homogeneous strains and zone-centered FE displacement modes. A comparison of the results obtained in Ref. [77] with those obtained in the present work is therefore of interest, as it highlights the role of non-zone-centered distortions, such as octahedral rotations, in determining the structural, energetic, and polarization dependences on epitaxial strain. Such information is of interest because non-zone-centered distortions may be frozen out in very thin films if they increase the interfacial energy, while they may be present in thicker films if they reduce strain energy.

For $SrTiO_3$, the effect of non-zone-centered distortions is to widen the range of stability of the paraelectric phase by nearly 0.5% misfit strain. Specifically, octahedral rotations reduce the strain energy by 147 meV/f.u. at -4% misfit strain, and by 86 meV/f.u. at 4% misfit strain. This implies that rotational modes reduce elastic energy and should allow for larger critical thicknesses for epitaxial growth. Under compressive epitaxial strain, the out-of-plane polarization is nearly halved when the out-of-plane rotation is allowed, implying an unfavorable coupling with the out-of-plane FE mode. In contrast, under tensile misfit strain, the presence of the two in-plane R_4^+ octahedral rotation modes does not significantly change the polarization compared to the results obtained from disallowing non-zone-center distortions.

For $SrHfO_3$, much larger effects of non-zone-center modes are found. The elastic energy is reduced by 343 meV/f.u. at -4% misfit strain and 109 meV/f.u. at 4% misfit strain when the non-zone-centered modes are allowed. Also, in the calculations where non-zone-center distortions are disallowed, large polarizations are computed, up to 0.56 C/m^2, and a direct

transition from a $P4mm$ phase with purely out-of-plane polarization to a $Pmm2$ phase with purely in-plane polarization is predicted around 0% misfit strain. The presence of non-zone-centered distortions in $SrHfO_3$ strongly suppresses these two phenomena, giving way to a paraelectric film over the entire range of epitaxial strain between -4% and 4%.

4.4.3 Predominant Displacement Modes

The atomic displacements calculated in the present work for the epitaxial ground-state structures of $SrTiO_3$, $CaTiO_3$, and $SrHfO_3$ can be predominantly decomposed into a small set of displacement eigenmodes. Figure 4.2 shows the displacement patterns of the most dominant unstable eigenmodes, including a zone-centered FE distortion wherein the B-cations shift against the other sublattices (Fig. 4.2a, irreducible representation Γ_4^-), and two types of AFD octahedral rotations wherein the oxygen octahedra rotate either out of phase (Fig. 4.2b, R_4^+) or in phase (Fig. 4.2c, M_3^+) along an axis. Note that the irreducible representation of the FE mode can vary with composition and misfit strain and need not be Γ_4^-, although this is the most common, whereas the octahedral rotation modes are uniquely determined by symmetry. Each of these three displacement patterns can be independently realized along each of the three orthogonal unit cell axes, leading to nine dominating displacement eigenmodes. Linear combinations of these nine eigenmodes account for 95.8% of the total atomic displacement predicted in the ground-state epitaxial phases of $SrTiO_3$, 70.1% of the total displacement in $CaTiO_3$ and 77.2% in $SrHfO_3$.

Even in cases where other displacement modes are more unstable in the reference tetragonal structures, combinations of the nine modes described in the previous paragraph still dominate in their contribution to the atomic displacements of the relaxed epitaxial ground-state structures. Table 4.2 gives the sets of nine eigenmodes with the most unstable eigenvalues for each of the reference tetragonal structures at various misfit strains. In some cases, denoted by an 'N/A' in the Glazer system entry in Table 4.2, these sets include modes other than the nine dominant modes described in the previous paragraph. However, even when these other modes are more unstable, the nine modes described in the previous paragraph still dominate in contributions to calculated displacement patterns in the relaxed ground-state structures. This tendency implies that the displacement modes illustrated in 4.4.3 have a more optimal balance of strong instability and favorable coupling with each other than other subsets of displacement modes.

For example, when $\bar{\eta} \geq 2\%$ for $SrTiO_3$, two symmetry-equivalent in-plane AFD modes have more negative eigenvalues in the reference tetragonal structures than all six of the R_4^+ and M_3^+ rotational modes. Yet, these two in-plane AFD modes do not contribute significantly to the calculated displacements in the relaxed ground-state structures of $SrTiO_3$ for strains ranging between 2% to 4%, while three of the six R_4^+ and M_3^+ rotational modes make large contributions to these displacements. Likewise, under large biaxial compressive or tensile strains, $SrHfO_3$ also has other unstable eigenmodes in the tetragonal reference structures that ultimately do not contribute significantly to the atomic displacements in the relaxed ground-state structures.

4.4.4 Role of *A*-Site Bonding

Although the nine dominant displacement modes illustrated in Fig. 4.2 largely describe the atomic displacements calculated for $SrTiO_3$, the ground-state epitaxial structures of $CaTiO_3$ and $SrHfO_3$ also have non-negligible atomic displacement contributions from a few additional stable or weakly unstable displacement eigenmodes. Of these, the most relevant is an antipolar *A*-site mode transforming like the irreducible representation X_5^+, shown in Fig. 4.3a. As described in detail in Ref. [16], the X_5^+ mode is energetically favorable when both the R_4^+ and M_3^+ rotational modes are present. Thus, most epitaxial ground-state structures for $CaTiO_3$ and $SrHfO_3$ predicted in this work show a significant antipolar shift in the *A*-sublattice with some dependence on misfit strain. Although these modes contribute less than 30% of the total atomic displacement in the relaxed structures, their impact on energy is still significant.

In order to determine the energetic influence of these eigenmodes having predominantly *A*-site displacements, the energies of the ground-state structures for $CaTiO_3$ and $SrHfO_3$ are re-calculated for modified structures in which only the contributions to the displacements associated with the nine dominant eigenmodes illustrated in Fig. 4.2 are kept, all other amplitudes being set to zero. The primary effect of this constraint is to disallow the structure to shift the *A*-site sublattices. Figure 4.3b shows the resulting energy curves versus misfit strain for $CaTiO_3$ and $SrHfO_3$. For $CaTiO_3$, removing all but the nine dominant modes from the structures increases the energy by up to 250 meV/f.u., with the most pronounced effects at the extremes of misfit strain. For $SrHfO_3$, the energetic influence is smaller, but still significant, with a maximum increase in energy of 80 meV/f.u at $\bar{\eta} = -2\%$. At $\bar{\eta} = -4\%$, contributions of modes other than the dominant nine vanish in $SrHfO_3$.

The reason these *A*-site displacement modes are important in $CaTiO_3$ and $SrHfO_3$, but not in $SrTiO_3$, can be explained by simple geometrical considerations. The relative ratios of the *A*- and *B*-cation radii, as characterized by the Goldschmidt tolerance factor (t) [56], are very different in these two cases. While $SrTiO_3$ ($t = 1.001$) has a tolerance factor that is close to unity, implying the *A* and *B* cations have radii nearly perfectly suited to the ideal perovskite structure, $CaTiO_3$ ($t = 0.946$) and $SrHfO_3$ ($t = 0.949$) have *A* cations that are relatively too small. As a result, the *A*-site coordination environment is unfavorable in the latter two systems, which explains why the eigenvalues of the $CaTiO_3$ and $SrHfO_3$ tetragonal reference structures are consistently 2-3 eV/Å^2 lower in value than those of $SrTiO_3$ for both the FE and AFD rotational eigenmodes (see bottom panels of Fig. 4.1). Both FE and AFD eigenmodes can optimize the *A*-site bonding, although octahedral rotations tend to do so more effectively and, thus, contribute more significantly to atomic displacements in the ground-state structures of $CaTiO_3$ and $SrHfO_3$ [16]. These rotations alone, however, are not enough to satisfy the *A*-site bonding preferences, which is why additional displacement modes, such as the antipolar *A*-site X_5^+ eigenmode shown in Fig. 4.3a, also condense in the structure. These modes further serve to minimize *A*-*O* repulsion and optimize the undersized *A*-site's coordination [16]. This can be visualized in the displacement pattern of the X_5^+ mode, which brings the *A*-cations closer the square oxygen interstice, while also

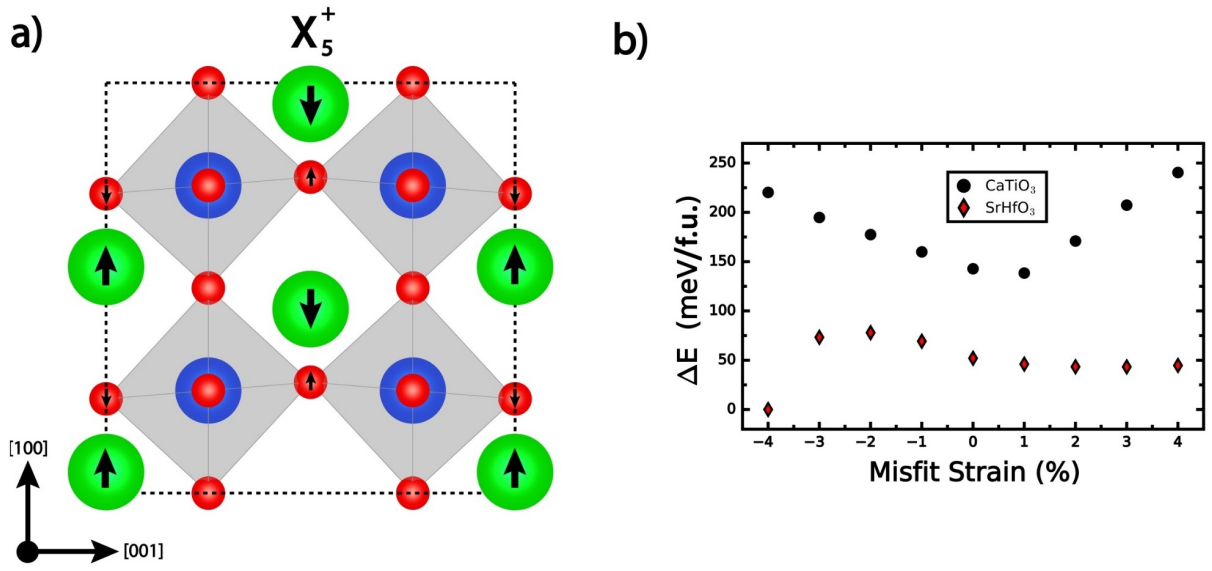

Figure 4.3: a) Antipolar A-site displacement mode (irreducible representation X_5^+). This mode can be independently realized down each of the three unit-cell axes. b) Metastability relative to the ground-state structures of $CaTiO_3$ and $SrHfO_3$ resulting from the eigenmode amplitudes of all modes other than the nine mentioned in Section 4.4.3 being set to zero. Part a) of this figure was created using VESTA [55].

drawing some of the equatorial oxygen atoms toward the A-cations. Figure 4.3b illustrates that these A-site bond-optimizing modes can be important in lowering strain energy, and that the degree to which these modes are needed to optimize the A-site bonding are highly sensitive to both the misfit strain and composition of the system.

4.4.5 Behavioral Trends

Irrespective of differences in cation bonding preferences between $SrTiO_3$, $CaTiO_3$, and $SrHfO_3$, the results of this work demonstrate many shared features among the behavior of the three compositions under epitaxy. In all three systems, application of misfit strain consistently destabilizes the B-site coordination environment, leading to growing FE eigenmode instabilities under both compression and tension. Increasing biaxial compressive strains lead to the out-of-plane FE displacement mode becoming more unstable, while increasing biaxial tensile strains always leads to the two in-plane FE modes becoming more unstable. The bottom panels in Fig. 4.1 indicate for all three systems that the FE modes of the tetragonal reference structures couple much more strongly to misfit strain than any of the octahedral rotation modes. The next strongest couplings occur in the two out-of-plane rotation modes, which are both strongly destabilized by increasing compressive strains, while the in-plane rotation modes have the weakest coupling to misfit strain.

4.5 Summary

Presented in this work is a computational framework for the calculation of ground-state epitaxial phase diagrams of ferroelectric perovskite oxides. This framework employs expansions of the total energy at various misfit strains with respect to soft-mode displacements and homogeneous deformations, in order to locate candidate ground-state structures, which are then further optimized through DFT calculations. Competing phases are predicted entirely from first-principles, with no assumptions made regarding which set of displacement modes to consider and no requirement of input information from experimental measurements. This method also considers the important effects of AFD and A-site displacement modes in ground-state epitaxial phases. The approach outlined in this work for identifying ground-state phases under epitaxial strain can be used in future work to treat a larger range of perovskite systems in order to explore compositional trends more broadly. This approach is demonstrated in the present work in an application to three perovskite oxides, $SrTiO_3$, $CaTiO_3$, and $SrHfO_3$, over a range of epitaxial strains applied parallel to the (001) plane. The main conclusions can be summarized as follows.

Compared to calculations in which relaxations associated with non-zone-centered displacement modes are disallowed, the present results show that inclusion of non-zone-centered displacement modes significantly affects the dependence of energy and polarization on misfit strain. Namely, AFD octahedral rotations and associated A-site displacement modes tend to strongly suppress polarization and also reduce the epitaxial strain energy. This information has important consequences for the stability of competing phases as a function of film thickness. Non-zone-centered distortions can be frozen out in very thin films if they increase interfacial energy with the underlying substrate lattice, while these distortions are likely to appear in thicker films because they reduce strain energy. In this way, competing phases with very different polar properties have the potential to be accessed as a function of film thickness.

A set of nine displacement modes, three zone-centered FE distortions often transforming like Γ_4^-, and six AFD octahedral rotations, three transforming like R_4^+ and three like M_3^+, comprise the largest contributors to the atomic displacements found in the calculated ground-state structures across all of the compositions and misfit strains considered. Combinations of these modes dominate atomic displacements in stable epitaxial phases even when other modes show more unstable eigenvalues in the high-symmetry reference structures. While the atomic displacements of $SrTiO_3$ can almost entirely be decomposed into contributions from these nine dominant displacement modes, those obtained for $CaTiO_3$ and $SrHfO_3$ also contain significant contributions from additional predominantly A-site displacement modes. This difference between $SrTiO_3$ and the other two compounds is driven by A-site bonding preference. The main effect of these additional modes is an antipolar A-site shift that significantly lowers strain energies of the epitaxial phases by optimizing the coordination geometry of the A-site cation.

CHAPTER 5

Electronic and Polar Properties of Vanadate Compounds Stabilized by Epitaxial Strain

5.1 Motivation and Overview

Vanadate compounds are observed to form in a variety of crystalline structures, where the coordination of the vanadium by oxygen can be octahedral, square pyramidal, trigonal bipyramidal, or tetrahedral [83]. Correlating with this structural variety, these compounds can be metals, insulators, ferroelectrics, ferromagnets, and potentially multiferroics [84]. The wide range of bonding behavior and associated physical properties can be attributed, in part, to vanadium having three different oxidation states (3+, 4+ and 5+) as well as to vanadium's ability to form strong directional bonds with oxygen. The oxovanadium (IV) ion, VO^{2+}, where V is in the 4+ oxidation state, is one of the most stable biatomic ions known [85], having a vanadyl short double bond characterized by a bond-length of approximately 1.60 Å and significant π-bonding [86]. Further, when V is in the 5+ oxidation state, the $3d$ shells of vanadium are empty, but still near enough to $4s$ and $4p$ orbitals to allow for the hybridized bonding behavior with oxygen characteristic of many transition metals [87].

The $PbVO_3$ (PVO) compound has been the subject of recent experimental and computational studies due to its potential for exhibiting magneto-electric coupling. Under pressure [88] and in epitaxially strained thin films [8], PVO has been reported to form in perovskite-derivative structures that are not observed under ambient conditions. These pressure- and strain-stabilized structures are observed to display a weak vanadyl short bond, square-pyramidal vanadium coordination, and super tetragonality. The vanadium ion has been measured to be in the 4+ oxidation state with a single occupied d orbital, thus having potential for multiferroicity [8]. These experimental studies of PVO have been augmented by computational investigations employing density-functional-theory (DFT) approaches [84, 88–90], which have elucidated key features of the electronic structure and reported a giant electric polarization of 1.52 C/m^2.

The work in this chapter has been submitted for publication in Chemistry of Materials, by T. Angsten, L. W. Martin and M. Asta, and is reproduced here with permission of the co-authors.

In contrast to PVO, relatively little attention has been devoted to exploring strain stabilization of perovskite-derivative structures in alternate vanadate compounds. This is perhaps because many of these systems are non-ferroic in their bulk equilibrium phases under ambient conditions. For example, if the Pb cation in PVO is replaced with a divalent alkaline earth metal, observed equilibrium phases include a metallic cubic perovskite structure (*e.g.*, $SrVO_3$) and a non-polar $GdFeO_3$-type structure (*e.g.*, $CaVO_3$) [91]. If Pb in PVO is replaced with a monovalent alkali metal, a non-polar centrosymmetric clinopyroxine or orthopyroxine structure results (*e.g.*, KVO_3) [92]. However, in the same manner that the perovskite-derivative structure of PVO must be externally stabilized through the application of strain, similar structures could form and exhibit ferroic properties for other vanadate systems under yet-unexplored epitaxial strain conditions.

In the present study, we employ DFT-based approaches in a computational investigation of the atomic and electronic structure, and energetic and polar properties of KVO_3 and $NaVO_3$ perovskite-derivative compounds under biaxial epitaxial strain. We further compare the atomic and electronic properties of these compounds with those computed for the experimentally-observed structure of PVO. For KVO_3, it is shown that a perovskite-derivative structure with spacegroup Cm is energetically stabilized under levels of compressive biaxial strains that could be achievable in thin-film growth experiments. For $NaVO_3$, a perovskite-derivative structure with spacegroup Cm is shown to be energetically stabilized under levels of tensile biaxial strains also achievable in growth experiments. Similar to PVO, both of the biaxial-strain-stabilized perovskite-derivative compounds of KVO_3 and $NaVO_3$ exhibit large electric polarizations, considerable off-centering of the B-site sublattice, and formation of vanadyl bonds. In contrast with PVO, these compounds do not form a magnetic moment at the B-site and produce signficiantly less displacement of the A-site sub-lattice. The results of this study suggest that strain-stabilized polar perovskite-derivative vanadate compounds may occur for other compositions in addition to PVO, and that changes in the A-site species can be used to tune the strength of vanadyl bonding and electronic properties in these systems. Control over these properties could be crucial to enabling ferroelectric switching and tuning the magnitudes of polar response properties.

In the remainder of this chapter, the computational methods are described in Section 5.2, and detailed descriptions of the experimentally observed crystal structures of PVO, KVO_3, and $NaVO_3$ are given in Section 5.3. The calculated epitaxial phase diagrams for KVO_3 and $NaVO_3$ are presented in Section 5.4, with associated electronic structure results discussed in Section 5.5. The main conclusions are summarized in Section 5.6.

5.2 Computational Methods

This work examines the effect of biaxial strain on the properties of perovskite-derivative structures of KVO_3 and $NaVO_3$. Here, the term perovskite-derivative structure denotes those that can be derived from the ideal 5-atom cubic perovskite unit cell by imposing biaxial strain in the (001), and allowing for tetragonal and monoclinic strains normal to this

plane, with arbitrary zone-centered displacements of the A- and B-site cations and oxygen anions. Such symmetries are meant to mimic those that would be obtained in an epitaxial thin film grown on a substrate with four-fold symmetry. Examples of such structures are described in Section 5.4 below.

5.2.1 Computational Procedure

Construction of the epitaxial phase diagrams was performed using the workflow described in Ref. [77], which involves a random structure search being conducted at each misfit strain. Specifically, for a given misfit strain, multiple candidates are initialized starting from a cubic perovskite structure and imposing random atomic displacements, leading to unit cells with $P1$ space-group symmetry. These candidate structures are subsequently structurally relaxed in DFT calculations, holding the in-plane lattice parameters constant. The lowest-energy structure resulting from these optimizations is selected at each misfit strain and used to generate a ground-state epitaxial phase diagram. A similar approach is used for the experimentally-observed 80-atom KVO_3 *Pbcm* structure. For this compound, candidate structures at each misfit strain are generated from the experimental *Pbcm* structure biaxially strained to be coherent with a four-fold substrate at a given lattice constant, and imposing random atomic displacements to again reduce the spacegroup symmetry to $P1$.

Energies of all relaxed structures are referenced to that of the compounds observed under ambient conditions, as discussed in Section 5.3. Electric polarizations are calculated for epitaxial structures at each misfit strain considered, and electronic structures are computed for the minimum energy epitaxial structures of KVO_3 and $NaVO_3$, as well as the perovskite-derivative PVO structure discussed in Section 5.3 for purposes of comparison.

5.2.2 Calculation Details

All DFT calculations made use of the Vienna *ab initio* simulation package (VASP) [60–63] version 5.4.1. A conjugate-gradient algorithm was used for all structural relaxations. As the standard VASP software package does not allow for arbitrary mechanical boundary conditions, relaxations performed under fixed in-plane strain used a custom-modified version of the VASP software in which components of the stress tensor can be fixed at zero. All relaxations of structures were continued until the forces and out-of-plane stresses converged to magnitudes within 0.001 eV/Å and 0.005 eV/f.u., respectively, where eV/f.u. is per five-atom formula unit. The resulting level of convergence in energy differences is to within 0.1 meV/f.u.

Calculations used the Ceperley-Alder form of the local density approximation (LDA) exchange-correlation functional, as parameterized by Perdew and Zunger [64], with the electron-ion interaction described by the projector augmented wave method [65, 66]. A 600 eV plane-wave cutoff energy and the tetrahedron smearing method with Blöchl corrections [68] were used. For calculations of perovskite-derivative structures based on five-atom unit cells, the Brillouin zone was sampled with a $6 \times 6 \times 6$ Monkhorst-Pack [67] grid. In

Table 5.1: Properties of the vanadate crystal structures illustrated in Fig. 5.1. The second, third and fourth columns list lattice constants, Goldschmidt tolerance factors [56], and spacegroups. The references for the data presented in this table are given in the fourth column.

Formula	a_0 (Å)	Tolerance Factor t	Spacegroup
KVO_3	3.75	1.153	$Pbcm$ [96]
$NaVO_3$	3.68	1.028	$C2/c$ [97]
$PbVO_3$	3.80	1.015	$P4mm$ [88]

calculations for the 80-atom $Pbcm$ epitaxial KVO_3 structure, a $2 \times 2 \times 6$ Monkhorst-Pack sampling was employed.

Hessian matrices were calcualed using Density Functional Perturbation Theory (DFPT) [93] at the gamma point of $2 \times 2 \times 2$ supercells. The Berry-phase approach, as described in the modern theory of polarization [24], was used to calculate the electric polarization vector of the ground-state phases at each misfit strain. All calculations assume a fixed (vanishing) external electric field corresponding to thin-films surrounded by perfectly charge-compensating electrodes, as discussed in Refs. [69, 70]. Use of the LDA in the present work leads to well-known systematic errors in the calculated lattice constants, resulting in an underestimation of their values of approximately one percent [4, 10].

Density of states calculations made use of a more refined k-point grid of $12 \times 12 \times 12$, a 600 eV plane-wave cutoff energy, and the HSE06 hybrid functional [94]. These calculations were performed on the original structures without re-optimizing the crystal structure with the hybrid functional. The HSE06 functional leads to more accurate electronic structures relative to LDA, with bandgaps agreeing to within 20% of experimentally measured values for transition-metal oxides, as discussed in Ref. [95].

5.3 Experimentally Observed Crystal Structures

Figures 5.1a and b illustrate the experimentally observed crystal structures for the KVO_3 and $NaVO_3$ compounds that form under ambient conditions [96, 97]. For comparison, Fig. 5.1c shows the structure of the PVO phase observed under high-pressure conditions [88]. Table 3.1 gives reference lattice constants, Goldschmidt tolerance factors, and spacegroups for these three structures. For KVO_3 and $NaVO_3$, all reported energies are referenced to the corresponding calculated DFT energies of the observed compounds illustrated in Figs. 5.1a and b.

The crystal structure of KVO_3 shown in Fig. 5.1a has an orthopyroxene structure with orthorhombic space group $Pbcm$, while the structure of $NaVO_3$ shown in Fig. 5.1b has the clinopyroxene structure with monoclinic space group $C2/c$ [92, 98]. Both structures are

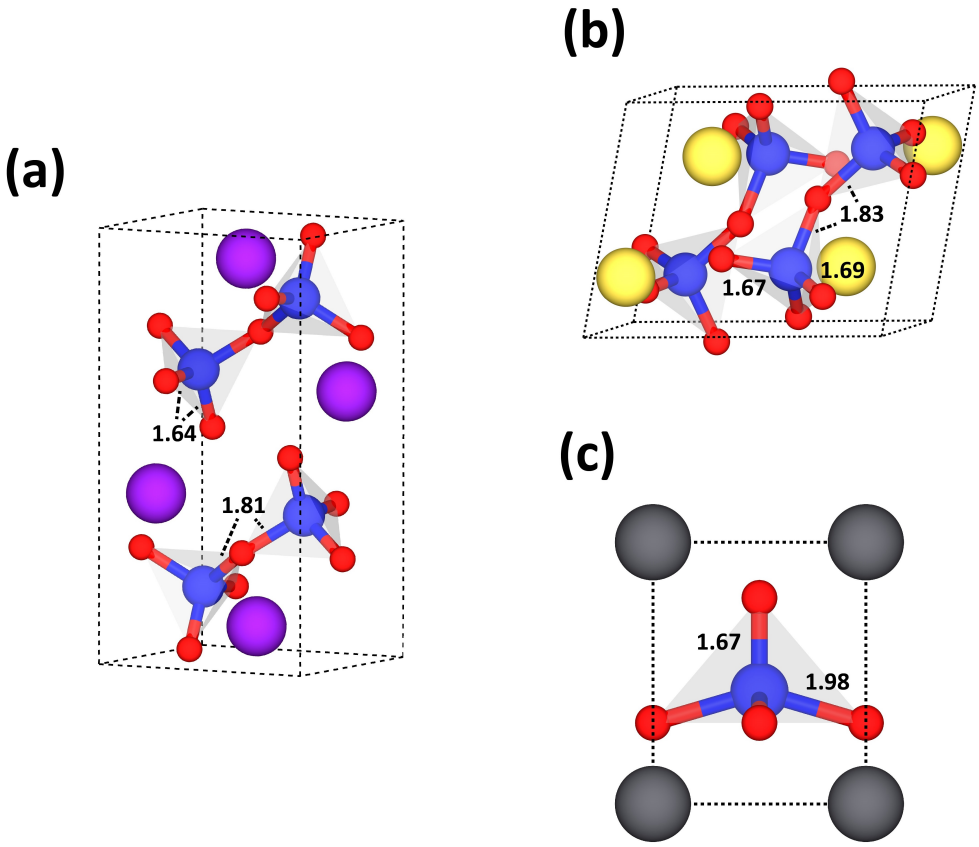

Figure 5.1: Experimentally observed crystal structures of a) KVO_3, b) $NaVO_3$, and c) PVO. Lengths of unique bonds are indicated in units of Ångstroms. References for structural data are given in the fourth column of Table 3.1. The PVO phase is observed under pressure or epitaxial strain, while the KVO and NVO phases are observed under ambient conditions. These figures were created using VESTA [55].

centrosymmetric and are characterized by long chains of tetrahedrally coordinated V^{5+} sites extending along a single direction ($^{[2+2]}V^{5+}{-}_{eq}O_{eq}{-}^{[2+2]}V^{5+}$ in the notation of Ref. [83]). The vanadium atoms have two terminating *cis* vanadyl bonds, both of length 1.64 Å for KVO_3, and of lengths 1.67 and 1.69 Å for $NaVO_3$, as well as two bridging equatorial bonds, both of length 1.81 Å for KVO_3 and 1.83 Å for $NaVO_3$. Previous experiments have demonstrated that these pyroxine structures can have strongly anisotropic mechanical responses due to their strong directional bonding along the chain directions [98].

The orthopyroxine structure of KVO_3 is potentially well-suited to epitaxial growth on a substrate with a surface displaying four-fold symmetry due to the nearly square arrangement of *A*-sites in the (100). This arrangement is illustrated in the 80-atom supercell representation shown in Fig. 5.2. From this perspective, the vanadium tetrahedra can be seen occupying the centers of slightly distorted cubes formed by *A*-sites.

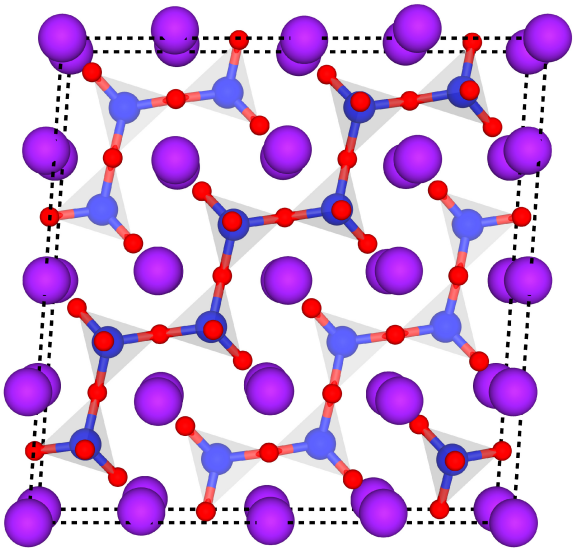

Figure 5.2: Supercell representation of *Pbcm* KVO_3 (rendered in perspective) illustrating the nearly square symmetry of the *A*-site cations in the (100) plane of the crystal structure shown in Fig. 5.1b. This figure was created using VESTA [55].

For comparison, we also consider the pressure-stabilized crystal structure of PVO as shown in Fig. 5.1c. This is similar to the strain-stabilized PVO structure obtained in thin-film growth experiments [8]. It has the non-centrosymmetric spacegroup $P4mm$, exhibits a very large tetragonality ($c/a = 1.23$), and is accompanied by significant off-centering of both the Pb and V sites [89]. These shifts result in an O_5 pyramid structure coordinating the V atom, with one apical oxygen, O(1), forming a short V-O vanadyl bond with a length of 1.67 Å. The square plane of equatorial O(2) atoms results in four equatorial V-O bonds, all of length 1.98 Å. The large downward displacement of the apical oxygen below the V site leads to a long V-O bond of 3.00 Å, resulting in a two dimensional layering of corner-shared squared pyramids rather than a three-dimensional framework of VO_6 octahedra [88]. The weak interaction between these neighboring layers is likely the reason PVO is not observed to form under ambient conditions. Due to the presence of the lone pair in Pb, the *A*-site is shifted from the center of an eightfold coordination toward a square $O(2)_2$ plane, and four of the eight Pb-O(2) distances become much shorter, with lengths of 2.39 Å. Thus, the coordination of the lead atom is a tetragonal antiprism [88]. The large displacements of the sites in PVO lead to a giant electric polarization of 1.52 C/m^2 [90].

5.4 Epitaxial Phase Diagrams

Figures 5.3a and b plot the calculated epitaxial phase diagrams for KVO_3 and $NaVO_3$, respectively. Energy is plotted versus misfit strain in the upper panel, while the values for the magnitude (dashed line) and out-of-plane (blue diamonds) and in-plane (red squares

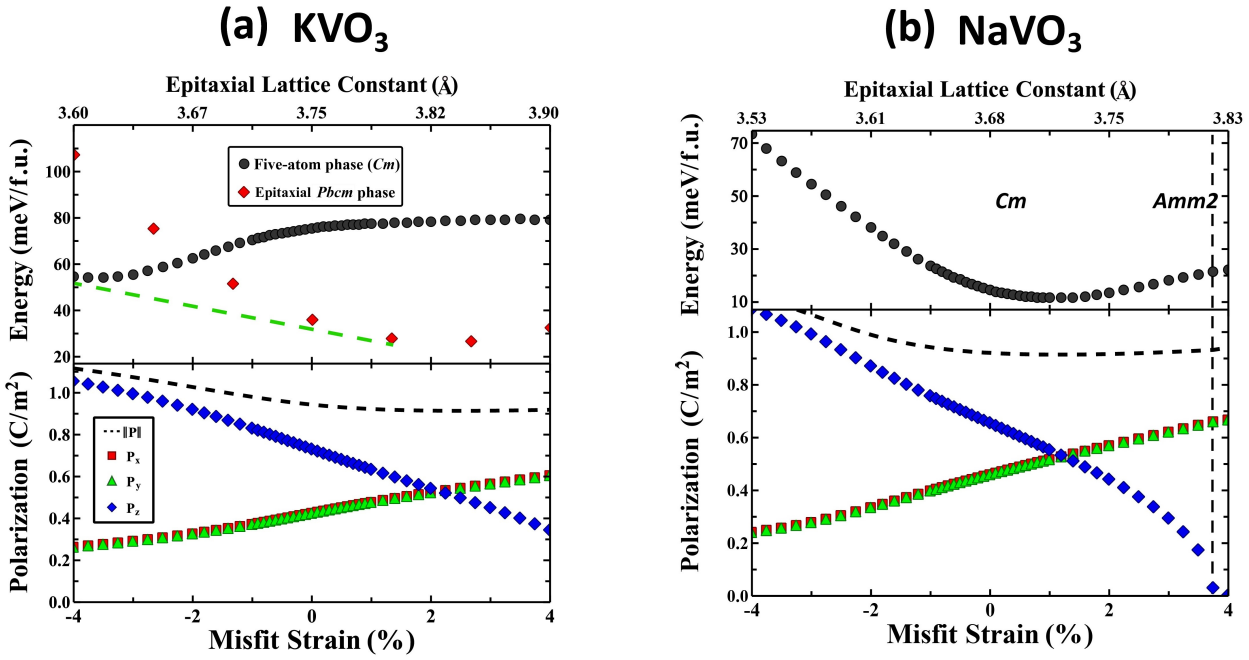

Figure 5.3: Energies and polarizations plotted against misfit strain for a) the Cm and $Pcmb$ phases of KVO_3 and b) the Cm phase of $NaVO_3$. The dashed green line in part a) indicates the common tangent construction for strain-induced phase separation. For the polarizations, out-of-plane (Pz) and in-plane (Px and Py) components, as well as the magnitudes of the total polarization vector are plotted.

and green triangles) components of the electric polarization are plotted in the bottom panel. The horizontal scale on top gives the lattice constant a of a cubic substrate corresponding to the given value of misfit: $a = a_0(\bar{\eta} + 1)$, where a_0 is the compound's reference cubic lattice constant, as listed in Table 5.1. Energies for each compound are referenced to the experimentally observed crystal structures described in Section 5.3, and can be interpreted as the strain energy of the epitaxially constrained phase, with more positive energies corresponding to larger driving forces for strain relaxation.

Figure 5.3a plots the energy and polarization versus misfit strain for two epitaxial phases of KVO_3, the perovskite-derivative Cm phase (black circles) and the strained derivative of the experimentally-observed ambient $Pbcm$ phase (red diamonds). As the $Pbcm$ phase is paraelectric at all misfit strains, only the Cm phase polarization is plotted in the bottom panel.

The energy curve of the KVO_3 Cm phase shows stabilization under large compressive misfit strains, with a minimum located at $\bar{\eta} = -3.75\%$. The corresponding ground-state perovskite-derivative structure at this misfit strain is shown in Fig. 5.4a. This structure is monoclinic ($\beta = 88.9^o$), has a very large tetragonal distortion ($c/a = 1.32$), and is 52

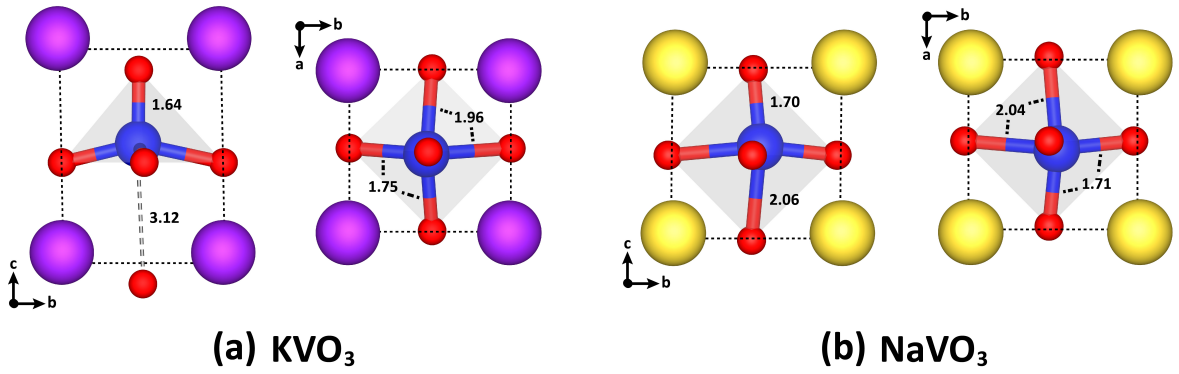

Figure 5.4: Calculated minimum-energy epitaxial structures of a) KVO_3 at $\bar{\eta} = -3.75\%$ and b) $NaVO_3$ at $\bar{\eta} = 1\%$. Bond lengths are indicated in units of Ångstroms. This figure was created using VESTA [55].

meV/f.u. higher in energy than the experimentally observed structure at ambient conditions. Vanadium forms a short vanadyl bond of length 1.64 Å with an apical oxygen, two equatorial bonds of length 1.96 Å with two surrounding oxygens in the square plane, and two equatorial bonds of length 1.75 Å with the other two oxygens in the plane. The length of the bond between vanadium and the oxygen *trans* to the vanadyl bond is 3.12 Å, leading to a layered square pyramidal arrangement similar to that seen in PVO, but with the four-fold symmetry along the c axis broken by a vanadium displacement along the $\langle 111 \rangle$. Analysis of the force-constant matrix for a $2 \times 2 \times 2$ supercell shows that this structure is stable with respect to displacement modes at the zone-center and Brillouin-zone boundaries. The softest eigen-displacement mode has an eigenvalue of 0.45 eV/Å^2, supporting the possibility that the minimum energy epitaxial KVO_3 Cm phase is stable to non-zone-centered displacement modes that can suppress polarization [16].

The polarization plot for the Cm phase of KVO_3 is shown in the bottom panel of Fig. 5.3a. This plot exhibits smoothly increasing out-of-plane polarization with increasing misfit compression, and smoothly increasing in-plane polarization with increasing misfit tension. At the energy minimum ($\bar{\eta} = -3.75\%$), the Cm phase has a polarization magnitude of almost 1.1 C/m^2, with the P_z component dominant.

Because of the ammenability of the $Pbcm$ structure of KVO_3 to (001)-oriented growth on a substrate surface with square symmetry, as described in Section 5.3, epitaxial calculations of KVO_3 were also performed on a constrained form of this structure, in which in-plane (100) shear was removed in order to simulate lattice matching with the substrate. The energy curve of the epitaxial KVO_3 $Pbcm$ phase in Fig. 5.3a has a parabolic shape centered around a minimum epitaxial lattice constant of approximately 3.82 Å. Relative to the Cm phase, the $Pbcm$ phase is stable under tensile and modest compressive epitaxial strain. However, at nearly -2% misfit strain, there is a crossing of the energy curves, and the Cm phase is predicted to be stable. A common tangent line can be constructed (dashed green line) between the energy curves of the Cm and $Pbcm$ phases, which predicts a strain-induced phase

coexistence [73] between structures with misfit strains of approximately -4% and 1.5%. This result implies that epitaxial films grown in this range of substrate lattice constants would form two phases, a non-polar tetrahedrally coordinated *Pbcm* phase with an in-plane lattice constant of around 3.80 Å, and a polar square-planar-coordinated *Cm* phase with an in-plane lattice constant of around 3.60 Å. The polar properties of such two-phase films could be of technological interest, as an out-of-plane electric field could drive growth of one or the other phase and potentially elicit a large dielectric response by altering the balance of the phase competition.

The explicit presence of a substrate, not accounted for in the present model, could shift the two energy curves shown in Fig. 5.3a. However, it is likely that the effect of a square substrate would be to further stabilize the *Cm* phase relative to *Pbcm*. This is because, in the above calculations, the *Cm* phase has an exactly square arrangement of *A* sites, while the *Pbcm* phase contains only a nearly square arrangement of *A* sites. The lack of perfect registry for the other atoms in the plane would be expected to increase the interfacial energy.

Figure 5.3b plots the energy and polarization versus misfit strain for $NaVO_3$. Due to the absence of known competing polymorphs suitable for (001) epitaxy, only predictions for a five-atom perovskite-derivative structure are shown. Under large tensile strains, an *Amm*2 phase is stable, while at all other misfit strains considered, a *Cm* phase is predicted. $NaVO_3$ under epitaxy is destabilized by compressive epitaxial strains, and stabilized at modest tensile strains, with a minimum energy structure located at $\bar{\eta} = 1\%$. The structure corresponding to this energy minimum is shown in Fig. 5.4b. It is characterized by a monoclinic angle of $\beta = 89.4^o$, $c/a = 1.01$, and it is only 9 meV/f.u. higher in energy than the experimentally observed polymorph at ambient conditions. All oxygen sites are nearly equivalent, each having a short bond with V of around 1.71 Å and a longer bond with V of 2.04 Å. The structure is approximately cubic, with the V atom shifted along the $\langle 111 \rangle$ direction to sit preferentially closer to three of the six coordinating oxygen sites. An analysis of the force-constant matrix for a $2 \times 2 \times 2$ supercell shows that this structure is unstable with respect to both in-phase and out-of-phase octahedral rotational modes at the brillouin-zone boundaries, with the most unstable eigen-displacement mode having an eigenvalue of -0.93 eV/Å^2. In a thicker film, where these modes are not frozen out due to the constraint of epitaxy, the effect on polarization could be sizeable [99].

Similar to behavior seen for the KVO_3 *Cm* phase, the out-of-plane polarization for epitaxial $NaVO_3$ smoothly decreases while in-plane polarization smoothly increases with increasing misfit strain. The out-of-plane polarization eventually disappears at the phase boundary located at $\bar{\eta} = 3.75\%$. The polarization of the minimum energy structure in $NaVO_3$ has a magnitude of 0.92 C/m^2, with nearly equal contributions from in-plane and out-of-plane components.

5.5 Electronic Structures

Figures 5.5a-c show the total and projected electronic density of states (DOS) for the PVO, KVO_3, and $NaVO_3$ structures illustrated in Figs. 5.1c, 5.4a, and 5.4b, respectively calculated by the HSE06 hybrid functional. The top panel (black line) of each figure plots the total DOS, while the other three panels plot the DOS projected onto the s, p, and d orbitals of the various sites. Projected DOS are included for the A-cation (red line, A = Pb, K, or Na), vanadium (blue), apical oxygen (light green), and two symmetry-equivalent equatorial oxygen sites (dark green). A comparison of the electronic structures of these three systems leads to key insights into the role of the A-site species in the bonding, as well as the effect of changing the vanadium oxidation state from V^{4+}, as in PVO, to V^{5+}, as in KVO_3 and $NaVO_3$.

Figure 5.5a plots the DOS for the PVO structure shown in Fig. 5.1c. The electronic structure of PVO has been calculated previously [84, 88, 89] using semi-local DFT, while the present work employs hybrid functionals. In prior work a C-type antiferromagnetic ordering of the magnetic moments has been shown to be slightly lower in energy than a ferromagnetic (FM) ordering [88]. In the present work, which is focused on exploring trends across the different vanadate compounds, we have considered only the FM state, which yields a magnetic moment of 1 μ_B/f.u., localized on the Pb ion.

In order of increasing energy, the DOS for PVO in Fig. 5.5a exhibits a separate Pb-6s peak starting 9 eV below the Fermi energy, followed by states of dominant O-2p character. At the valence band maximum, the DOS shows a small peak originating from spin-up V-3d states. The states at the conduction band minimum are of dominant V-3d character, followed by a manifold of low-lying Pb-6p states. The DOS indicates Mott-insulator character, with the 2.35 eV band gap determined by the splitting between occupied and unoccupied V-3d states. A single electron occupies the majority-spin vanadium d_{xy} state (blue, -1 to 0 eV), resulting in vanadium having a V^{4+} (d^1) configuration in an ionic picture. In a centrosymmetric tetragonal crystal field, the d_{yz} and d_{xz} orbitals are normally lower in energy than the d_{xy} orbital, *e.g.*, as is seen in $PbTiO_3$ [89]. However, the crystal field in PVO can be thought of as being composed of an octahedral crystal field that splits the five d orbitals into three lower-lying t_{2g} states and two higher-lying e_g states. The non-centrosymmetric displacements in the structure further split the e_g states into two and the t_{2g} states into a lower-lying d_{xy} non-bonding state and higher-lying two-fold degenerate d_{xz} and d_{yz} states [84]. This picture accounts for the multipeak electronic structure seen in the d-orbital partial DOS in the bottom panel of Fig. 5.5a.

The stereochemically-active Pb site plays an important role in the bonding and electronic structure of PVO. Both the Pb-O and V-O bonds display covalent character, and are strongly coupled. As shown in Fig. 5.5a, the Pb-6s states in the valence band and low-lying Pb-6p states in the conduction band mix with O-2p states. These same O-2p states also display hybridization with V-3d states, thus suggesting the possibility for competition between vanadyl and Pb-O bonds. As pointed out in Ref. [84], the stereochemical activity of Pb is not just

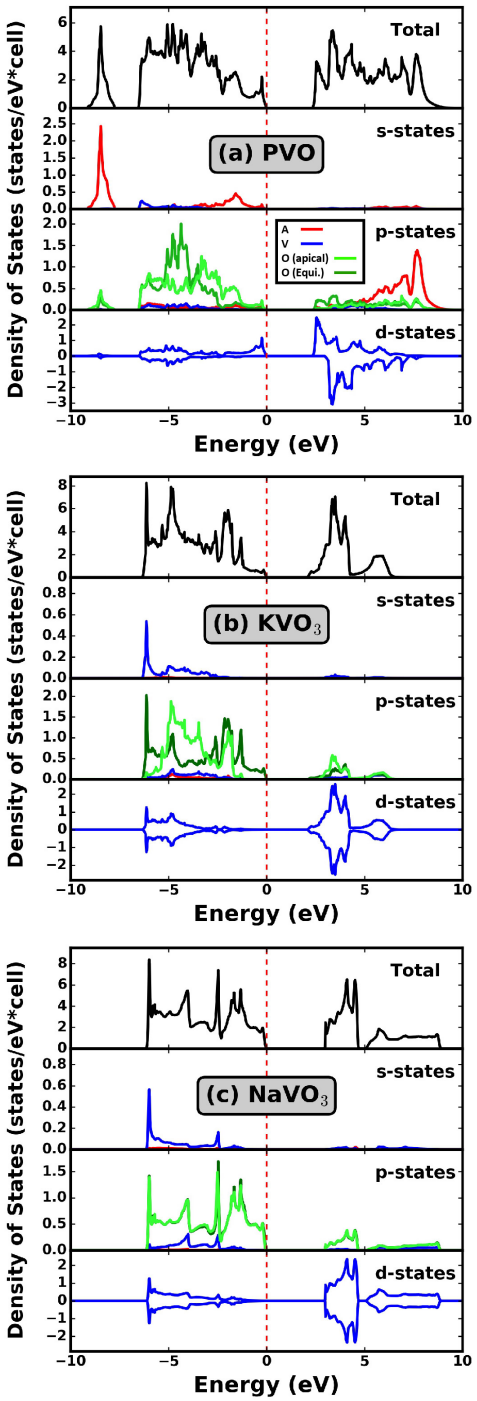

Figure 5.5: Total and projected density of states for a) PVO (Fig. 5.1c), b) KVO_3 (Fig. 5.4a), and c) $NaVO_3$ (Fig. 5.4b). Black lines indicate values of the total DOS, while colored lines give values of the Projected DOS, with values of the *A*-cation in red, vanadium in blue, the apical oxygen in light green, and the two symmetry-equivalent equatorial oxygens in dark green. For *d*-states, spin-up and spin-down states are denoted by positive and negative values.

a result of the lone 6s pair, but also results from the atomic structure of Pb^{2+}, which has low-lying 6p states that are very spatially extended and are able to hybridize with occupied ligand orbitals. As a result of this competition, the vanadyl bond in PVO is relatively weak, as evidenced by a relatively long bond length compared to most other vanadyl bonds in minerals.

Figures 5.5b and c show DOS plots for the minimum energy epitaxial phases (see Fig. 5.4) of KVO_3 and $NaVO_3$, respectively. Both are charge-transfer insulators with the states at the valence-band maximum being largely of O-2p character. The HSE06 bandgaps of KVO_3 and $NaVO_3$ are 2.07 eV and 2.98 eV, respectively. The ground state is non-spin-polarized in both structures. Both in the valence and conduction bands, the V-3d states of KVO_3 and $NaVO_3$ strongly mix with O-2p states, indicating strong covalent character. In general, the strong tetragonal distortion of KVO_3 results in distinct electronic behaviors for the apical versus the equitorial O sites, whereas the almost cubic lattice in $NaVO_3$ leads to nearly identical behaviors between all of the O sites. Unlike with PVO, no A-site states appear near the Fermi energy. At approximately 6.5 eV below the Fermi energy, both systems exhibit a sharp peak of states with mixed V-4s, O-2p, and V-3d character. In the case of KVO_3, the equitorial O-2p states are mixing with largely V-s and V-3$d_{x^2-y^2}$ states, while in $NaVO_3$, both the apical and equitorial O states mix with V-4s and equal parts V-3d_{z^2} and V-3$d_{x^2-y^2}$ states. The states above approximately -5 eV are largely of V-3d_{xz} and V-3d_{yz} character for KVO_3 and equal parts V-3d_{xz}, V-3d_{yz}, and V-3d_{xy} for $NaVO_3$. The apical O in KVO_3 mixes more strongly with these states in a second peak. The states at the valence band maximum are of dominant O-2p character in both compounds, and those at the valence-band minimum are of primarily V-3d character.

A key result of the calculations shown in Fig. 5 is that the strength of the vanadyl bond is affected by replacing the Pb A-site cation with Na or K. Singh shows in Ref. [84] that, although replacement of Pb^{2+} with Ca^{2+} should strengthen the vanadyl bond by removing the Pb-O ineraction that competes with the V-O interaction, the replacement of Pb instead broadens the t_{2g} bands and alters the crystal field so that the vanadyl bond is no longer stabilized. In this work, however, it is seen that substitution of Pb^{2+} with K^{1+} or Na^{1+} does not alter the crystal field such as to destabilize the vanadyl bond. Further, because the monovalent alkali metal A-sites do not have the spatially extended 6p states needed to bond covalently with oxygen, they do not compete with the V-O interactions. The result is stronger mixing between V and O states in KVO_3 and $NaVO_3$, which is consistent with the shorter average V-O bond lengths of these two systems as compared to those of PVO.

5.6 Summary

The ground-state epitaxial phases and energetic, polar, and electronic properties of two alkali-metal vanadates, KVO_3 and $NaVO_3$, are studied computationally by DFT calculations. Both KVO_3 and $NaVO_3$ exhibit epitaxially stabilized perovskite-derivative phases with vanadyl bonding, large polarizations, and low epitaxial strain energies. The predicted

ground-state epitaxial phase diagram for KVO_3 shows potential for strain-induced phase separation between a structure with Cm symmetry having a large polarization and square pyramidal coordination of the B-site, and a non-polar epitaxial $Pbcm$ structure displaying tetrahedral coordination of the B-site. The electronic structure of the epitaxial phases of KVO3 and NaVO3 are calculated and compared with those of the experimentally observed perovskite-derivative PVO compound. These calculations show that substitution of Pb^{2+} with K^{1+} or Na^{1+} increases the strength of the vanadyl bond, due to the removal of the spatially extended Pb $6p$ states that compete with V-O bonding.

CHAPTER 6

Summary and Future Work

The design and discovery of new ferroelectric thin-film systems is greatly facilitated by improved first-principles modeling capabilities, as the properties of these systems are sensitive to a relatively large number of degrees of freedom as compared to traditional bulk ferrelectrics. The research presented here has outlined and applied various automated first-principles computational approaches for efficiently and systematically exploring the complex parameter space of thin film ferroelectrics. The remainder of this chapter provides a summary of the key results given in chapters 3, 4, and 5. In the final section, potential directions for future work are given, with a discussion of how this work could further develop understanding of thin-film ferroelectrics.

6.1 Orientation-Dependent Properties of Perovskite Oxide Thin Films

In chapter 3, an automated DFT computational approach is used to investigate the effects of epitaxial misfit strain on the structure, polarization, and energetic behavior of many common perovskite compounds. Boundary conditions are included not only for the (100)-growth orientation, but also for the (110)- and (111)-orientations, allowing for study of the dependence of thin-film properties on growth orientation. The approach in this work considered only perovskite-based structures, *i.e.*, structures consistent with a periodicities of a 5-atom perovskite primitive cell. Although this precludes examining the effects of common distortions, such as rotations of the BO_6 octahedra, it also gives unique insight in the case of sufficiently thin-films in which such distortions are effectively frozen out.

Key results of chapter 3 include robust trends of in-plane polarization enhancement under tension for all three growth orientations, and out-of-plane polarization enhancement under biaxial compression for the (100)- and (110)-oriented film systems. For (111)-oriented growth, a wider variety of out-of-plane polarization behaviors is predicted, the most extreme example being (111)-$BaTiO_3$, which exhibits an anomalously diminishing out-of-plane polarization with compression. This dependence of polarization enhancement on growth

orientations is a clear example of the subtle dependencies of thin-film properties on epitaxial boundary conditions. Other trends discovered include clear tendencies for compounds with different compositions to form behavior groups, characterized by their phase sequences and polarizations versus misfit strain. Two (100)-oriented systems, $SrHfO_3$ and $NaTaO_3$, exhibit unique polarization dependencies on misfit strain, having phase transitions near 0% misfit strain whereby a phase with all out-of-plane polarization gives way to a phase with all in-plane polarization. The three (100)-oriented systems showing strain-induced phase coexistence, $PbTiO_3$, $NaNbO_3$, and $NaVO_3$, have relatively soft biaxial elastic responses compared to the other compounds where this phenomenon is absent, suggesting that softness of the in-plane biaxial elastic response is an important factor in predicting whether or not strain-induced phase coexistence will occur in a film.

With respect to technological applications, the key takeaway from the work in chapter 3 is that the (110)- and (111)-oriented films more commonly feature first-order phase transitions as a function of misfit strain, relative to the (100)-oriented case. An example is given for (111)-oriented $NaVO_3$, which has a first-order phase transition at small misfit tension with a very large shift in polarization direction. Sudden changes in polarization state are often useful for device applications, making the much-less-explored realm of (110)- and (111)-oriented films a potentially fruitful domain for materials discovery.

6.2 Epitaxial Phase Diagrams Including the Role of Antiferrodistortive and *A*-Site Displacement Modes

Chapter 4 presents a more comprehensive computational framework for the calculation of ground-state epitaxial phase diagrams of ferroelectric perovskite oxides. This approach includes the effects of AFD and *A*-site displacement modes that are commonly observed in perovskite compounds. Ground-state epitaxial phases are identified using a series of total-energy expansions at various misfit strains with respect to soft-mode displacements and homogeneous deformations. These expansions are minimized in order to locate candidate ground-state structures, which are further optimized through DFT calculations. The key feature of this method is the lack of need for input information from experimental measurements. This computational approach is demonstrated in chapter 4 in an application to three perovskite oxides, $SrTiO_3$, $CaTiO_3$, and $SrHfO_3$, over a range of epitaxial strains applied parallel to the (001) plane.

The results of this work show that a set of nine displacement modes, three zone-centered FE distortions often transforming like Γ_4^-, and six AFD octahedral rotations, three transforming like R_4^+ and three like M_3^+, comprise the largest contributors to the atomic displacements found in the calculated ground-state structures across all of the compositions and misfit strains considered. Further, even when competing eigenmodes have more ustable eigenvalues, combinations of these nine modes dominate atomic displacements in stable epi-

taxial phases. This work also shows the important role of A-site bonding preferences in these perovskite compounds. While the atomic displacements of $SrTiO_3$ can almost entirely be decomposed into contributions from these nine dominant displacement modes, those obtained for $CaTiO_3$ and $SrHfO_3$ also contain significant contributions from additional predominantly A-site displacement modes. These modes largely constitute antipolar A-site shifts that significantly lower strain energies of the epitaxial phases by optimizing the coordination geometry of the A-site cation. The amplitude of displacements in the A-site lattice is very sensitive to the degree of misfit strain.

Because the model presented in chapter 4 includes non-zone-centered displacement modes, while the model in chapter 3 is restricted to only treating zone-centered modes, a unique opportunity arises to isolate the effects of an important subset of distortions in perovskite thin films. The results show that the inclusion of non-zone-centered displacement modes significantly affects the dependence of energy and polarization on misfit strain. Specifically, the AFD octahedral rotations and A-site displacement modes tend to strongly suppress polarization and reduce the epitaxial strain energy. This comparison gives important insights for practical thin-film applications with regard to the stability of competing phases as a function of film thickness. Non-zone-centered distortions can be frozen out in very thin films if they increase interfacial energy with the underlying substrate lattice, while these distortions are likely to appear in thicker films because they reduce strain energy. Thus, one of multiple competing phases with very different polar properties can be preferentially selected by tuning film thickness.

6.3 Electronic and Polar Properties of Vanadate Thin-Films

Chapter 5 focuses on the discovery of new vanadate perovskite thin-film ferroelectrics alternative to the commonly studied PVO system. The workflow that was outlined in chapter 3 is applied to two alkali-metal vanadates, KVO_3 and $NaVO_3$, in order to determine the effect of epitaxial boundary conditions on their energetic and polar properties. This work finds that both KVO_3 and $NaVO_3$ exhibit epitaxially stabilized perovskite-based phases with vanadyl bonding, large polarizations, and low film strain energy. Further, the predicted phase diagram for KVO_3 shows potential for strain-induced phase separation between a 5-atom Cm phase having a large polarization and square pyramidal coordination of the B-site, and a non-polar epitaxial $Pbcm$ phase having tetrahedral coordination of the B-site. This region of phase separation could be interesting from an applied perspective, as application of an electric field can foster growth of one or the other phase, potentially eliciting a large dielectric response. The electronic structure of PVO is calculated and compared with those of KVO_3 and $NaVO_3$, showing that substituting Pb^{2+} with K^{1+} or Na^{1+} increases the strength of the vanadyl bond, due to the removal of the spatially extended Pb $6p$ states that compete with V-O bonding. This increased strength in bonding between V and O could result in a

system that is even more difficult to ferroelectrically switch than PVO, although the barriers to switching depend on factors influencing domain nucleation and growth, which are not considered in this work.

6.4 Future Work

The results outlined in chapters 3-5 point to many opportunities for additional work that could further improve understanding of thin-film ferroelectrics and facilitate their design and discovery. The workflow discussed in chapter 3 was applied to 42 non-magnetic oxide perovskite systems having B-cations with d^0 formal valence. There exist many other perovskite systems of technological interest, and the consideration of this broader set of systems with non-d^0 B-cations having spin-polarized ground states is a natural extension of this work. This extension would require the more complex task of considering degrees of freedom associated with the ordering of the magnetic moments of the B-cation when searching for the ground-state. The simplest approach would be to allow only magnetic states consistent with the five-atom periodicity of the perovskite primitive cell (ferromagnetism), while more complicated approaches considering antiferromagnetism could be enabled by using larger supercells.

The approach discussed in chapter 4 was applied to only three specific systems for the purpose of demonstrating its effectiveness. This approach could easily be applied to a broader range of compositions. This would allow for trends to be ascertained with respect to more complex distortion modes than those considered in chapter 3. Further, the three systems considered, $SrTiO_3$, $CaTiO_3$, and $SrHfO_3$, all have tolerance factors at or below one. Extending this workflow to perovskite compounds with tolerance factors greater than one would lead to a greater diversity of ground-state phases and a deeper understanding of the dominant displacement modes for perovskite in which the B-cation is relatively too small.

As discussed in chapter 5, although PVO has a giant electrical polarization, it is a difficult system to switch with application of an electric field. Thus, one of the motivations for searching for alternative vanadate perovskites was to discover systems with similarly large spontaneous polarizations that have lower barriers to switching. Insight into the barriers of the ground-state epitaxial phases of KVO_3 and $NaVO_3$ would provide knowledge of whether these systems could be useful for applications requiring ferroelectric switching. However, because switching in ferroelectrics is dependent on processes with relatively large length scales, such as domain nucleation, predicting the true energy barriers will require multi-scale approaches, such as the use of force-field models in large-scale molecular dynamics simulations, or phase-field models that can be parametrized from DFT results.

The calculations described in this dissertation have been limited to determining the energies and properties of the homogeneous phases of ferroelectric thin films, as DFT is constrained in the size of system it can consider. Although the direct modeling of domain structures in thin-film ferroelectrics goes well beyond the present capabilities of DFT calculations, the DFT calculations and workflows presented in this work can be used to guide

the development of other methods that can handle these larger length scales. For example, first-principles DFT calculations could be used to develop potentials for use in molecular dynamics simulations, which have been applied to studying domain-wall motion in ferroelectrics (*e.g.*, [100]), or to study pyroelectricity in $LiNbO_3$ using shell-model potentials [101]. This approach would enable incorporation of temperature effects, determination of the preferred types of domain walls in a given ferroelectric, and would give access to a variety of other equilibrium properties and a deeper understanding of the kinetic mechanisms underlying switching.

References

[1] J. F. Scott, "Applications of modern ferroelectrics," *Science*, vol. 315, pp. 954–959, 2007.

[2] D. G. Schlom, L. Q. Chen, C. B. Eom, K. M. Rabe, S. K. Streiffer, and J. M. Triscone, "Strain Tuning of Ferroelectric Thin Films," *Annu. Rev. Mater. Res.*, pp. 589–626.

[3] D. L. Smith and D. W. Hoffman, *Thin-Film Deposition: Principles and Practice*. Boston: McGraw-Hill, 1995.

[4] M. Dawber, K. M. Rabe, and J. F. Scott, "Physics of thin-film ferroelectric oxides," *Rev. Mod. Phys.*, vol. 77, no. 4, pp. 1083–1130, 2005.

[5] S. Baoyuan, W. Jiantong, Z. Jun, and Q. Min, "A new model describing physical effects in crystals: The diagrammatic and analytic methods for macro-phenomenological theory," *Journal of Materials Processing Technology*, vol. 139, pp. 444–447, 2003.

[6] A. R. Damodaran and L. W. Martin, "Strain-induced Domain Structure Coexistence and Giant Electromechanical Responses in PbTiO3," *Nat. Mater.*, submitted.

[7] J. H. Haeni, P. Irvin, W. Chang, R. Uecker, P. Reiche, Y. L. Li, S. Choudhury, W. Tian, M. E. Hawley, B. Craigo, a. K. Tagantsev, X. Q. Pan, S. K. Streiffer, L. Q. Chen, S. W. Kirchoefer, J. Levy, and D. G. Schlom, "Room-temperature ferroelectricity in strained SrTiO3.," *Nature*, vol. 430, no. August, pp. 758–761, 2004.

[8] L. W. Martin, Q. Zhan, Y. Suzuki, R. Ramesh, M. Chi, N. Browning, T. Mizoguchi, and J. Kreisel, "Growth and structure of PbVO3 thin films," *Appl. Phys. Lett.*, vol. 90, p. 062903, 2007.

[9] R. D. King-Smith and D. Vanderbilt, "First-principles investigation of ferroelectricity in perovskite compounds," *Phys. Rev. B*, vol. 49, no. 9, pp. 5828–5844, 1994.

[10] O. Diéguez, K. M. Rabe, and D. Vanderbilt, "First-principles study of epitaxial strain in perovskites," *Phys. Rev. B*, vol. 72, no. 14, p. 144101, 2005.

[11] O. Diéguez, S. Tinte, A. Antons, C. Bungaro, J. B. Neaton, K. M. Rabe, and D. Vanderbilt, "Ab Initio study of the phase diagram of epitaxial BaTiO 3," *Phys. Rev. B*, vol. 69, no. 21, p. 212101, 2004.

[12] J. B. Neaton, C. L. Hsueh, and K. M. Rabe, "Enhanced polarization in strained BaTiO 3 from first principles," in *MRS Proceedings*, vol. 718, 2002.

[13] A. Antons, J. B. Neaton, K. M. Rabe, and D. Vanderbilt, "Tunability of the dielectric response of epitaxially strained SrTiO 3 from first principles," *Phys. Rev. B*, vol. 71, no. 2, p. 024102, 2005.

[14] K. M. Rabe, "Theoretical investigations of epitaxial strain effects in ferroelectric oxide thin films and superlattices," *Curr. Opin. Solid State Mater. Sci.*, vol. 9, no. 3, pp. 122–127, 2005.

[15] O. Diéguez and D. Vanderbilt, "First-principles modeling of strain in perovskite ferroelectric thin films," *Phase Transitions*, vol. 81, no. 7-8, pp. 607–622, 2008.

[16] N. A. Benedek and C. J. Fennie, "Why are there so few perovskite ferroelectrics?," *J. Phys. Chem. C*, vol. 117, no. 26, pp. 13339–13349, 2013.

[17] R. Custodio and N. H. Morgon, "The Density-Functional Theory," 1995.

[18] A. J. Freeman and E. Wimmer, "Density Functional Theory as a Major Tool in Computational Materials Science," *Annual Review of Materials Science*, vol. 25, pp. 7–36, 1995.

[19] A. Jain, Y. Shin, and K. A. Persson, "Computational predictions of energy materials using density functional theory," *Nature Reviews Materials*, vol. 1, p. 15004, 2016.

[20] Y. Zhang, J. Sun, J. P. Perdew, and X. Wu *Phys. Rev. B*, vol. 96, p. 035143, 2017.

[21] D. I. Bilc, R. Orlando, R. Shaltaf, G. M. Rignanese, J. Íñiguez, and P. Ghosez, "Hybrid exchange-correlation functional for accurate prediction of the electronic and structural properties of ferroelectric oxides," *Phys. Rev. B*, vol. 77, no. 16, p. 165107, 2008.

[22] S. Baroni, S. De Gironcoli, A. Dal Corso, and P. Giannozzi, "Phonons and related crystal properties from density-functional perturbation theory," *Rev. Mod. Phy.*, vol. 73, no. 2, pp. 515–562, 2001.

[23] N. A. Spaldin, "A beginner's guide to the modern theory of polarization," *Journal of Solid State Chemistry*, vol. 195, pp. 2–10, 2012.

[24] R. Resta and D. Vanderbilt, "Theory of polarization: A modern approach," *Top. Appl. Phys.*, vol. 105, no. Cm, pp. 31–68, 2007.

[25] S. P. Ong, W. D. Richards, A. Jain, G. Hautier, M. Kocher, S. Cholia, D. Gunter, V. L. Chevrier, K. A. Persson, and G. Ceder, "Python Materials Genomics (pymatgen): A robust, open-source python library for materials analysis," *Computational Materials Science*, vol. 68, pp. 314–319, 2013.

[26] S. P. Ong, A. Jain, G. Hautier, K. A. Persson, and G. Ceder

[27] M. de Jong, W. Chen, H. Geerlings, M. Asta, and K. A. Persson, "A database to enable discovery and design of piezoelectric materials," *Scientific Data*, vol. 2, p. 150053, 2015.

[28] M. de Jong, W. Chen, T. Angsten, A. Jain, R. Notestine, A. Gamst, M. Sluiter, C. Krishna Ande, S. van der Zwaag, J. J. Plata, C. Toher, S. Curtarolo, G. Ceder, K. A. Persson, and M. Asta, "Charting the complete elastic properties of inorganic crystalline compounds," *Scientific Data*, vol. 2, pp. 1–13, 2015.

[29] Cross, L. E., and Newnham, R. E., "History of ferroelectrics," in *Ceramics and Civilization*, vol. III, pp. 289–305, Westerville, OH: American Ceramic Society, 1987.

[30] Jaffe, Bernard, and Cook, William R., and Jaffe, Hans Ludwig, *Piezoelectric ceramics*. New York: Academic Press, 1971.

[31] A. R. Damodaran, J. C. Agar, S. Pandya, Z. Chen, L. Dedon, R. Xu, B. Apgar, S. Saremi, and L. W. Martin, "New modalities of strain-control of ferroelectric thin films," *J. Phys. Condens. Matter*, vol. 28, p. 263001, 2016.

[32] L. W. Martin, Y. H. Chu, and R. Ramesh, "Advances in the growth and characterization of magnetic, ferroelectric, and multiferroic oxide thin films," *Mater. Sci. Eng. R-Rep.*, vol. 68, no. 4-6, pp. 89–133, 2010.

[33] D. G. Schlom, L. Q. Chen, X. Pan, A. Schmehl, and M. A. Zurbuchen, "A thin film approach to engineering functionality into oxides," *J. Am. Ceram. Soc.*, vol. 91, no. 8, pp. 2429–2454, 2008.

[34] K. Sone, H. Naganuma, T. Miyazaki, T. Nakajima, and S. Okamura, "Crystal structures and electrical properties of epitaxial BiFeO3 thin films with (001), (110), and (111) orientations," *Jpn. J. Appl. Phys.*, vol. 49, no. 9 PART 2, p. 09MB03, 2010.

[35] R. Xu, S. Liu, I. Grinberg, J. Karthik, A. R. Damodaran, A. M. Rappe, and L. W. Martin, "Ferroelectric polarization reversal via successive ferroelastic transitions.," *Nat. Mater.*, vol. 14, no. 1, pp. 79–86, 2015.

[36] W. K. Simon, E. K. Akdogan, and A. Safari, "Anisotropic strain relaxation in (ba0.6sr0.4)tio3 epitaxial thin films," *J. Appl. Phys.*, vol. 97, no. 10, 2005.

[37] A. K. Tagantsev, N. A. Pertsev, P. Muralt, and N. Setter, "Strain-induced diffuse dielectric anomaly and critical point in perovskite ferroelectric thin films," *Phys. Rev. B*, vol. 65, no. 1, p. 012104, 2001.

[38] H. Wu, X. Ma, Z. Zhang, J. Zeng, J. Wang, and G. Chai, "Effect of crystal orientation on the phase diagrams, dielectric and piezoelectric properties of epitaxial BaTiO3 thin films," *AIP Adv.*, vol. 6, no. 1, p. 015309, 2016.

[39] J. C. Agar, S. Pandya, R. Xu, A. K. Yadav, Z. Liu, T. Angsten, S. Saremi, M. Asta, R. Ramesh, and L. W. Martin, "Frontiers in strain-engineered multifunctional ferroic materials," *MRS Commun.*, vol. 6, pp. 151–166, Aug 2016.

[40] J. Schwarzkopf and R. Fornari, "Epitaxial growth of ferroelectric oxide films," *Prog. Cryst. Growth Charact. Mater.*, vol. 52, no. 3, pp. 159–212, 2006.

[41] H. Béa, B. Dupé, S. Fusil, R. Mattana, E. Jacquet, B. Warot-Fonrose, F. Wilhelm, A. Rogalev, S. Petit, V. Cros, A. Anane, F. Petroff, K. Bouzehouane, G. Geneste, B. Dkhil, S. Lisenkov, I. Ponomareva, L. Bellaiche, M. Bibes, and A. Barthélémy, "Evidence for room-temperature multiferroicity in a compound with a giant axial ratio," *Phys. Rev. Lett.*, vol. 102, no. 21, p. 217603, 2009.

[42] S. Curtarolo, G. L. W. Hart, M. B. Nardelli, N. Mingo, S. Sanvito, and O. Levy, "The high-throughput highway to computational materials design," *Nat. Mater.*, vol. 12, no. 3, pp. 191–201, 2013.

[43] G. Ceder and K. Persson, "How Supercomputers Will Yield a Golden Age of Materials Science," *Scientific American*, vol. 309, pp. 36–40, 2013.

[44] B. Meredig, A. Agrawal, S. Kirklin, J. E. Saal, J. W. Doak, A. Thompson, K. Zhang, A. Choudhary, and C. Wolverton, "Combinatorial screening for new materials in unconstrained composition space with machine learning," *Phys. Rev. B*, vol. 89, no. 9, p. 094104, 2014.

[45] A. Jain, G. Hautier, S. P. Ong, and K. Persson, "New opportunities for materials informatics: Resources and data mining techniques for uncovering hidden relationships," *J. of Mater. Res.*, vol. 31, no. 8, pp. 977–994, 2016.

[46] A. Zakutayev, X. Zhang, A. Nagaraja, L. Yu, S. Lany, T. O. Mason, D. S. Ginley, and A. Zunger, "Theoretical prediction and experimental realization of new stable inorganic materials using the inverse design approach," *J. Amer. Chem. Soc.*, vol. 135, no. 27, pp. 10048–10054, 2013.

[47] Z. Gui, S. Prosandeev, and L. Bellaiche, "Properties of epitaxial (110) BaTiO 3 films from first principles," *Phys. Rev. B*, vol. 84, no. 21, p. 214112, 2011.

[48] A. Raeliarijaona and H. Fu, "Various evidences for the unusual polarization behaviors in epitaxially strained (111) BaTiO3," *J. Appl. Phys.*, vol. 115, no. 5, p. 054105, 2014.

[49] R. Oja, K. Johnston, J. Frantti, and R. M. Nieminen, "Computational study of (111) epitaxially strained ferroelectric perovskites BaTiO3 and PbTiO3," *Phys. Rev. B*, vol. 78, no. 111, p. 094102, 2008.

[50] A. Togo and I. Tanaka, "First principles phonon calculations in materials science," *Scripta Mater.*, vol. 108, pp. 1–5, 2015.

[51] J. Hutter, "Carparrinello molecular dynamics," *Wiley Interdisciplinary Reviews: Computational Molecular Science*, vol. 2, pp. 604–612, 7 2012.

[52] C. J. Pickard and R. J. Needs, "Ab initio random structure searching.," *J. Phys.: Condens. Matter*, vol. 23, no. 5, p. 053201, 2011.

[53] C. W. Glass, A. R. Oganov, and N. Hansen, "USPEX-Evolutionary crystal structure prediction," *Comp. Phys. Commun.*, vol. 175, no. 11-12, pp. 713–720, 2006.

[54] Y. Wang, J. Lv, L. Zhu, and Y. Ma, "CALYPSO: A method for crystal structure prediction," *Comp. Phys. Commun.*, vol. 183, no. 10, pp. 2063–2070, 2012.

[55] K. Momma and F. Izumi *J. Appl. Crystallogr.*, vol. 44, pp. 1272–1276, Dec 2011.

[56] V. M. Goldschmidt, "Die Gesetze der Krystallochemie," *Die Naturwissenschaften*, vol. 14, no. 21, pp. 477–485, 1926.

[57] I. D. Brown, "Bond valences?a simple structural model for inorganic chemistry," *Chem. Soc. Rev.*, vol. 7, no. 3, p. 359, 1978.

[58] www.me.utexas.edu/˜benedekgroup/ToleranceFactorCalculator.

[59] K. M. Rabe, M. Dawber, C. Lichtensteiger, C. H. Ahn, and J. M. Triscone, "Modern physics of ferroelectrics: Essential background," *Top. Appl. Phys.*, vol. 105, no. 2007, pp. 1–30, 2007.

[60] G. Kresse and J. Hafner, "Ab initio molecular dynamics for liquid metals," *Phys. Rev. B*, vol. 47, no. 1, pp. 558–561, 1993.

[61] G. Kresse and J. Hafner, "Ab initio molecular-dynamics simulation of the liquid-metalamorphous-semiconductor transition in germanium," *Phys. Rev. B*, vol. 49, no. 20, pp. 14251–14269, 1994.

[62] G. Kresse and J. Furthmüller, "Efficient iterative schemes for ab initio total-energy calculations using a plane-wave basis set," *Phys. Rev. B*, vol. 54, no. 16, pp. 11169–11186, 1996.

[63] G. Kresse and J. Furthmüller, "Efficiency of ab-initio total energy calculations for metals and semiconductors using a plane-wave basis set," *Computational Materials Science*, vol. 6, no. 1, pp. 15–50, 1996.

[64] J. P. Perdew and A. Zunger, "Self-interaction correction to density-functional approximations for many-electron systems," *Phys. Rev. B*, vol. 23, no. 10, pp. 5048–5079, 1981.

[65] P. E. Blöchl, "Projector augmented-wave method," *Phys. Rev. B*, vol. 50, no. 24, pp. 17953–17979, 1994.

[66] G. Kresse and D. Joubert, "From Ultrasoft Pseudopotentials to the Projector Augmented Wave Method," *Phys. Rev. B*, vol. 59, no. 3, pp. 1758–1775, 1999.

[67] H. Monkhorst and J. Pack, "Special points for Brillouin zone integrations," *Phys. Rev. B*, vol. 13, no. 12, pp. 5188–5192, 1976.

[68] P. E. Blöchl, O. Jepsen, and O. K. Andersen, "Improved tetrahedron method for Brillouin-zone integrations," *Phys. Rev. B*, vol. 49, no. 23, pp. 16223–16233, 1994.

[69] A. M. Kolpak, N. Sai, and A. M. Rappe, "Short-circuit boundary conditions in ferroelectric thin films," *Phys. Rev. B*, vol. 74, no. 5, p. 054112, 2006.

[70] K. M. Indlekofer and H. Kohlstedt, "Simulation of quantum dead-layers in nanoscale ferroelectric tunnel junctions," *Europhys. Lett.*, vol. 72, no. 2, p. 282, 2005.

[71] T. Schimizu and T. Kawakubo, "First-principles approach to the effect of c-axis elongation of BaTiO3 thin films," *Jpn. J. Appl. Phys.*, vol. 37, no. 2 SUPPL. B, p. L235, 1998.

[72] N. A. Pertsev, A. G. Zembilgotov, and A. K. Tagantsev, "Effect of Mechanical Boundary Conditions on Phase Diagrams of Epitaxial Ferroelectric Thin Films," *Physical Review Letters*, vol. 80, no. 9, pp. 1988–1991, 1998.

[73] F. Xue, Y. Li, Y. Gu, J. Zhang, and L. Q. Chen, "Strain phase separation: Formation of ferroelastic domain structures," *Phys. Rev. B*, vol. 94, no. 22, p. 220101, 2016.

[74] R. Cohen and H. Krakauer, "Electronic structure studies of the differences in ferroelectric behavior of BaTiO3 and PbTiO3," *Ferroelectrics*, vol. 136, no. January 2013, pp. 65–83, 1992.

[75] N. A. Spaldin, "Analogies and Differences between Ferroelectrics and Ferromagnets," *Physics of Ferroelectrics*, vol. 218, no. 2007, pp. 175–217, 2007.

[76] W. Zhong, D. Vanderbilt, R. D. King-Smith, and K. Rabe, "Coulomb interaction and ferroelectric phase transitions in perovskite compounds," *Ferroelectrics*, vol. 164, no. April, pp. 291–301, 1995.

[77] T. Angsten, L. Martin, and M. Asta, "Orientation-dependent properties of epitaxially strained perovskite oxide thin films: Insights from first-principles calculations," *Phys. Rev. B*, vol. 95, no. 17, p. 174110, 2017.

[78] C. J. Eklund, C. J. Fennie, and K. M. Rabe, "Strain-induced ferroelectricity in orthorhombic CaTiO3 from first principles," *Phys. Rev. B*, vol. 79, no. 22, p. 220101, 2009.

[79] C.-H. Lin, C.-M. Huang, and G. Y. Guo, "Systematic ab initio study of the phase diagram of epitaxially strained SrTiO3," *J. Appl. Phys.*, vol. 100, no. 8, p. 084104, 2006.

[80] H. T. Stokes, E. H. Kisi, D. M. Hatch, and C. J. Howard, "research papers Octahedral tilting in cation-ordered perovskites a group-theoretical analysis research papers," *Acta Cryst.*, vol. B58, pp. 934–938, 2002.

[81] S. C. Miller and W. F. Love, *Tables of irreducible representations of space groups and co-representations of magnetic space groups*. Boulder: Pruett, 1967.

[82] N. A. Pertsev, A. K. Tagantsev, and N. Setter, "Phase transitions and strain-induced ferroelectricity in SrTiO 3 epitaxial thin films," vol. 61, pp. 825–829, 2000.

[83] M. Schindler, F. C. Hawthorne, and W. H. Baur, "Crystal Chemical Aspects of Vanadium : Polyhedral Geometries, Characteristic Bond Valences, and Polymerization of (VOn) Polyhedra," *Chem. Mater.*, vol. 12, pp. 1248–1259, 2000.

[84] D. J. Singh, "Electronic structure and bond competition in the polar magnet PbVO3," *Phys. Rev. B*, vol. 73, p. 094102, 2006.

[85] J. Selbin, "The Chemistry of Oxovanadium(IV)," *Chem. Rev.*, vol. 65, pp. 153–175, 1965.

[86] C. J. Ballhausen and H. B. Gray, "The Electronic Structure of the Vanadyl Ion," *Inorg. Chem.*, vol. 1, pp. 111–122, 1962.

[87] H. T. Evans Jr., "refinement and vanadium bonding in the metavanadates KV03, and KV03-H20 Crystal," *Z. Kristallogr.*, vol. 114, pp. 257–277, 1960.

[88] R. V. Shpanchenko, V. V. Chernaya, A. A. Tsirlin, and P. S. Chizhov, "Synthesis, Structure, and Properties of New Perovskite PbVO3," *Chem. Mater.*, vol. 16, pp. 3267–3273, 2004.

[89] Y. Uratani, T. Shishidou, F. Ishii, and T. Oguchi, "First-principles predictions of giant electric polarization," *Jpn. J. Appl. Phys.*, vol. 44, pp. 7130–7133, 2005.

[90] Y. Uratani, T. Shishidou, and T. Oguchi, "First-principles study on the magnetic anisotropy in multiferroic PbVO 3 and BiCoO 3," *J. Phys. Soc. Jpn.*, vol. 78, p. 084709, 2009.

[91] B. L. Chamberland and P. S. Danielson, "First-principles study on the magnetic anisotropy in multiferroic PbVO3 and BiCoO3," *J. Solid State Chem.*, vol. 3, p. 243, 1971.

[92] D. de Waal and A. M. Heyns, "Vibrational spectra of NaVO3, KVO3 and the solid solutions (Na0.88K0.12)VO3 and (Na0.5K0.5)VO3," *Mat. Res. Bull.*, vol. 27, pp. 129–136, 1992.

[93] S. Baroni, "Green's-Function Approach to Linear Response in Solids," *Phys. Rev. Lett.*, vol. 58, pp. 1861–1864, 1987.

[94] A. V. Krukau, O. A. Vydrov, A. F. Izmaylov, and G. E. Scuseria, "Influence of the exchange screening parameter on the performance of screened hybrid functionals," *J. Chem. Phys.*, vol. 125, p. 224106, 2006.

[95] A. J. Garza and G. E. Scuseria, "Predicting Band Gaps with Hybrid Density Functionals," *J. Phys. Chem. Lett.*, vol. 7, pp. 4165–4170, 2016.

[96] F. C. Hawthorne and C. Calvo, "The crystal chemistry of the pyroxines," *J. Solid State Chem.*, vol. 22, pp. 157–170, 1977.

[97] F. Marumo, M. Isobe, S. Iwai, and Y. Kondō, "α-Form of sodium metavanadate," *Acta Cryst.*, vol. 30, pp. 1628–1630, 1974.

[98] D. M. Adams, A. G. Christy, and J. Haines, "The phase stability of the alkali-metal vanadates at high pressures studied by synchrotron X-ray powder diffraction and infrared spectroscopy," *J. Phs. Condens. Matter*, vol. 3, pp. 6135–6144, 1991.

[99] T. Angsten and M. Asta, "Epitaxial phase diagrams of SrTiO3, CaTiO3, and SrHfO3: Computational investigation including the role of antiferrodistortive and A-site displacement modes," *Phys. Rev. B*, vol. 97, p. 134103, 2018.

[100] S. Liu, I. Grinberg, and A. M. Rappe, "Intrinsic ferroelectric switching from first principles," *Nature*, vol. 534, no. 7607, pp. 360–363, 2016.

[101] Q. Peng and R. E. Cohen, "Origin of pyroelectricity in LiNbO3," *Physical Review B*, vol. 83, no. 22, p. 220103, 2011.

APPENDIX A

Additional Calculation Details and Supporting Figures

A.1 Additional Calculation Procedure Details

A.1.1 Accuracy of Phase Transitions

For each of the 42 thin-film systems modeled in this work, the energy and polarization are calculated at each point in a grid of 47 misfit strains spanning -4% to 4%. These misfit strains are spaced by increments of 0.1% between -1% and 1% strain; increments of 0.2% between -2% and -1% and 1% and 2% strain; and increments of 0.25% for all other misfit strain regions. Space group symmetries of calculated phases are determined using the Spglib software package.[1] The symmetry precision tolerance value used to assign space group symmetries (and consequently determine points of phase transition) is 0.01Å. As a result of the use of a discrete grid and limited precision in symmetry determination, there is a small error in the phase transition misfit strains reported in this work that is on the order of $\pm 0.1\%$ misfit strain.

A.1.2 Justification for Random Search Method

In finding the minimum energy phases at each misfit strain, a random structure search is performed in order to find the minimum energy epitaxial structure. With this approach, there is no guarantee that the global minimum in energy will be located. However, the systems treated in this work have a very small number of degrees of freedom over which to search (12 displacement and 3 strain). This allows for a high degree of certainty in locating the true energetic minimum given enough random trials. The number of trials used in this work is at least three, with additional trials used as necessary to form smooth polarization and energy curves where first-order transitions do not apply (see Section A.1.3 for details). An alternative approach to random structure searching is to use as initial structures the known phases for each growth orientation. However, a random structure search is preferable to this

[1] atztogo.github.io/spglib/

approach for multiple reasons. In the first place, the set of possible phases is only tabulated in the literature for the (100) and (111) growth orientations.[2,3] Second, for certain phases, there can be two or more energy minima with the same space group symmetries. Thus, to be sure that all possible minima are accessed, a random seeding and multiple simulation cells are still required even if the set of all possible space group symmetries of phases are known. Given these concerns and the relatively inexpensive nature of the random structure search, it was decided that a random approach with many trials was both more general and more ammenable to automation.

A.1.3 Post-Processing of Polarization Curves

In many cases, after the initial pass of random structure searches at each misfit strain, the resulting energy and polarization curves show discontinuities. These could correspond either to sharp first-order phase transitions or the failure of a random structure search with three trials to find the true energy minimum. To ensure the latter cases are eliminated, an automated post-processing framework is applied. This framework locates all points showing sudden changes in polarization components above a 0.05 C/m^2 threshold and re-runs them using the neighboring relaxed structures as the initial structures (with misfit strain properly altered). This approach ensures that relaxed structures at neighboring misfit strains are shared, thereby minimizing the chance of missing true ground-state structures at a given misifit strain. To ensure sections of the phase diagram are not stuck in shared metastable states, this approach is iteratively applied until the only points on the polarization curve having discontinuous jumps above the 0.05 C/m^2 threshold correspond to predicted first-order phase transitions.

[2]Oja, R., Johnston, K., Frantti, J. and Nieminen, R. M. Phys. Rev. B 78, 16 (2008)

[3]N. A. Pertsev, A. G. Zembilgotov, and A. K. Tagantsev, Phys. Rev. Lett. 80, 1988 (1998)

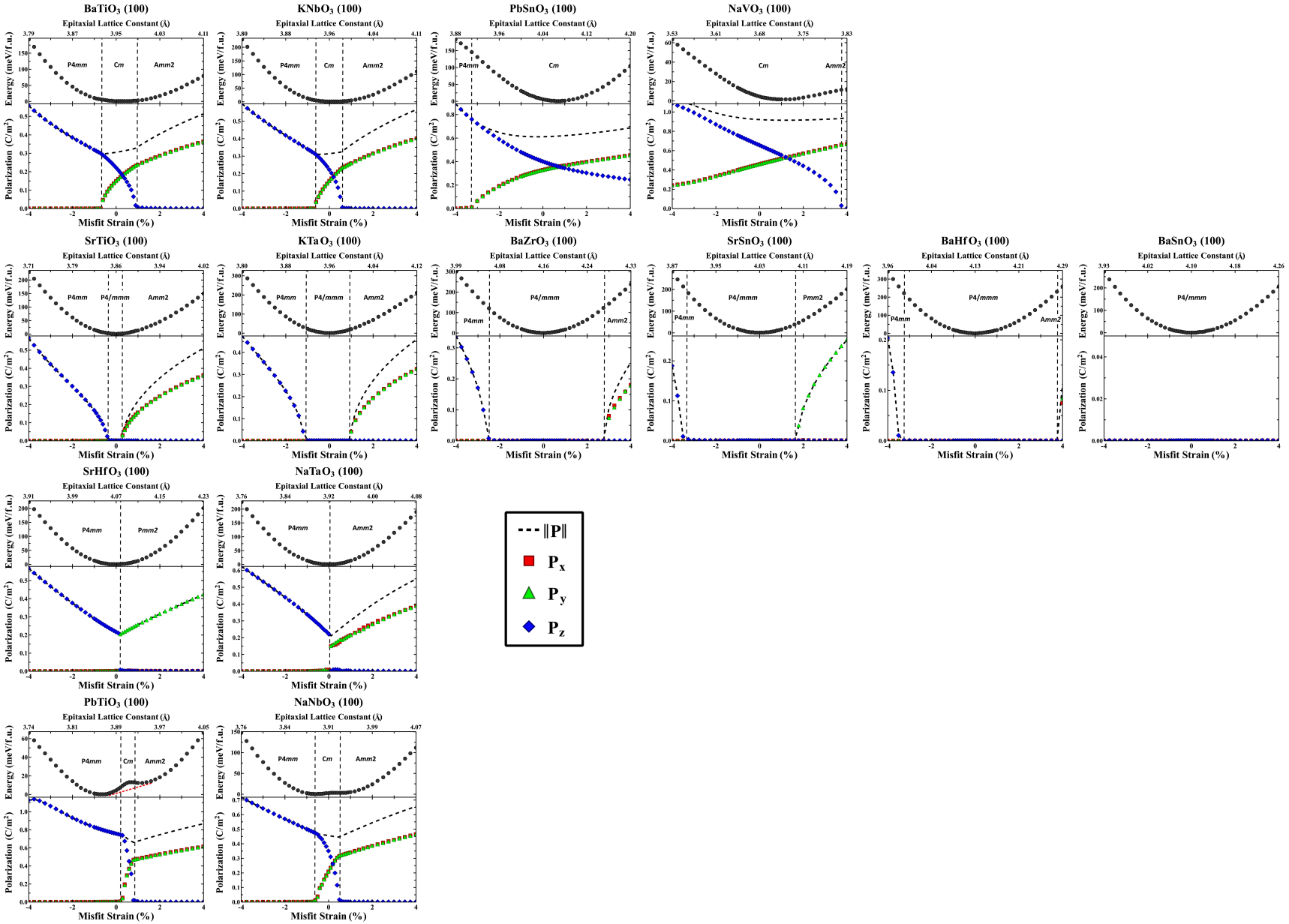
BaTiO3 (100)
KNbO3 (100)
PbSnO3 (100)
NaVO3 (100)
SrTiO3 (100)
KTaO3 (100)
BaZrO3 (100)
SrSnO3 (100)
BaHfO3 (100)
BaSnO3 (100)
SrHfO3 (100)
NaTaO3 (100)
PbTiO3 (100)
NaNbO3 (100)
Epitaxial Lattice Constant (Å)
Energy (meV/f.u.)
Polarization (C/m²)
Misfit Strain (%)
P4mm
Cm
Amm2
P4/mmm
Pmm2
‖P‖
Px
Py
Pz

Figure A.1

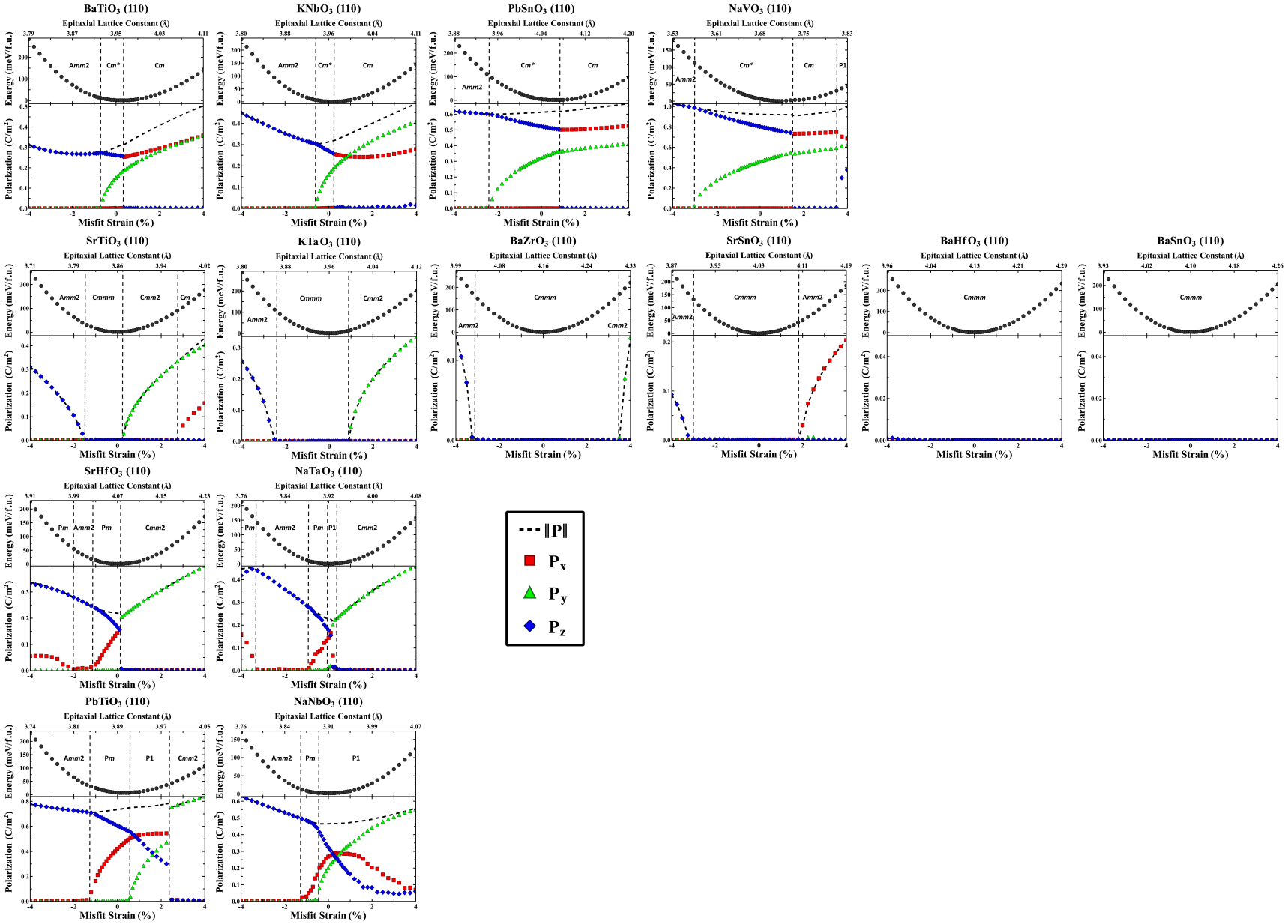
BaTiO3 (110)
KNbO3 (110)
PbSnO3 (110)
NaVO3 (110)
SrTiO3 (110)
KTaO3 (110)
BaZrO3 (110)
SrSnO3 (110)
BaHfO3 (110)
BaSnO3 (110)
SrHfO3 (110)
NaTaO3 (110)
PbTiO3 (110)
NaNbO3 (110)
Epitaxial Lattice Constant (Å)
Energy (meV/f.u.)
Polarization (C/m2)
Misfit Strain (%)
Amm2
Cm*
Cm
Cmmm
Cmm2
Pm
P1
‖P‖
Px
Py
Pz

Figure A.2

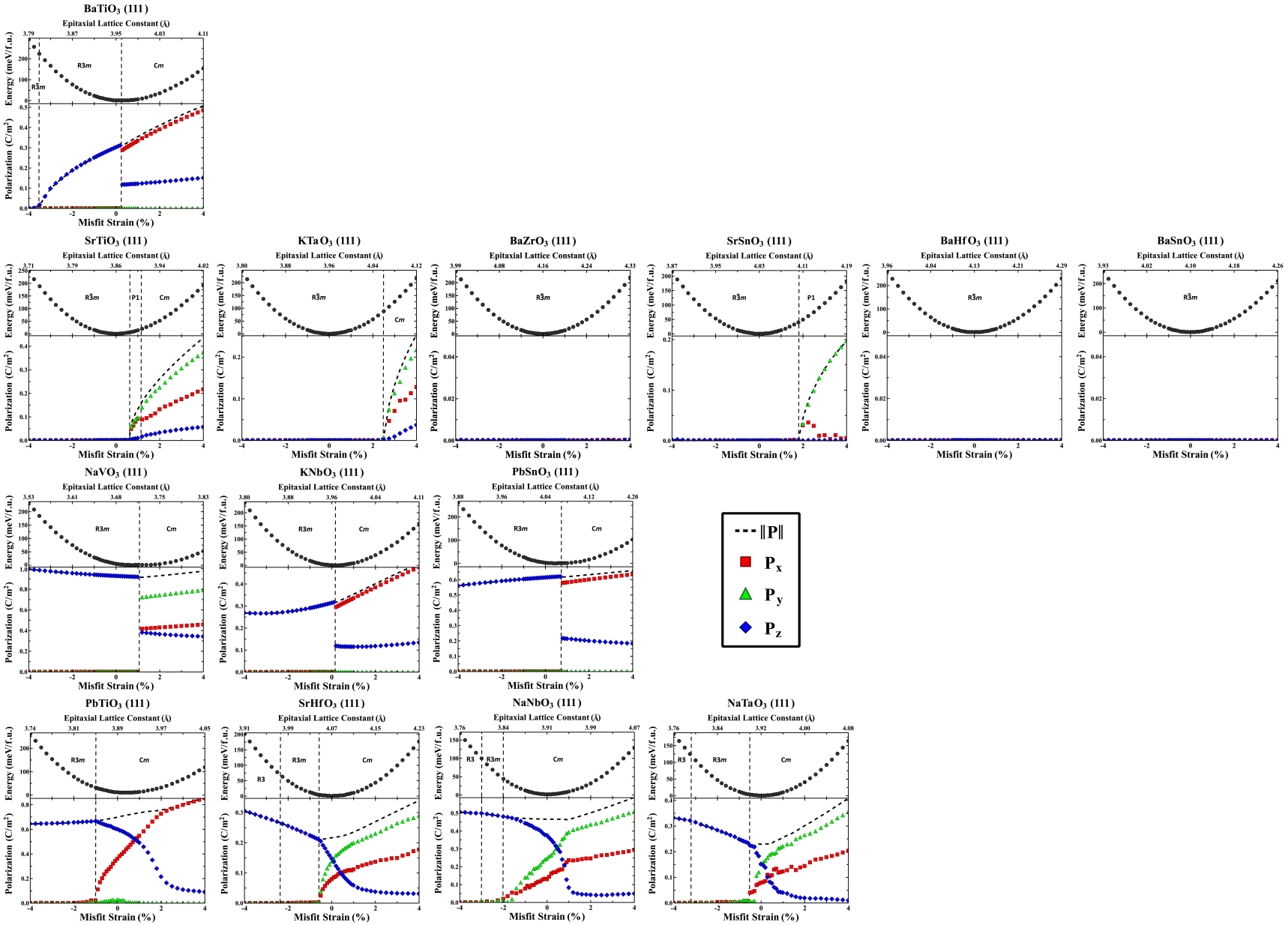
BaTiO3 (111)
SrTiO3 (111)
KTaO3 (111)
BaZrO3 (111)
SrSnO3 (111)
BaHfO3 (111)
BaSnO3 (111)
NaVO3 (111)
KNbO3 (111)
PbSnO3 (111)
PbTiO3 (111)
SrHfO3 (111)
NaNbO3 (111)
NaTaO3 (111)
Epitaxial Lattice Constant (Å)
Energy (meV/f.u.)
Polarization (C/m2)
Misfit Strain (%)
R3m
Cm
P1
R3
‖P‖
Px
Py
Pz

Figure A.3

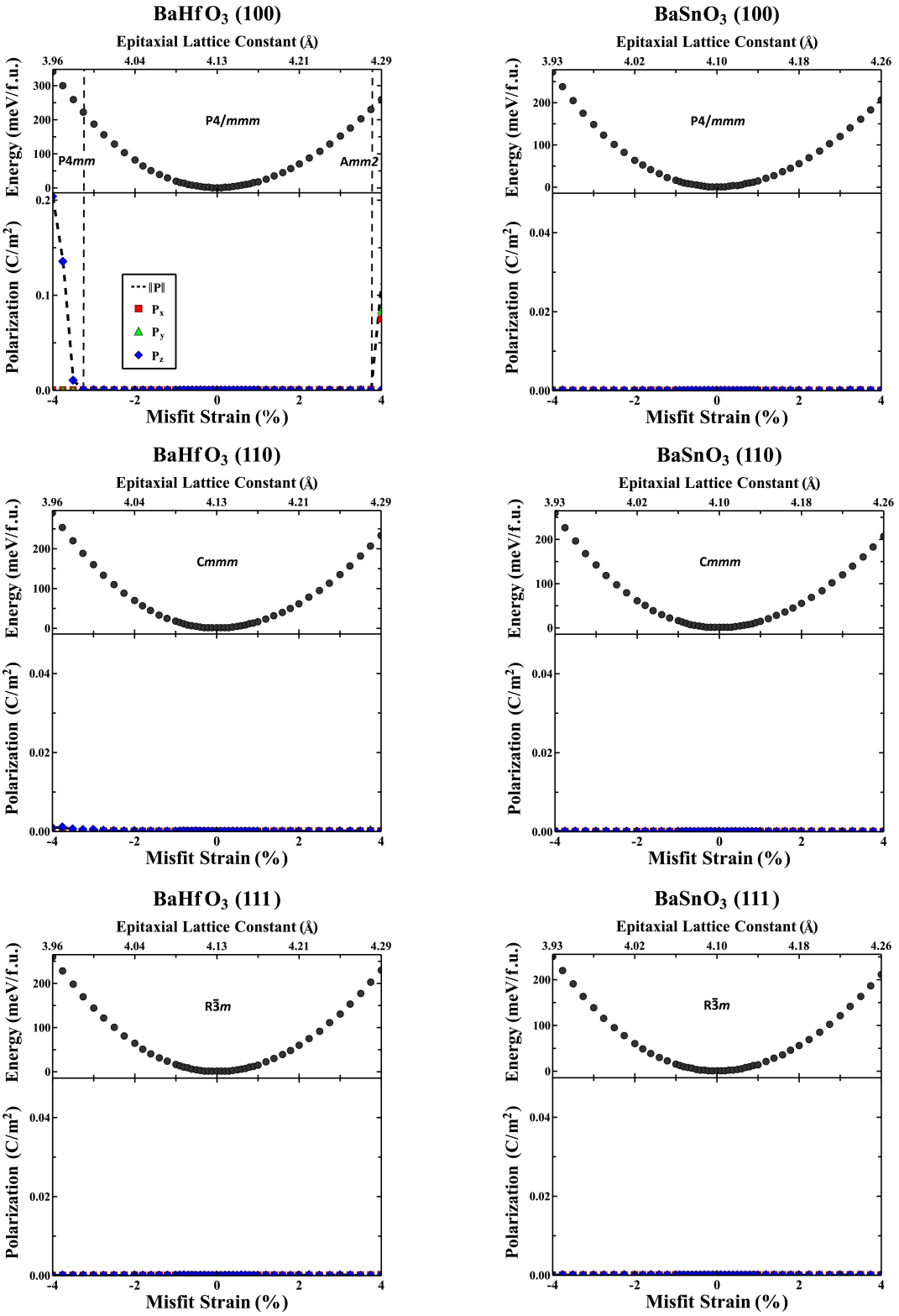
BaHfO3 (100)
Epitaxial Lattice Constant (Å)
3.96 4.04 4.13 4.21 4.29
Energy (meV/f.u.)
P4/mmm
P4mm
Amm2
Polarization (C/m2)
||P||
Px
Py
Pz
Misfit Strain (%)
BaSnO3 (100)
Epitaxial Lattice Constant (Å)
3.93 4.02 4.10 4.18 4.26
Energy (meV/f.u.)
P4/mmm
Polarization (C/m2)
Misfit Strain (%)
BaHfO3 (110)
Epitaxial Lattice Constant (Å)
3.96 4.04 4.13 4.21 4.29
Energy (meV/f.u.)
Cmmm
Polarization (C/m2)
Misfit Strain (%)
BaSnO3 (110)
Epitaxial Lattice Constant (Å)
3.93 4.02 4.10 4.18 4.26
Energy (meV/f.u.)
Cmmm
Polarization (C/m2)
Misfit Strain (%)
BaHfO3 (111)
Epitaxial Lattice Constant (Å)
3.96 4.04 4.13 4.21 4.29
Energy (meV/f.u.)
R3̄m
Polarization (C/m2)
Misfit Strain (%)
BaSnO3 (111)
Epitaxial Lattice Constant (Å)
3.93 4.02 4.10 4.18 4.26
Energy (meV/f.u.)
R3̄m
Polarization (C/m2)
Misfit Strain (%)

Figure A.4

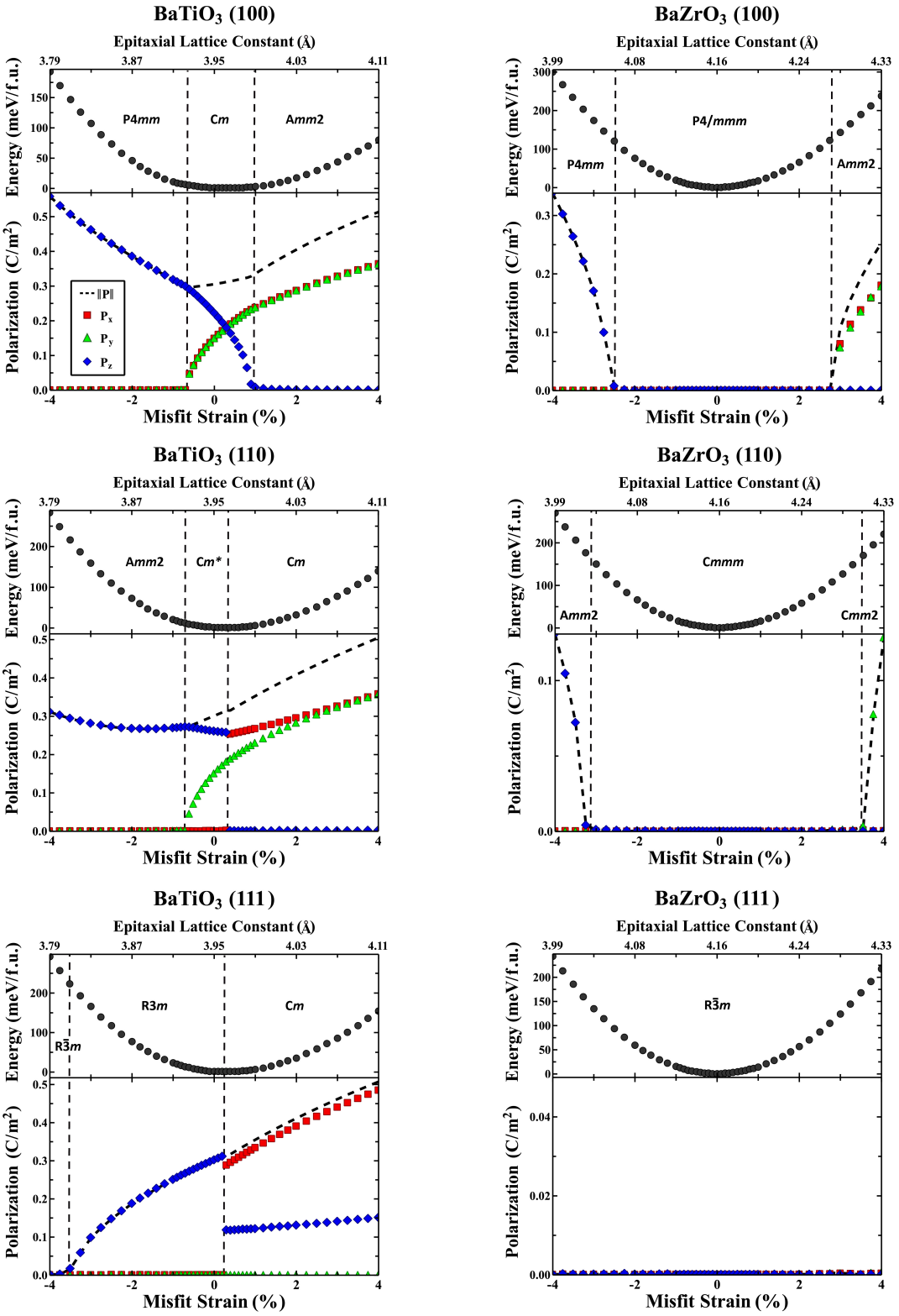
BaTiO3 (100)
Epitaxial Lattice Constant (Å)
3.79 3.87 3.95 4.03 4.11
Energy (meV/f.u.)
P4mm
Cm
Amm2
Polarization (C/m2)
||P||
Px
Py
Pz
Misfit Strain (%)
BaZrO3 (100)
Epitaxial Lattice Constant (Å)
3.99 4.08 4.16 4.24 4.33
Energy (meV/f.u.)
P4/mmm
P4mm
Amm2
Polarization (C/m2)
Misfit Strain (%)
BaTiO3 (110)
Epitaxial Lattice Constant (Å)
3.79 3.87 3.95 4.03 4.11
Energy (meV/f.u.)
Amm2
Cm*
Cm
Polarization (C/m2)
Misfit Strain (%)
BaZrO3 (110)
Epitaxial Lattice Constant (Å)
3.99 4.08 4.16 4.24 4.33
Energy (meV/f.u.)
Cmmm
Amm2
Cmm2
Polarization (C/m2)
Misfit Strain (%)
BaTiO3 (111)
Epitaxial Lattice Constant (Å)
3.79 3.87 3.95 4.03 4.11
Energy (meV/f.u.)
R3m
Cm
R3̄m
Polarization (C/m2)
Misfit Strain (%)
BaZrO3 (111)
Epitaxial Lattice Constant (Å)
3.99 4.08 4.16 4.24 4.33
Energy (meV/f.u.)
R3̄m
Polarization (C/m2)
Misfit Strain (%)

Figure A.5

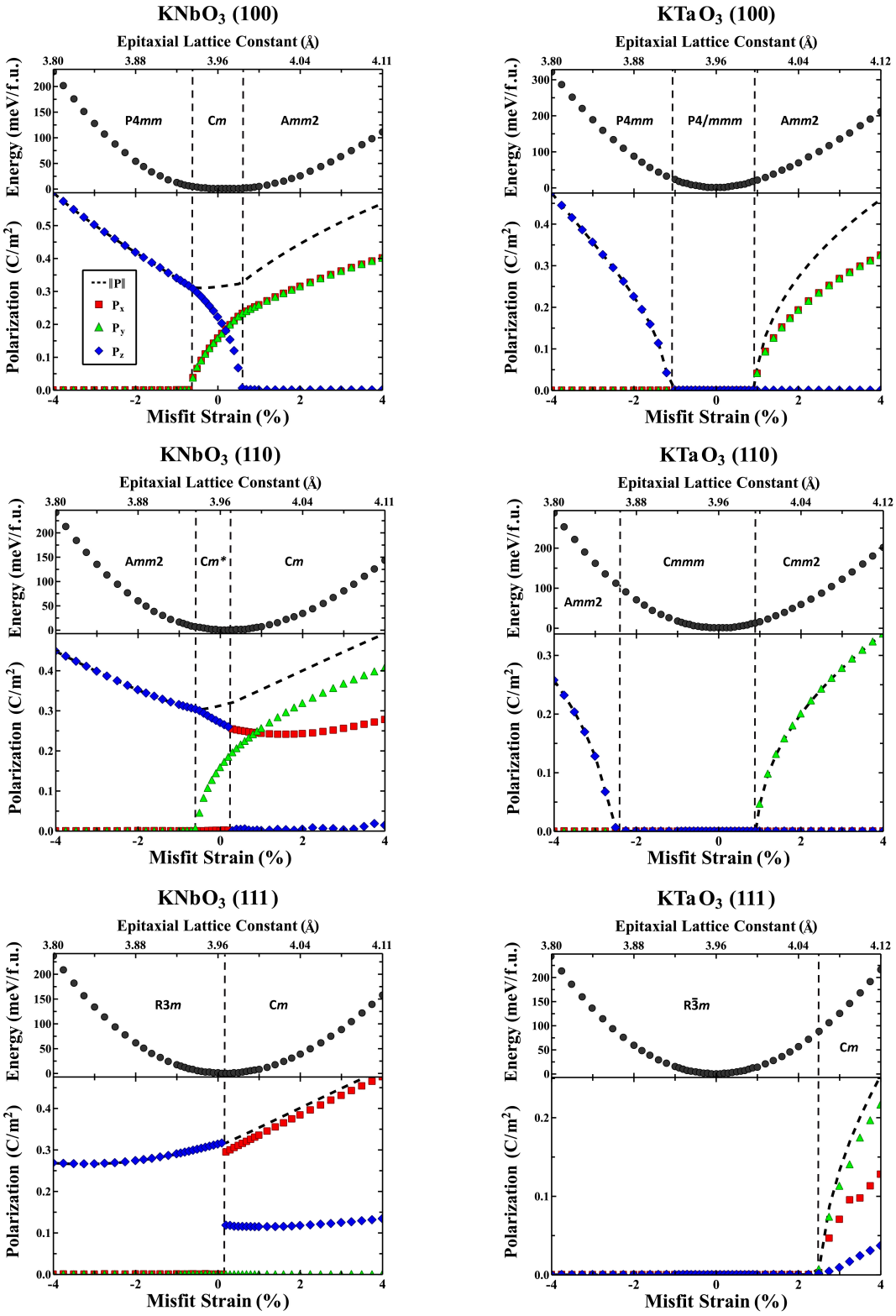
KNbO3 (100)
KTaO3 (100)
KNbO3 (110)
KTaO3 (110)
KNbO3 (111)
KTaO3 (111)
Epitaxial Lattice Constant (Å)
Energy (meV/f.u.)
Polarization (C/m2)
Misfit Strain (%)
P4mm
Cm
Amm2
P4/mmm
Cm*
Cmmm
Cmm2
R3m
R3̄m
||P||
Px
Py
Pz

Figure A.6

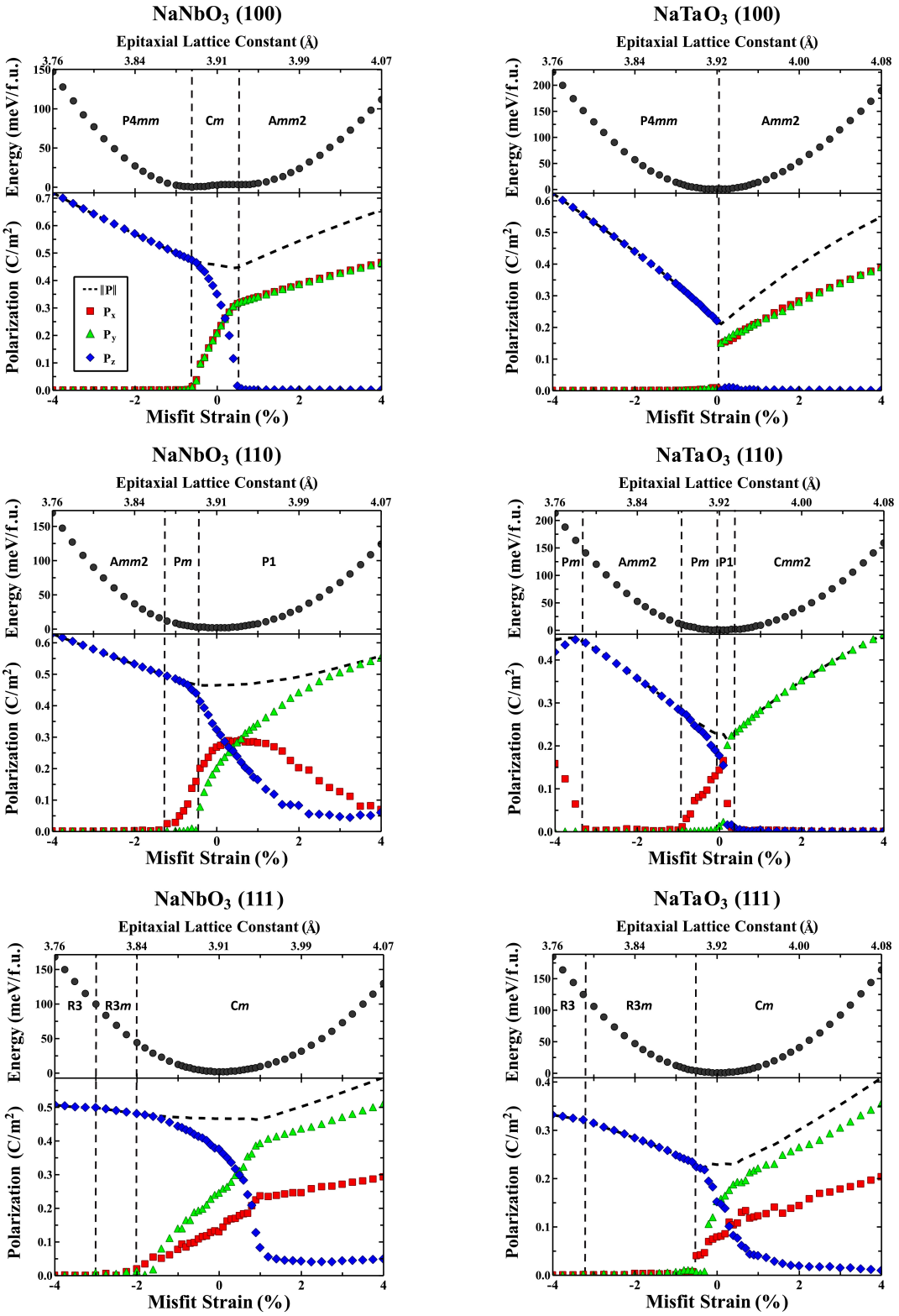
NaNbO3 (100)
Epitaxial Lattice Constant (Å)
3.76 3.84 3.91 3.99 4.07
Energy (meV/f.u.)
P4mm
Cm
Amm2
Polarization (C/m2)
||P||
Px
Py
Pz
Misfit Strain (%)
NaTaO3 (100)
Epitaxial Lattice Constant (Å)
3.76 3.84 3.92 4.00 4.08
Energy (meV/f.u.)
P4mm
Amm2
Polarization (C/m2)
Misfit Strain (%)
NaNbO3 (110)
Epitaxial Lattice Constant (Å)
3.76 3.84 3.91 3.99 4.07
Energy (meV/f.u.)
Amm2
Pm
P1
Polarization (C/m2)
Misfit Strain (%)
NaTaO3 (110)
Epitaxial Lattice Constant (Å)
3.76 3.84 3.92 4.00 4.08
Energy (meV/f.u.)
Pm
Amm2
Pm
P1
Cmm2
Polarization (C/m2)
Misfit Strain (%)
NaNbO3 (111)
Epitaxial Lattice Constant (Å)
3.76 3.84 3.91 3.99 4.07
Energy (meV/f.u.)
R3
R3m
Cm
Polarization (C/m2)
Misfit Strain (%)
NaTaO3 (111)
Epitaxial Lattice Constant (Å)
3.76 3.84 3.92 4.00 4.08
Energy (meV/f.u.)
R3
R3m
Cm
Polarization (C/m2)
Misfit Strain (%)

Figure A.7

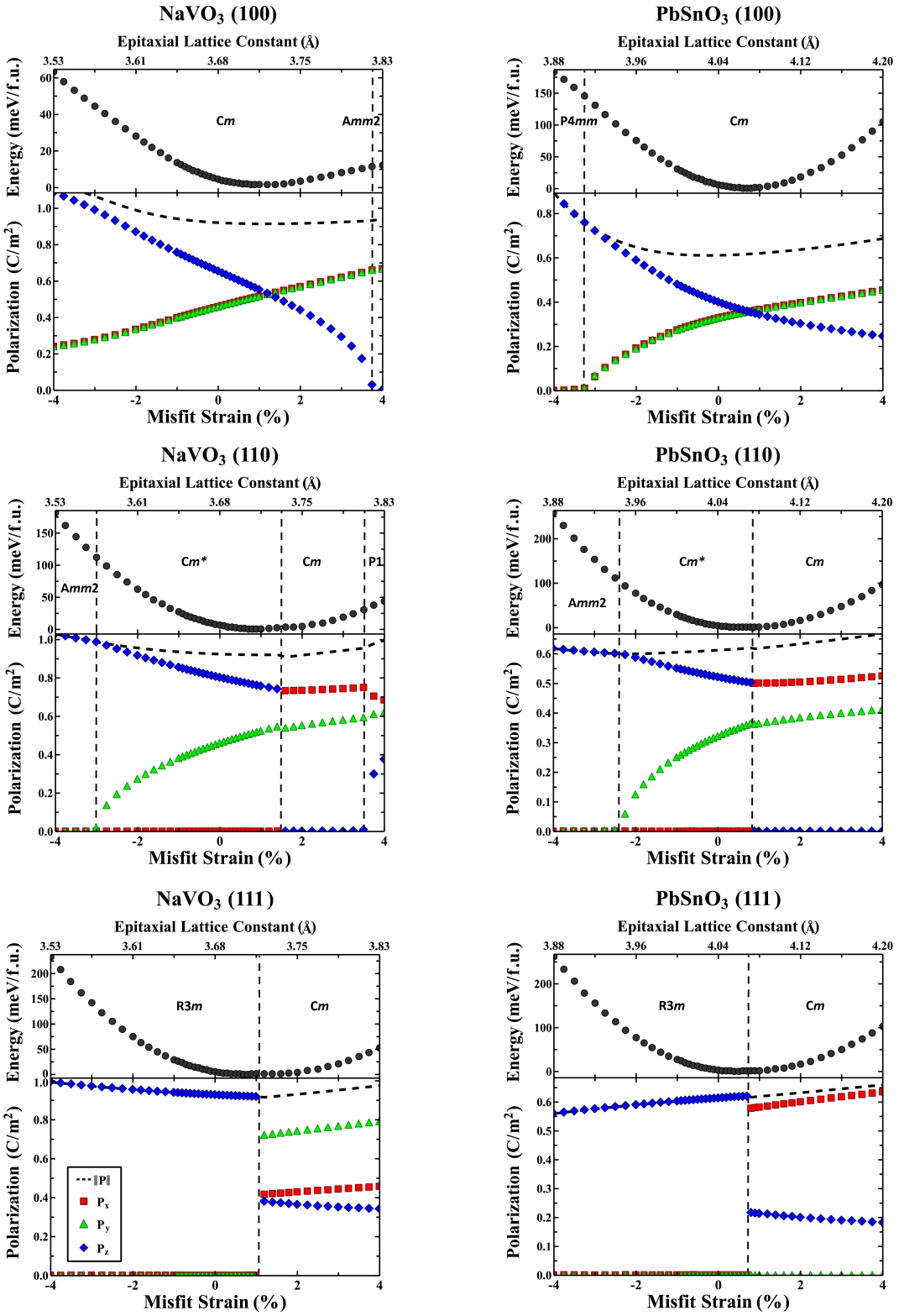
NaVO3 (100)
PbSnO3 (100)
NaVO3 (110)
PbSnO3 (110)
NaVO3 (111)
PbSnO3 (111)
Epitaxial Lattice Constant (Å)
Energy (meV/f.u.)
Polarization (C/m2)
Misfit Strain (%)
Cm
Amm2
P4mm
Cm*
P1
R3m
||P||
Px
Py
Pz

Figure A.8

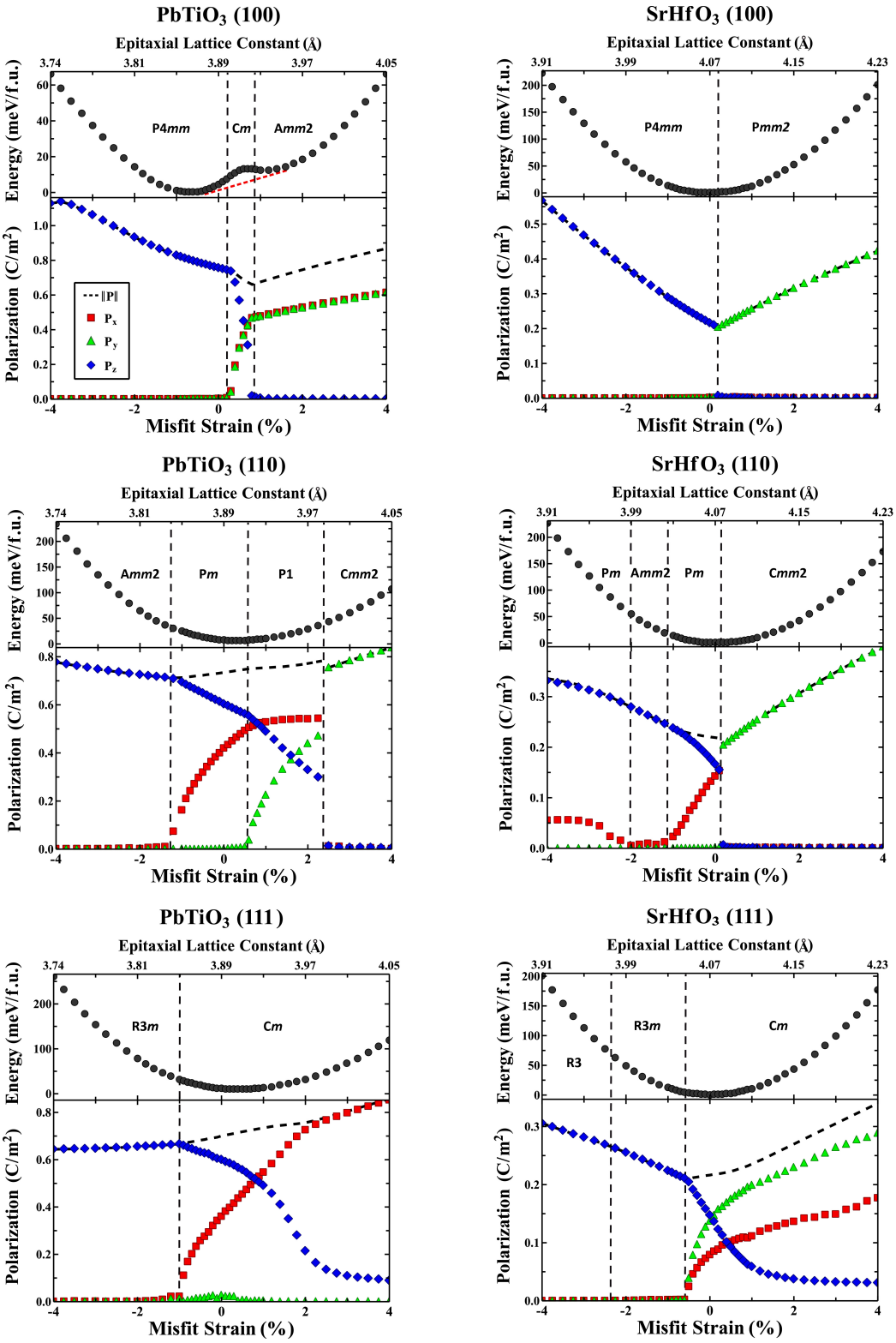
PbTiO3 (100)
SrHfO3 (100)
PbTiO3 (110)
SrHfO3 (110)
PbTiO3 (111)
SrHfO3 (111)
Epitaxial Lattice Constant (Å)
Energy (meV/f.u.)
Polarization (C/m2)
Misfit Strain (%)
P4mm
Cm
Amm2
Pmm2
Pm
P1
Cmm2
R3m
R3
||P||
Px
Py
Pz

Figure A.9

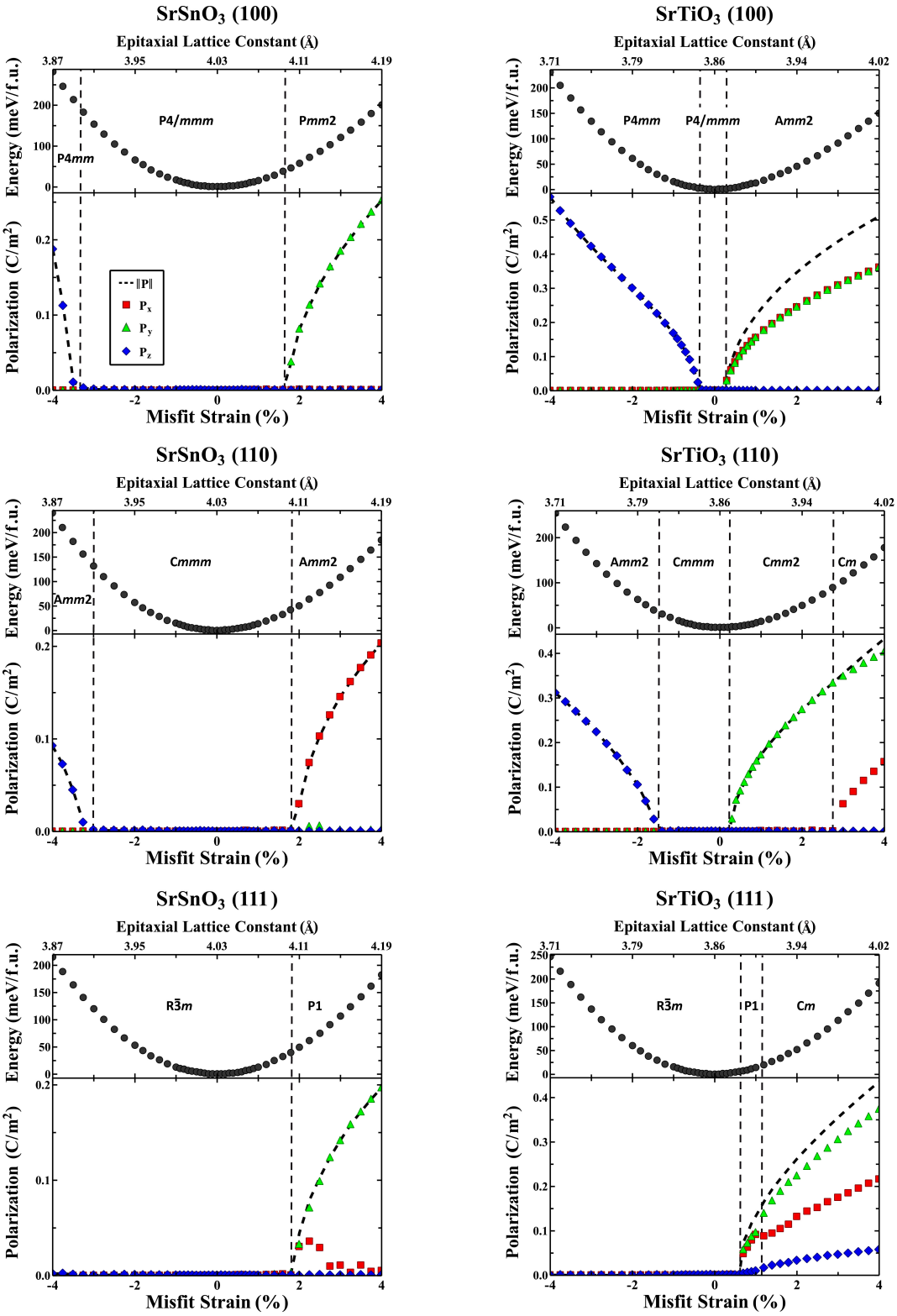
SrSnO3 (100)
SrTiO3 (100)
SrSnO3 (110)
SrTiO3 (110)
SrSnO3 (111)
SrTiO3 (111)
Epitaxial Lattice Constant (Å)
Energy (meV/f.u.)
Polarization (C/m2)
Misfit Strain (%)
P4/mmm
Pmm2
P4mm
Amm2
Cmmm
Cmm2
Cm
R3̄m
P1
||P||
Px
Py
Pz

Figure A.10

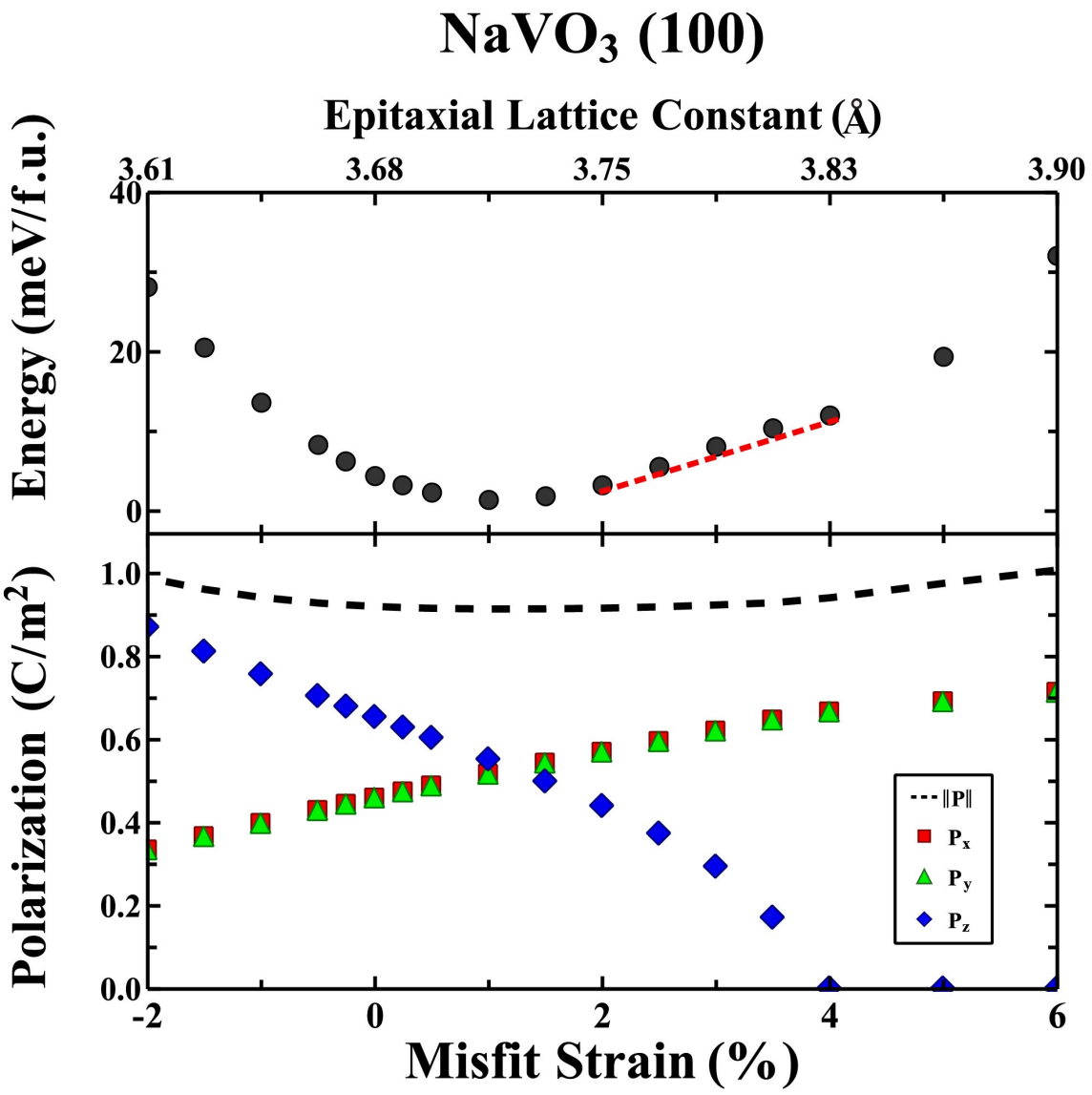

Figure A.11: Energy and polarization as a function of misfit strain for $NaVO_3$. Shown here is data for an expanded set of tensile misfit strains in order to demonstrate the slight tendency for this system to phase separate. The red dashed line indicates the common tangent construction. This construction predicts a slight lowering of energy by forming a phase mixture in the 2-4% misfit strain regime.

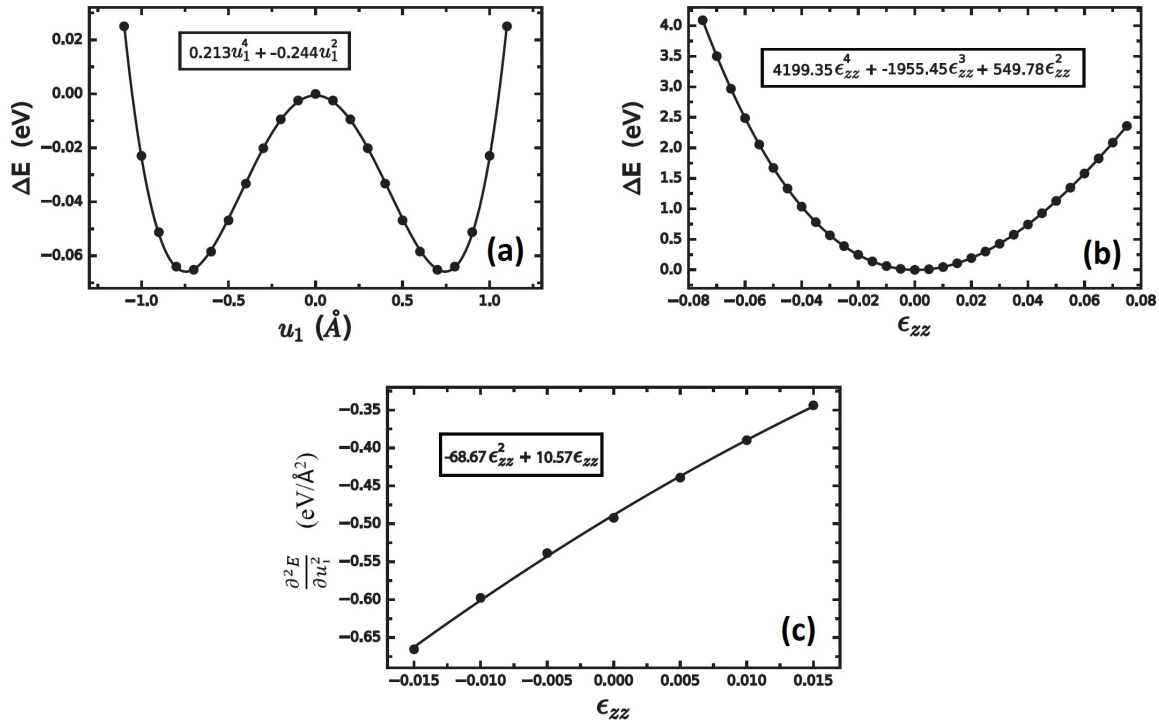

Figure A.12: Example fitted curves used to find expansion coefficients for $SrTiO_3$ at $\bar{\eta} = 0.0$. a) A polynomial fit of energy versus u_1, the softest eigenmode coordinate, gives the second and fourth order displacement term coefficients in Eq. 4.8 of the main text, b) a fit of energy versus ϵ_{zz} gives the second-, third-, and fourth-order tensile strain coefficients in Eq. 4.7, and c) a fit of the second derivative of energy with respect to u_1 versus ϵ_{zz} determines the strain-displacement coupling term in Eq. 4.9. Similar fitted curves are generated for the other eight softest displacement eigenmodes.

A.2 Example Calculation of Expansion Coefficients

Total energy calculations and curve fitting allow for the determination of all expansion coefficients defined in Eqs. 4.7-4.9 of the main text. Figure A.12 depicts an example for the case of $SrTiO_3$ with $\bar{\eta} = 0.0$. Figure A.12a shows the total energy versus the amplitude of the first eigenmode, from which the second- and fourth-order coefficients of the fitted polynomial give $\frac{1}{2}\lambda_1$ and C_1 in Eq. 4.8 of the main text, respectively. Figure A.12b gives the total energy versus out-of-plane tensile strain, from which the second-, third-, and fourth-order coefficients of the fitted polynomial give B_2, B_3, and B_4 in Eq. 4.7, respectively. Fig. A.12c shows the second derivative of the total energy with respect to the first eigenmode coordinate versus the out-of-plane strain, ϵ_{zz}. The first derivative of this fitted polynomial evaluated at $\epsilon_{zz} = 0$, and thus the first-order coefficient, gives $2A_1$ in Eq. 4.9. Each data point in Fig. A.12c is computed using a finite-difference expression for determining the second derivative of the energy, and thus is derived from multiple total-energy calculations.

A.3 Effect of the Exchange Correlation Functional

Use of the LDA in the present work leads to well-known systematic errors resulting in overbinding of the system, which are often reduced by the generalized-gradient approximation (GGA). In ferroelectric perovskite oxides, however, GGA-based functionals, including the HSE hybrid functional, can perform much worse than LDA.[4] Recent work[5] has demonstrated that use of the strongly constrained and appropriately normed (SCAN) meta-GGA functional can significantly improve accuracy over the LDA and GGA functionals when computing the structural, electronic, and energetic properties of ferroelectrics.

To assess the effect of using SCAN in the present work, the phase diagram for $CaTiO_3$ has been calculated using this meta-GGA functional. Figure A.13 shows the recalculated phase diagram for $CaTiO_3$ using SCAN. Due to the higher computational cost, only a portion of the formalism outlined in the main text was followed to generate this diagram. The five lowest-energy structures found using the full formalism of the main text under the LDA were used as initial structures when constructing Fig. A.13, with a random structure search being performed around each of these five structures. Within each search, relaxations at fixed in-plane biaxial strains were carried out using the same DFT parameters as in the main text, but with the SCAN functional applied instead of the LDA. It is possible that following the full formalism with the SCAN functional could result in other phases not reported in Fig. A.13, but the results indicate how different the descriptions are of the local energy landscapes between LDA and SCAN.

A comparison of Fig. A.13 with Fig. 4.1b indicates that the primary difference of the SCAN versus LDA results is that the former give phase boundaries shifted to epitaxial lattice constants that are approximately 1% larger in magnitude. This is consistent with the overbinding in LDA that produces energy equilibrium lattice constants that are underestimated by a comparable amount. The same phases and phase orderings appear in Fig. A.13 as in Fig. 4.1b, and the eigenmode amplitudes and their dependencies on misfit strain are also very similar. This demonstrates that the LDA functional describes the local energy landscape about the three phases in a manner consistent with the SCAN functional, once the systematic shift in lattice parameter has been applied.

[4] D. I. Bilc et al., Phys. Rev. B 77, 165107 (2008)
[5] Y. Zhang et al., Phys. Rev. B 96, 035143 (2017)

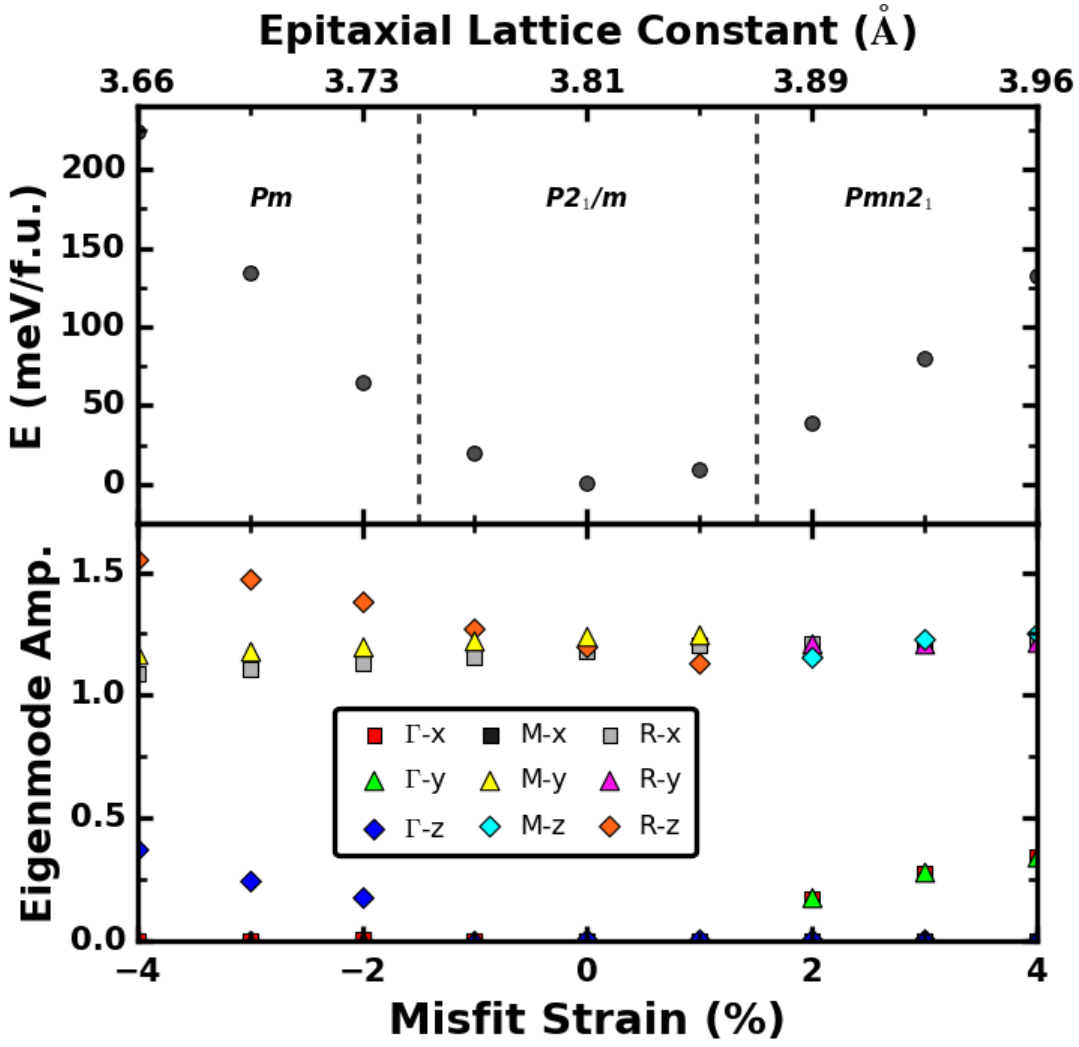

Figure A.13: Recalculated phase diagram for $CaTiO_3$ using the SCAN functional. Energies and eigenmode amplitudes of the lowest-energy epitaixal structures are given. Note that the same reference lattice constant used in Fig. 4.1b has been used here for reporting the misfit strain.

Table A.1: Computed coefficients of the higher-order energy expansion terms at each misfit strain for $SrTiO_3$, $CaTiO_3$, and $SrHfO_3$. Each entry gives the coefficient that appears before the term denoted in the top row, and these values correspond to B_2, B_3, and B_4 in Eq. 4.7, all C_j in Eq. 4.8, and all A_j in Eq. 4.9 of the main text respectively. u_i is the amplitude of displacement eigenmode i. More significant figures than shown below are used in the actual expansions. A '*' indicates a mode is stable and therefore not considered a degree of freedom in the energy expansion. Second order displacement eigenmode coefficients can be obtained by taking one-half of the eigenvalues listed in Table 4.2 of the main text. All coefficient units are eV per 40-atom cell.

$SrTiO_3$																				
Misfit Strain	ϵ_{zz}^2	ϵ_{zz}^3	ϵ_{zz}^4	u_1^4	u_2^4	u_3^4	u_4^4	u_5^4	u_6^4	u_7^4	u_8^4	u_9^4	$\epsilon_{zz}u_1^2$	$\epsilon_{zz}u_2^2$	$\epsilon_{zz}u_3^2$	$\epsilon_{zz}u_4^2$	$\epsilon_{zz}u_5^2$	$\epsilon_{zz}u_6^2$	$\epsilon_{zz}u_7^2$	$\epsilon_{zz}u_8^2$	$\epsilon_{zz}u_9^2$
-2%	516.24	-1837.43	3956.76	8.26	0.26	0.23	0.25	0.25	*	*	*	*	-70.26	-3.51	-5.33	3.89	3.89	*	*	*	*
-1%	532.76	-1897.28	4096.02	7.71	0.24	0.24	0.24	0.22	0.56	0.56	*	*	-67.46	-3.42	4.68	4.68	-5.23	4.79	4.79	*	*
0%	549.78	-1955.45	4199.35	0.21	0.21	0.23	0.21	0.21	0.21	*	*	*	5.29	5.29	-3.39	5.10	5.10	-5.16	*	*	*
1%	567.32	-2017.70	4280.11	7.77	7.77	0.22	0.22	0.21	0.20	0.20	*	*	8.82	8.82	5.74	5.74	-3.34	5.37	5.37	*	*
2%	584.78	-2075.36	4396.85	9.43	9.43	9.88	9.88	0.21	0.21	0.20	0.20	0.20	11.16	11.16	18.78	18.78	6.14	6.14	5.62	5.62	-3.27
$CaTiO_3$	ϵ_{zz}^2	ϵ_{zz}^3	ϵ_{zz}^4	u_1^4	u_2^4	u_3^4	u_4^4	u_5^4	u_6^4	u_7^4	u_8^4	u_9^4	$\epsilon_{zz}u_1^2$	$\epsilon_{zz}u_2^2$	$\epsilon_{zz}u_3^2$	$\epsilon_{zz}u_4^2$	$\epsilon_{zz}u_5^2$	$\epsilon_{zz}u_6^2$	$\epsilon_{zz}u_7^2$	$\epsilon_{zz}u_8^2$	$\epsilon_{zz}u_9^2$
-2%	522.02	-1879.32	4106.94	0.32	2.88	0.30	0.30	0.30	0.26	0.26	1.16	1.16	1.54	-38.16	0.35	7.21	7.21	7.32	7.32	-0.67	-0.67
-1%	539.40	-1945.12	4246.54	0.31	0.29	0.29	0.28	0.25	0.25	1.86	1.12	1.12	1.58	7.16	7.16	0.46	7.18	7.18	-32.4	1.94	1.94
0%	557.37	-2009.83	4353.20	0.28	0.28	0.28	0.25	0.25	0.26	1.29	1.29	1.17	7.57	7.57	1.39	7.45	7.45	0.15	5.77	5.77	-27.03
1%	575.45	-2075.97	4517.48	0.27	0.27	0.27	1.74	1.74	0.24	0.24	0.25	0.81	7.50	7.50	1.36	10.72	10.72	7.28	7.28	0.42	-22.95
2%	593.83	-2140.45	4648.33	2.63	2.63	0.26	0.26	0.21	0.21	0.24	0.22	0.57	15.75	15.75	7.64	7.64	7.28	7.28	1.51	0.48	-19.55
$SrHfO_3$	ϵ_{zz}^2	ϵ_{zz}^3	ϵ_{zz}^4	u_1^4	u_2^4	u_3^4	u_4^4	u_5^4	u_6^4	u_7^4	u_8^4	u_9^4	$\epsilon_{zz}u_1^2$	$\epsilon_{zz}u_2^2$	$\epsilon_{zz}u_3^2$	$\epsilon_{zz}u_4^2$	$\epsilon_{zz}u_5^2$	$\epsilon_{zz}u_6^2$	$\epsilon_{zz}u_7^2$	$\epsilon_{zz}u_8^2$	$\epsilon_{zz}u_9^2$
-2%	650.56	-2458.53	5626.13	0.23	0.22	0.22	0.22	0.19	0.19	0.74	0.45	0.65	0.39	-0.73	6.21	6.21	6.44	6.44	-22.21	-10.05	-12.04
-1%	668.82	-2519.17	5688.55	0.22	0.21	0.21	0.20	0.19	0.19	0.53	0.49	0.49	0.49	7.18	7.18	-0.63	7.20	7.20	-18.54	-1.06	-1.06
0%	686.96	-2579.53	5737.01	0.20	0.20	0.20	0.18	0.18	0.19	0.43	0.43	0.42	8.00	8.00	0.66	7.78	7.78	-0.45	3.26	3.26	-15.99
1%	704.54	-2639.53	5885.13	0.19	0.19	0.19	0.18	0.18	0.18	0.44	0.44	0.45	8.79	8.79	0.81	8.47	8.47	-0.39	7.75	7.75	10.27
2%	722.19	-2695.19	5968.25	0.18	0.18	0.17	0.17	0.17	0.15	0.47	0.47	0.44	9.40	9.40	8.93	8.93	0.88	-0.22	11.55	11.55	11.42